DISSERTATION

RAIN AND RELAMPAGO: ANALYSIS OF THE DEEP CONVECTIVE STORMS OF CENTRAL ARGENTINA

Submitted by

Nathan Robert Kelly

Department of Atmospheric Science

In partial fulfillment of the requirements

For the Degree of Doctor of Philosophy

Colorado State University

Fort Collins, Colorado

Spring 2023

Doctoral Committee:

Advisor: Russ Schumacher

Kristen Rasmussen
Michael Bell
Peter Nelson

Copyright by Nathan Robert Kelly 2023

All Rights Reserved

ABSTRACT

RAIN AND RELAMPAGO: ANALYSIS OF THE DEEP CONVECTIVE STORMS OF CENTRAL ARGENTINA

When, where and how much precipitation falls are fundamental questions to research interests spanning the weather to climate spectrum, yet are difficult to solve. The various methods used to answer "how much" each have sources of error, making it important to obtain knowledge about the characteristics of an individual dataset. This is especially true for rare events such as extreme precipitation. IMERG, TRMM 3B42, MERRA2 and ERA5 precipitation datasets were regridded to the same resolution and compared for 3-hourly heavy rainfall (99th and 99.9th percentile) in subtropical South America , which has some of the strongest convective storms on Earth. Seasonal and dirunal distribution are compared, with similar seasonal distributions between the datasets but at the diurnal scale MERRA2 and ERA5 show more afternoon events than TRMM and IMERG. Thermodynamic environments were compared with MERRA2 events tending to occur in more marginal environments than TRMM 3B42 and ERA5 environments over much of the analyzed region. Overall the satellite datasets showed the highest amounts. Brief case studies are included to illustrate these differences, which reinforce that choice of dataset can be an important factor in precipitation research.

How the precipitation falls is also addressed using a case study from the RELAMPAGO field program in Argentina. Many observations are available of this case, which occurred during the mobile operations period of the field program. Mobile surface stations, increased temporal resolution from fixed sounding sites, and six mobile sounding systems provide a high level of detail on the evolution of this storm system. Additionally, a trove of radar data and a GOES mesoscale sector are available. This case is demonstrative of a common occurrence in the region: a strong MCS (Mesoscale Convective System) over the Sierras de Córdoba mountain range. The extent

of the backbuilding observed with this MCS was not predicted by the operation convective allowing models used for field program forecasting. To study this event two simulations are presented: one in which backbuilding of the MCS occurs and one where such backbuilding does not occur. The difference between these simulations is the number of vertical levels used in the model which impacts moisture availability upstream of the system via the effect of mountain wave downslope winds.

ACKNOWLEDGEMENTS

Many thanks to all the patient people who have stuck with me throughout this process. Gratitude goes firstly to Aura Lee who took on so much extra work while I dedicated many hours to the completion of my PhD. You mean so much to me and I could not have done it without you. Thanks also to Russ for his patient input on the science and for never letting me freak out too much, while also landing me my dream job. I also want to thank my parents and grandparents, who have been a constant positive support these past seven years. I would be remiss if I did not mention all my friends for their invaluable help keeping me sane through social interaction, thanks to you all. I also want to acknowledge my coworkers and managers at DTN for being very flexible as the expected PhD completion date continued to march backwards. Thanks to the committee as well for being very flexible with me as I finish while working part time. It is truly incredible that I get to be at this point in my academic journey. This work was financially supported by National Science Foundation grant AGS-16661862, and use of the Cheyenne supercomputer was provided by the National Center for Atmospheric Research Computational and Information Systems Laboratory (doi:10.5065/D6RX99HX).

DEDICATION

Dedicated to the memory of my Grandma, Barbara Jean Thomas (November 27, 1936 - January 28, 2022), without whose constant prayers I would have never gotten to where I am today.

Requiem aeternam dona ei Domine, et lux perpetua luceat ei.

TABLE OF CONTENTS

LIST OF FIGURES

Chapter 1

Introduction

Rain is perhaps the most variable part of daily life in the modern world, particularly for regions whose economy centers on agriculture. Central Argentina is such a region. Soybeans growing in that region comprise 30.7% of the total exports of Argentina (Phélinas and Choumert, 2017). Most of this production is not irrigated and thus more vulnerable to variations in rainfall (Hernandez et al., 2015). Much of the rainfall during the growing season comes from Mesoscale Convective Systems (MCSs), multicell thunderstorm complexes that are fueled by the South American Low Level Jet (SALLJ) bringing warm moist air south from the Amazon (e.g. Durkee et al., 2009; Cavalcanti, 2012; Rasmussen et al., 2016). Due to their impact on the region, an accurate understanding of how these storms form and detailed analysis of how much rain they produce is very important. However, due to a relative lack of observations (both gauges and radars) for measuring precipitation in the region for measuring, reanalysis and satellite observations of precipitaiton are imperative to long term analysis of rainfall amounts especially at small spatial and temporal scales. The influence of the spatially small (100km x 300km) (SDC) mountain range on convection in the region at these smaller scales is particularly important. In-situ data collected in the region by the Remote Sensing of Electrification, Lightning, and Mesoscale/Microscale Processes with Adaptive Ground Observations (RELAMPAGO) field campaign centered in Córdoba Province, Argentina helped to fill gaps in the knowledge about storms in the region (Nesbitt et al., 2021). Detailed analysis of the events observed during the campaign can help inform interpretation of data gleaned from reanalysis and satellite datasets on the nature of the storms in the region and their rainfall characteristics. A particularly notable case was observed on 13-14 December 2018 and will be the focus of the RELAMPAGO analysis conducted for this dissertation.

The objective of this study is to add to knowledge of precipitation patterns and processes in Argentina incorporating both long term precipitation datasets and a case study from the RELAMPAGO campaign. Chapter 2 analyzes four preicpitation datasets to compare the characteristics

of 3-hour rainfall at the 99th percentile level. Two of these datasets (ERA5 and MERRA2) are reanalyses utilizing observations and data assimilation to make a precipitation estimate and two are satellite datasets calibrating both active and passive remote sensing to rainfall rates. 3-hour temporal resolution allows for the capture of intense rainfall resulting from the MCSs that make up the majority of warm season rainfall in the region. No direct comparison to observations in the study region is possible at the temporal and spatial scale that these datasets utilize, but comparing these datasets to each other allows for knowledge of the biases of each dataset relative to the others. These biases manifest themselves both in the total volume of precipitation each dataset depicts and in the meteorological environments that heavy rain events in each dataset occur in. Events in the different datasets often did not occur at the same time, which is a concern for researchers who wish to construct composite maps of the large scale weather conditions likely to lead to events. Large differences were observed in average convectively available potential energy (CAPE), convective inhibition (CIN) and precipitable water (PWAT) present during events in each dataset as well. Both satellite datasets recorded events in environments with higher CIN and lower CAPE than the reanalysis events. Since the satellite datasets rely on observing the cloud tops from space, this suggests that the reanalysis datasets do not produce events in more marginal thermodynamic environements, or that the algorithms used to produce the satellite datasets are not well calibrated to the types of storms that form in more marginal environments. With rain gauge observations unavailable in this region for these spatial and temporal scales it is difficult to know which datasets hold the "truth" in these situations. However, identifying these differences in environment between datasets contextualizes the results of any analysis of events above a certain percentile.

Chapter 3 analyzes an event observed during the RELAMPAGO campaign that produced a 99th percentile 3-hour rainfall event in Córdoba Province on 13-14 December 2018. Operation models used during the RELAMPAGO campaign to plan campaign operations did not depict backbuilding, a process by which new convective cells are generated on the west (upstream) side of the storm. This process can lead to torrential rains as storm cells repeatedly move over the same area. By utilizing a model run that did produce backbuilding using the same parameters as the real-time

run during the campaign but 30 more vertical levels the causes of these important differences in storm structure can be assessed, provides a window into the important processes that produce these events and addresses some of the challenges they present to forecasters. The results herein are useful to researchers using reanalysis datasets to analyze past precipitation events as well as for entities utilizing convective allowing models to forecast future events in real time in this region of Argentina.

Chapter 2

Extreme 3-Hourly Precipitation in Subtropical Argentina: Comparison of Four Datasets

2.1 Chapter 2 Introduction

Quantitative Precipitation Estimation (QPE) is an important aspect of both operational meteorology and climate analysis. Rain gauges, radar and satellite remote sensing methods, and reanalysis datasets all offer different methods of obtaining the answer: How much rain fell? Unfortunately, each of these methods, as well as datasets produced using techniques that combine aspects of each of these methods, are all subject to error and may arrive at different conclusions. Different datasets could have different sets of events that are considered extreme for a given definition, which may in turn influence the results of an ensuing analysis. Rain gauges observe only one discrete point, and a dense network is required for a good estimate. Xu et al. (2013), using daily precipitation data, found that the accuracy of a runoff model dropped significantly when the density of the assimilated rain gauge network dropped below 0.4 per 1000km^2. Reanalysis datasets are only as accurate as the data assimilation scheme, the data that is assimilated, and the accuracy of the model parameterizations (e.g. Bosilovich et al., 2015; Hersbach et al., 2020). Satellite based estimates rely on algorithms to convert indirect observations to rainfall rates. These methods often are in partial disagreement with each other and rain gauge measurements, and this is especially true in the case of extreme precipitation (e.g. Sun and Barros, 2010; Chen et al., 2013; Yucel and Onen, 2014; Sekaranom and Masunaga, 2017). These potential errors are exacerbated by the fact that many areas of the world do not have a dense enough rain gauge network or radar network to adequately assess the uncertainty in satellite and reanalysis datasets. One such area is subtropical South America, the subject of this study. Hurtado et al. (2021) reports a station density of 0.03 per 1000km^2 in subtropical Argentina. The province of Córdoba, within subtropical Argentina, con-

tains 7 gauge sites with enough data to span the period 1930-2006, for a density of approximately 0.04 per 1000km^2 (de la Casa and Nasello, 2010). Argentina also began installing a radar network relatively recently, in December 2014 (Vidal et al., 2017). These challenges leave reanalysis and satellite precipitation estimates as the only sources of long-term high temporal and spatial resolution precipitation data, in a region where such data is vitally important. Subtropical South America is a breadbasket region, and Argentina is among the world's top exporters of corn and soybeans (Merlos et al., 2015). Heavy short-term rainfall can damage this industry via the washing away of topsoil, though this is mitigated by the implementation of no-till agriculture (Hugo et al., 2006). The region is also prone to flash flooding, especially near the SDC mountain range which extends from north to south through the center of Córdoba Province. (Latrubesse and Brea, 2009; Le Coz et al., 2016). Extreme amounts of rainfall can therefore be particularly impactful to life and economic activity in this region, but research into such events must acknowledge potential differences between the precipitation datasets used. This study will focus on four datasets: the Modern Era Retrospective Analysis for Research and Applications (MERRA2; Bosilovich et al., 2015), European Center for Medium-Range Weather Forecasts Re-Analysis 5th Generation (ERA5; Hersbach et al., 2020), NASA global precipitation measurement (GPM) integrated multi-satellite retrievals for GPM (IMERG; Huffman et al., 2015) and Tropical Rainfall Measurement Mission multi-satelite precipitation analysis (TMPA) 3B42 v7, hereafter referred to as TRMM (Huffman et al., 2010).

Many recent studies have also addressed the issue of dataset validation and comparison. Tang et al. (2020) compared ten different datasets at daily and hourly scales over China, finding that gauge adjusted satellite products (including TRMM and IMERG) outperformed reanalysis datasets (including ERA5 and MERRA2) using Kling-Gupta efficiency, a metric that quantifies correlation, bias, and variability of the datasets compared to gridded gauge observations. At the hourly scale, this study found that the satellite based products captured diurnal variability better than the reanalysis products. IMERG was found to reasonably represent the diurnal cycle of precipitation in the maritime continent as well (Tan et al., 2019). Giles et al. (2021) found that TRMM had a

more pronounced diurnal cycle in northeastern Argentina than ERA5 and MERRA2. Beck et al. (2019) found that over the continental United States IMERG performed better than TRMM 3B42 compared to Stage-IV gauge-radar data, and in general the satellite based products did better in convective regions (such as the plains and the southeast United States) than reanalysis, while being outperformed by reanalysis in areas of more complex terrain. Degradation of performance of the satellite based products including TRMM in complex terrain relative to flatter areas was also found by Kim et al. (2017) during the pre-monsoon and monsoon seasons in far-east Asia. Despite this relatively poorer performance in regions of complex terrain TRMM data were found to be sufficient to force a hydrological model in Bhutan (Xue et al., 2013), illustrating the usefulness of satellite rainfall products to investigate data sparse regions. Additionally, Arabzadeh et al. (2020) also noted that the differences between reanalysis and satellite based products was largest in data sparse regions such as South America, and that ERA5 outperformed MERRA2. ERA5 was also found to outperform MERRA2 in India (Mahto and Mishra, 2019). When examining extreme precipitation specifically many studies found that both reanalysis and satellite based products underestimated heavy precipitation events and overestimated lighter and moderate precipitation events when compared to gauges in a variety of regions and scenarios including Bolivia, regions frequently impacted by atmospheric rivers, China, Iran, and India (Blacutt et al., 2015; Arabzadeh et al., 2020; Fang et al., 2019; Taghizadeh et al., 2021; Gupta et al., 2020). A study examining all precipitation events found when events seperated by a minimal time period of dry weather between raining periods, IMERG matched event totals well, but did so by overestimating duration and underestimating intensity. Despite this drawback in the representation of extremes, Donat et al. (2014) found that trends in extremes derived from reanalysis datasets including ERA-Interim were consistent with ground based observations of the same variables. Lavers et al. (2022) notes the importance of ERA5 QPE to the forcing of hydrologic models, and finds that ERA5 precipitation is more reliable in the extratropics than the tropics, with the area to be examined in this paper lying in a transition zone between these two latitude bands. These results suggest that despite the limitations of reanalysis and satellite derived QPE, these datasets can still be used to discover

important aspects of the nature of extreme precipitation events in data sparse regions around the globe. This chapter will examine rainfall extremes at the 99th and 99.9th percentiles occurring in the data sparse region of central Argentina. Section 2 examines the value of the 99th and 99.9th percentiles, correlation and event overlap between datasets. Section 3 investigates the diurnal and seasonal frequency of events. Section 4 investigates differences in the thermodynamic environment during events in each dataset as represented by MERRA2 and ERA5 reanalysis. The variables chosen for this analysis are precipitable water (PWAT), convective available potential energy (CAPE) and convective inhibition (CIN) associated with events. Extreme precipitation is often associated with PWAT values well above climatological averages (Kunkel et al., 2020), and most precipitation in subtropical Argentina summers, when PWAT is highest, is known to result from convective storms which are impacted by the CAPE and CIN (e.g. Durkee et al., 2009; Cavalcanti, 2012; Rasmussen et al., 2016). The CAPE variable used for this study is the natively calculated CAPE in ERA5, produced by calculating the CAPE of parcels starting at progressively lower levels from 300hPa to the surface and retaining the highest CAPE that is calculated during this procedure. MERRA2 does not produce a standalone CAPE variable as part of the dataset. Taszarek et al. (2020) calculated CAPE directly from ERA5 and MERRA2, without using the natively calculated CAPE from ERA5, and found that CAPE from ERA5 matches observed radiosondes better than MERRA2. Knowledge of the differences in extreme event depiction between datasets is important for understanding the possible biases tied to the choice of precipitation dataset in such an analysis.

2.2 Data

This study explores the differences between the events identified as an extreme amount of precipitation (above the 99th or 99.9th percentile for all three hour periods) in the four datasets. These datasets were chosen for their relatively high spatial resolution, high (three hour or better) time resolution and complete coverage of the tropics and mid-latitudes, which allow them to be used for detailed analysis of extreme precipitation events. MERRA2 and ERA5 are both reanalysis datasets using model initialization to estimate rain rates, while IMERG and TRMM utilizes satellite ob-

servations paired with calibrated algorithms to estimate rain rates. The TRMM algorithm works as follows (Huffman et al., 2010): first the available microwave radiometer datasets are calibrated using the TRMM microwave radiometer and precipitation radar and combined to produce a rain rate estimate. Then an infrared satellite estimate is produced using the infrared satellite brightness temperatures calibrated to microwave rain rate estimates. The microwave radiometer estimates are used where there is enough data to create them and the infrared satellite estimates where there is not. Finally, these estimates are scaled to monthly gridded gauge data. IMERG works much the same way, with some differences. The largest of these is that the microwave estimates are calibrated to GPM instruments rather than TRMM instruments, and the infrared satellite estimates are provided by PERSIANN-CCS rather than microwave calibrated IR (Huffman et al., 2015). The precipitation estimates are still scaled to monthly gauge data. The MERRA2 precipitation variable used in this study is also scaled to monthly gauge data, and this procedure as applied to MERRA2 is described in Reichle and Liu (2014). The data used in this study covers the period between 1 June 2000 and 1 June 2015. The temporal start and end points were chosen so that the start and end are not in the middle of a convective season, and the period ends in 2015 because after this time the TRMM satellite was deorbited. IMERG, relying on the Global Precipitation Mission satellite launched 27 February 2014, had just begun at the end of the period, and data for the earlier period is based on applying the IMERG algoritms to TRMM data. Looking at a period where both these datasets were being produced allows for an anlysis of the level of continuity in identification of extreme rainfall events between the two datasets in Argentina. Before regridding, the data were aligned to the accumulation periods of TRMM, the dataset with the coarsest temporal resolution (three hour periods). The three hour periods end on half hours starting at 0130 UTC. When summing the MERRA2 and ERA5 precipitation, which has hourly temporal resolution ending on the hour, the total amount of precipitation during the hour containing the end of the TRMM accumulation period was divided by two and equally applied to the end of the current TRMM accumulation period and beginning of the next one. To compare extreme values in the different datasets after the summation each dataset was conservatively regridded to the MERRA2 resolution, as it is the

dataset with the coarsest resolution: 0.625 degrees longitude by 0.5 degrees latitude. Conservative regridding results in a regridded dataset that retains the same amount of precipitation mass as the original dataset, an important consideration when comparing precipitation amounts across datasets with different resolution. After regridding, the 99th and 99.9th percentile is determined at each gridpoint for each dataset in the domain 44° S to 26° S and 74.375° W to 56.875° W. These percentiles are based on every three hour period during the 15 year study period between 1 June 2000 and 1 June 2015, resulting in 44 identified events per gridpoint above the 99.9th percentile and 439 events per gridpoint above the 99th percentile.

2.3 Percentile Thresholds, Correlation and Event Overlap

The first point of comparison between the datasets is the value of the 99th and 99.9th percentile threshold. Fig. 2.1 and Fig. 2.2 shows these values at each gridpoint as accumulation during a three hour period. At the 99th percentile, the reanalysis dataset thresholds are very similar to one another at most locations, with MERRA2 generally slightly lower with the exception of the southern Andes mountains, where the ERA5 threshold is about 0.5cm $3hr^{-1}$ larger. Mahto and Mishra (2019) found that while both ERA5 and MERRA2 underestimated upslope precipitation in the western Ghats of India, MERRA2 had the greater difference, so it is possible that the lower thresholds at the 99th percentile in MERRA2 on the upstream side of the Andes are related to a bias in MERRA2 toward lower precipitation in upslope flow regions. Both TRMM and IMERG 99th percentile thresholds are higher than both reanalysis datasets by about 0.5cm per 3 hours in most locations, and have a very similar spatial structure to each other. At the 99.9th percentile threshold however, TRMM values nearly double those of MERRA2 and ERA5 in most locations, and also about a centimeter higher than IMERG. There is also a clear land-sea contrast in threshold values in TRMM and IMERG off the southeastern coast that is not present in the reanalysis datasets, and particularly evident in IMERG. This is a known problem for datasets based on microwave radiometers, due to retrievals being much more difficult over land than the ocean, as discussed in Petty and Li (2013). The correlation between all rainfall in each dataset was also investigated. Fig.

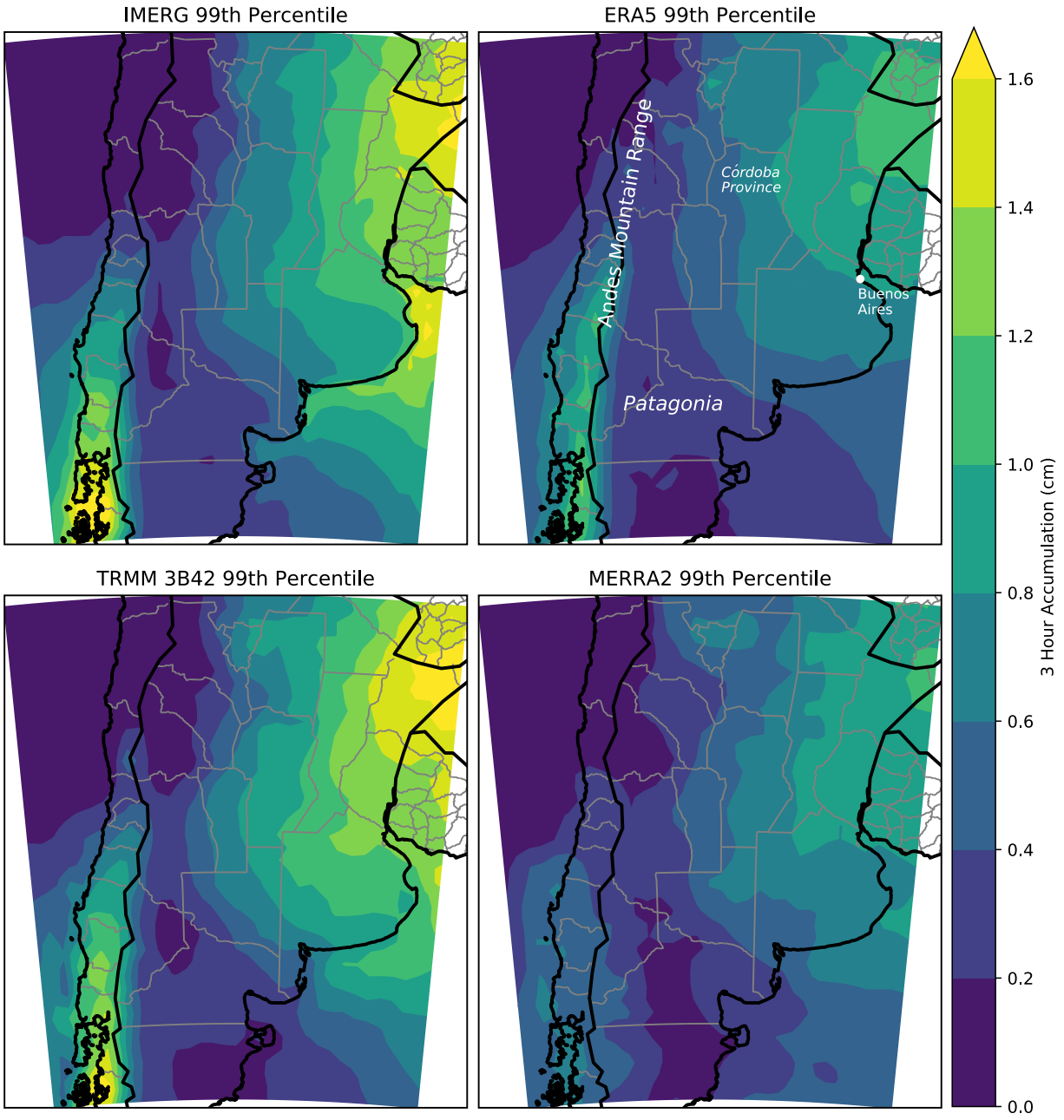

Figure 2.1: Map of the value of the 99th percentile threshold at each gridpoint for each dataset. Geographic locations mentioned in the text are labeled on the ERA5 plot.

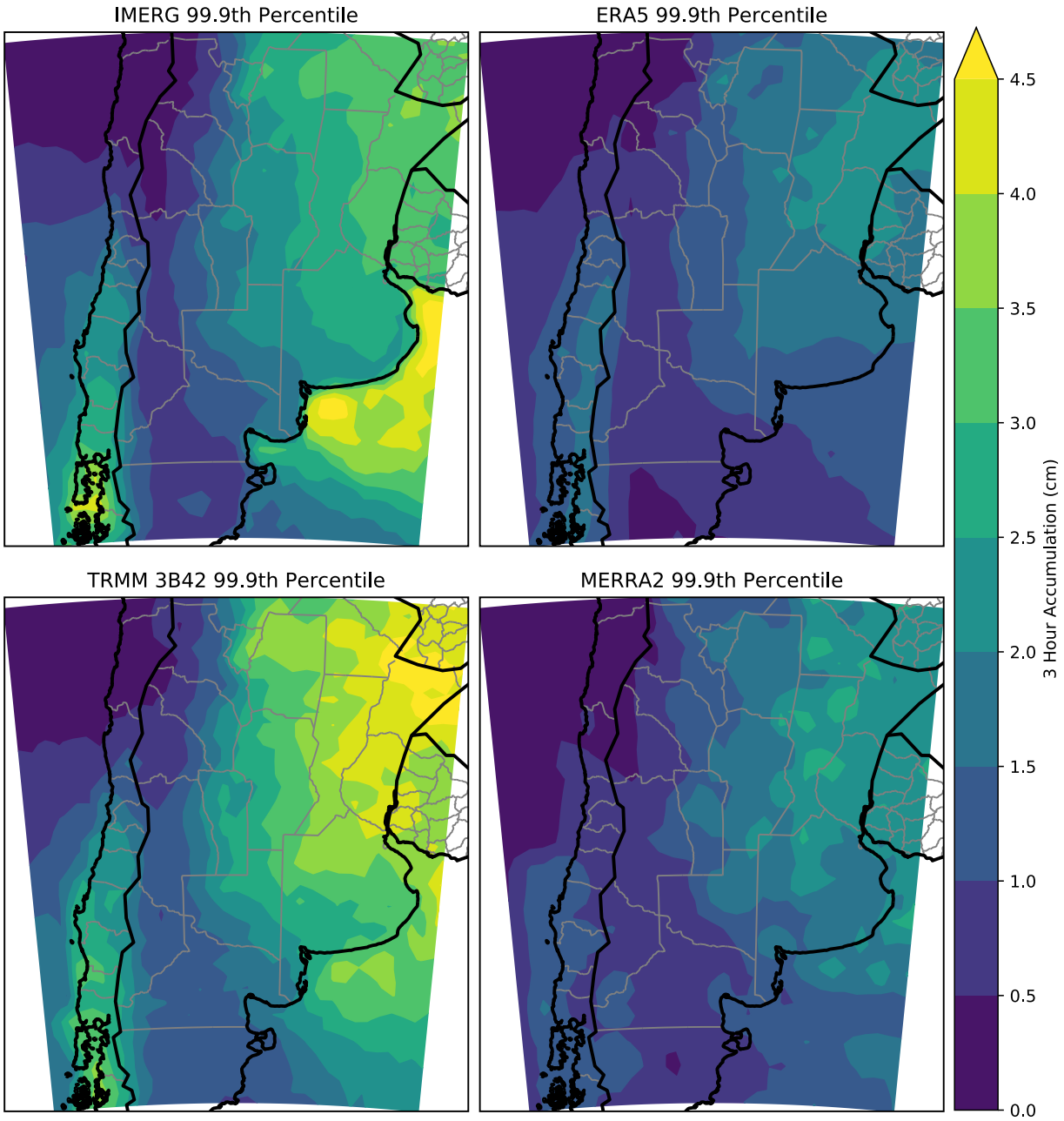

Figure 2.2: Note new colorbar levels, otherwise as in Fig. 2.1 but for the 99.9th percentile.

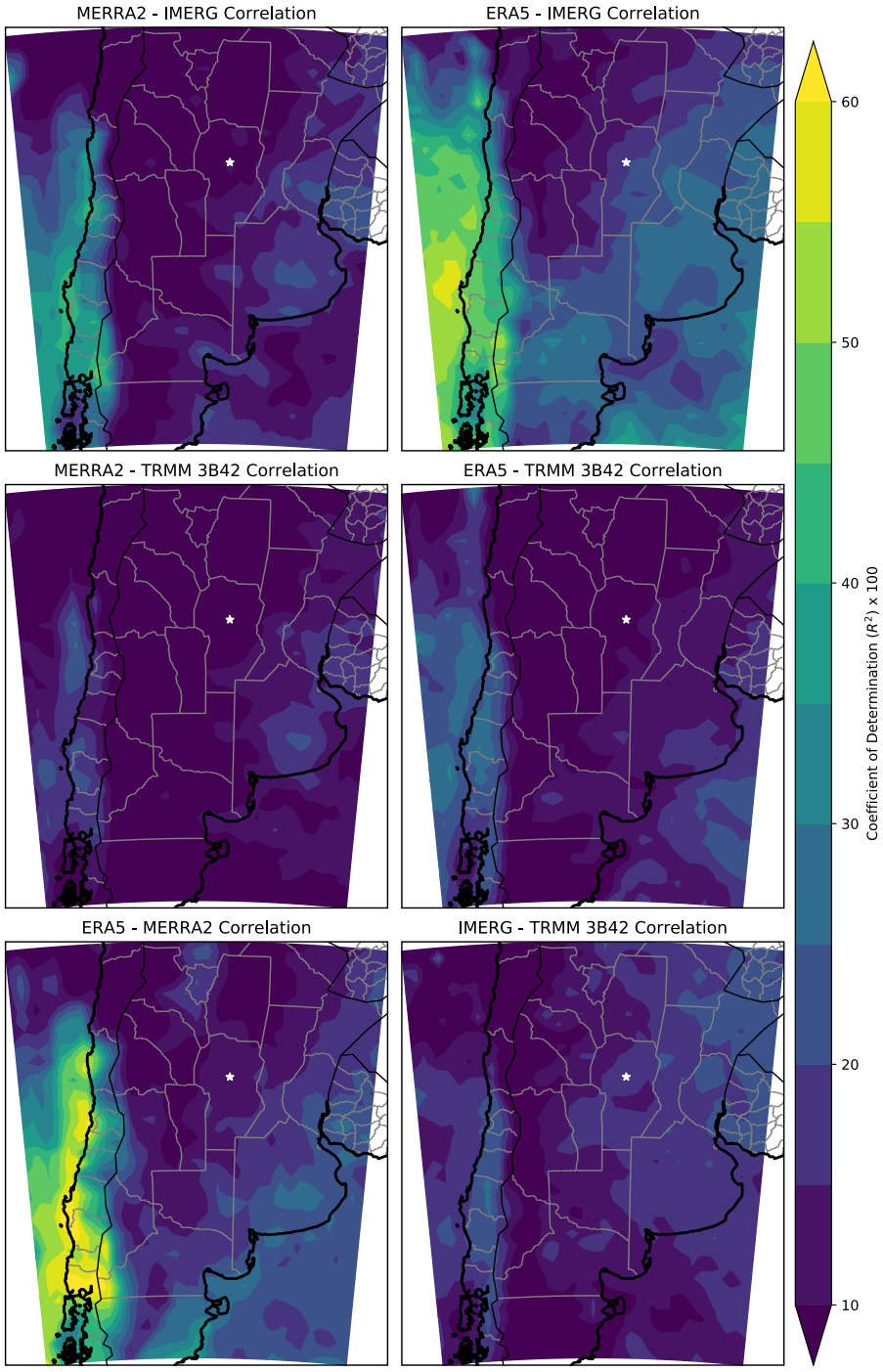

Figure 2.3: Map of the coefficient of determination (R^2) value x 100 at each gridpoint in the study domain for each possible pair of datasets. The location of gridpoint used for the scatterplot in Fig. 2.4 is marked with a white star

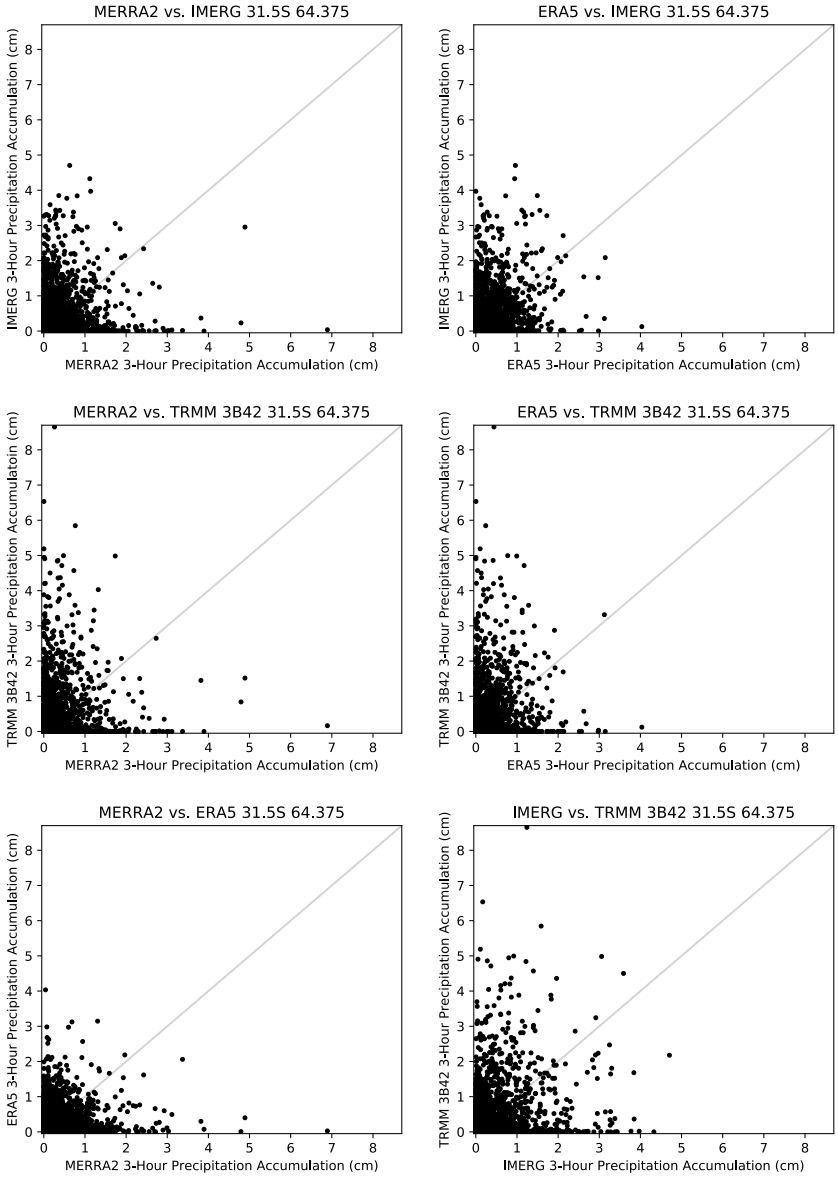

Figure 2.4: Scatter plots of each combination of datasets at 31.5° S 64.375° W, the location noted by the star in Fig. 2.3.

2.3 shows the coefficient of determination (R^2) between each possible pair of datasets and Fig. 2.4 shows the corresponding scatter plots for one gridpoint. The R^2 values indicate that while ERA5 and IMERG and ERA5 and MERRA2 are the two best correlated pairs of datasets, none of the datasets is particularly well correlated with another. The R^2 values in Córdoba province (location of the white star in Fig. 2.3) are at a maximum in the ERA5 and IMERG pair at a value between 0.2 and 0.25, which equates to a correlation coefficient of 0.4 to 0.5. For context, most of the 26 datasets studied by Beck et al. (2019) were found to have a median gridpoint correlation coefficient value with the Stage-IV radar and gauge analysis of 0.6-0.7, corresponding to an R^2 value of 0.36 - 0.49. Specifically, IMERG and MERRA2 were found to have median correlation coefficients with Stage-IV just below 0.8, ERA5 just less than 0.7 and TRMM 3B42 just above 0.6. Thus it can be seen that the best correlation values in Córdoba province between each pair of the datasets examined in this study are lower (and in some cases much lower) than those found for these same datasets and the Stage-IV dataset in the United States. Fig. 2.4 illustrates why this is the case. Many points in these scatter plots fall close to either the x or y axis, where the ratio of rainfall between datasets is high. A key question for a researcher seeking to compile a list of events is: Are these differences at higher levels of accumulation due to events being relatively independent of one another, or the result of small spatial and timing differences?

Fig. 2.5 and Fig. 2.6 answer this question. These figures illustrate the percentage of events above the given percentile threshold in both datasets that do not overlap with the other dataset within one gridbox and/or one time period. For example, for the 99.9th percentile, the total amount of events in both datasets is 88. If 22 events in dataset A and 33 events in dataset B have a corresponding event in the other dataset that occurred within a 3x3 gridpoint box (1.875 degrees longitude by 1.5 degrees latitude) centered on the gridpoint at the time of the event or one time period before or after, the percentage of events that do not overlap is $88 - (22 + 33)/88 = 0.375$. It is possible for the amount of events overlapping with the other dataset to be different because two events back to back in the same dataset can both overlap with one event in the other dataset. These maps thus allow for an analysis of the percentage of events between the two datasets that

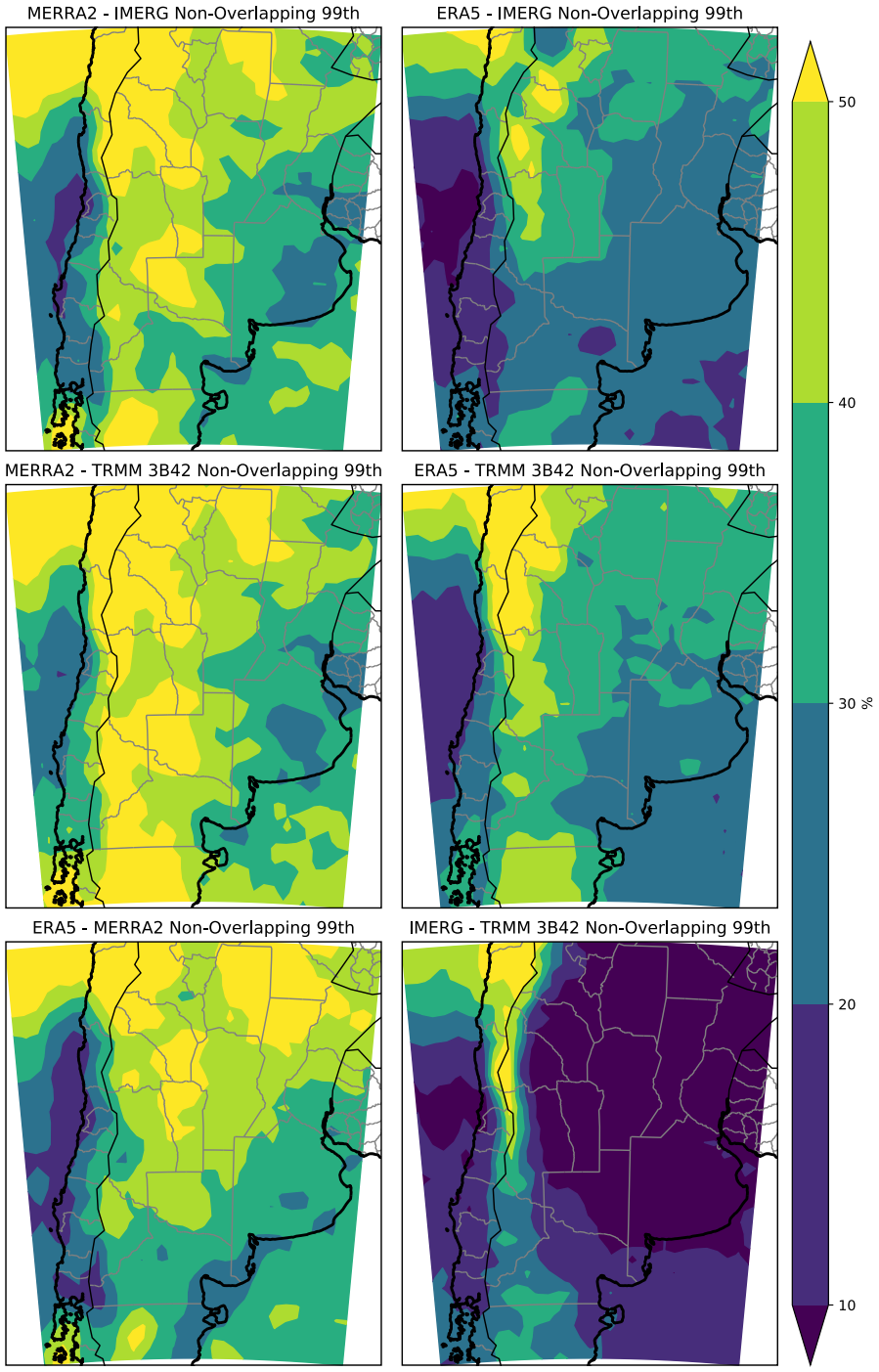

Figure 2.5: The percentage of 99th percentile events of the two compared datasets that do not overlap with an event in the other dataset within one gridbox spatially and/or one time period temporally.

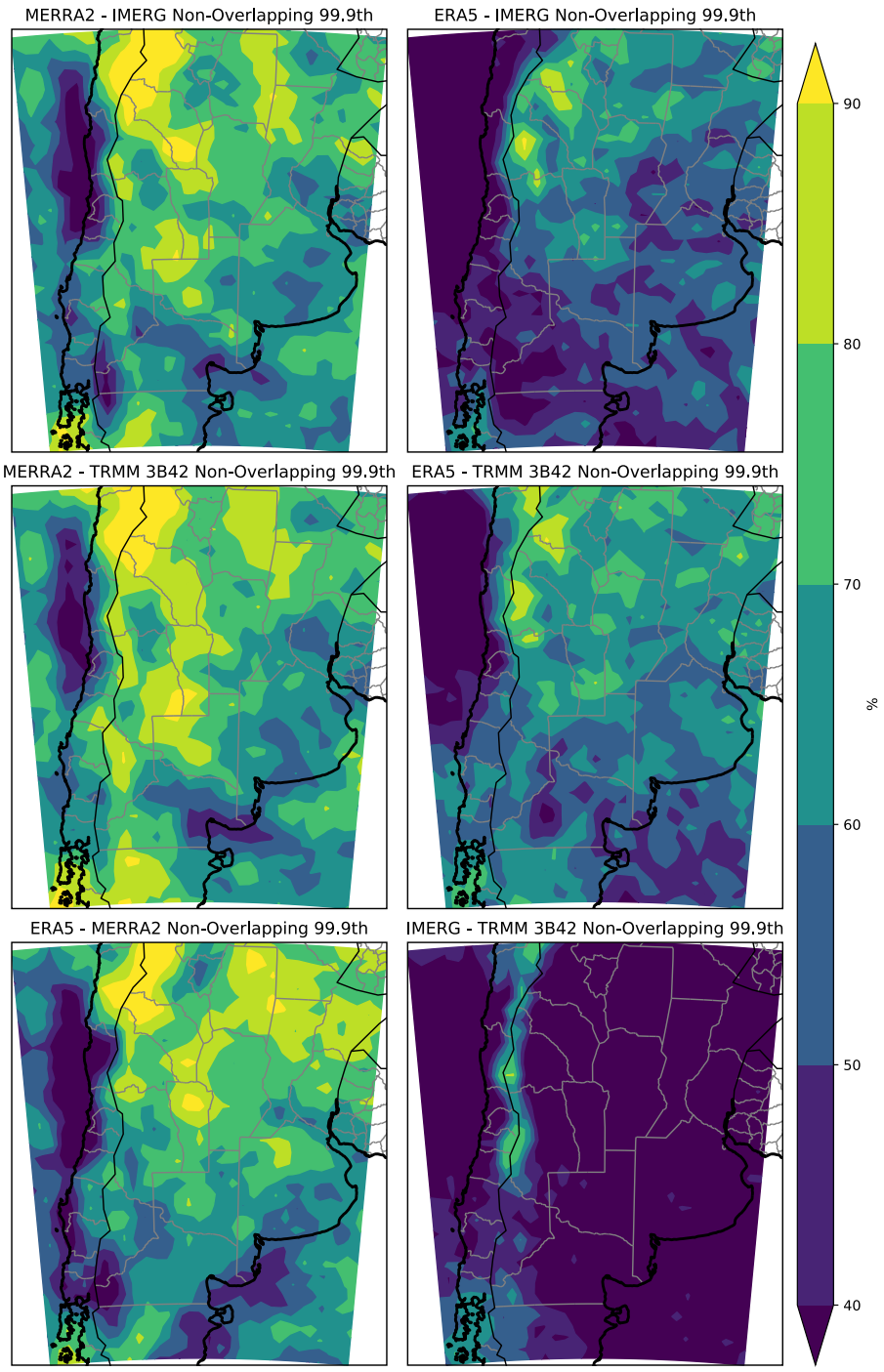

Figure 2.6: Note the different colorbar, otherwise as in Fig. 2.5 but for the 99.9th percentile.

are independent of each other in space and time as defined by the overlap criteria. At the 99th percentile percentages in the arid northeast part of the domain are the highest, and elsewhere between 30 and 50%, showing that for most areas less than half of events do not have a nearby in space or time counterpart in the compared dataset. The exception is TRMM compared to IMERG, where nearly all identified events have a counterpart, with the exception of the Andes crest, showing that instances with a high accumlation in one dataset and a high ratio between the datasets are nearly entirely due to small differences in space and timing. At the 99.9th percentile (Fig. 2.6 with a lower sample size the results are noisier. However, it is nonetheless apparent that the amount of events that do not overlap is much higher, as would be expected with a lower sample size. Most areas in each dataset comparison show over 50% of events not overlapping in space and time with the events in the corresponding dataset, with the highest values near the Andes. The exception is once again TRMM and IMERG, which show good agreement between time and location of events. Thus the reason many of the points off of the 1:1 line in Fig. 2.4 is not merely due to offsets in space and time between datasets, but rather due to rainfall occuring at different times in different environments meeting the percentile threshold to be considered extreme in each dataset. Therefore it can be seen that any list of extreme events compiled using these datasets, particularly at the 99.9th percentile, will have many dates that do not match with lists compiled from the other datasets, with the exception of TRMM and IMERG.

2.4 Seasonal and Diurnal Analysis

Fig. 2.8 shows the percentage of events that happen during the peak 30 day window shown in Fig. 2.7. Events are most concentrated seasonally along the eastern side of the Andes in the northern part of the domain, while to the south and east events are more evenly distributed throughout the year. Interestingly, the area noted earlier in south central Argentina with events in the spring has values of 10-15% except for MERRA2 where this most of the gridpoints in this region have maximum 30-day event counts 15-20% of the yearly total. This is likely because of the tendency of MERRA2 to record more events than the other datasets in strongly forced synoptic environments

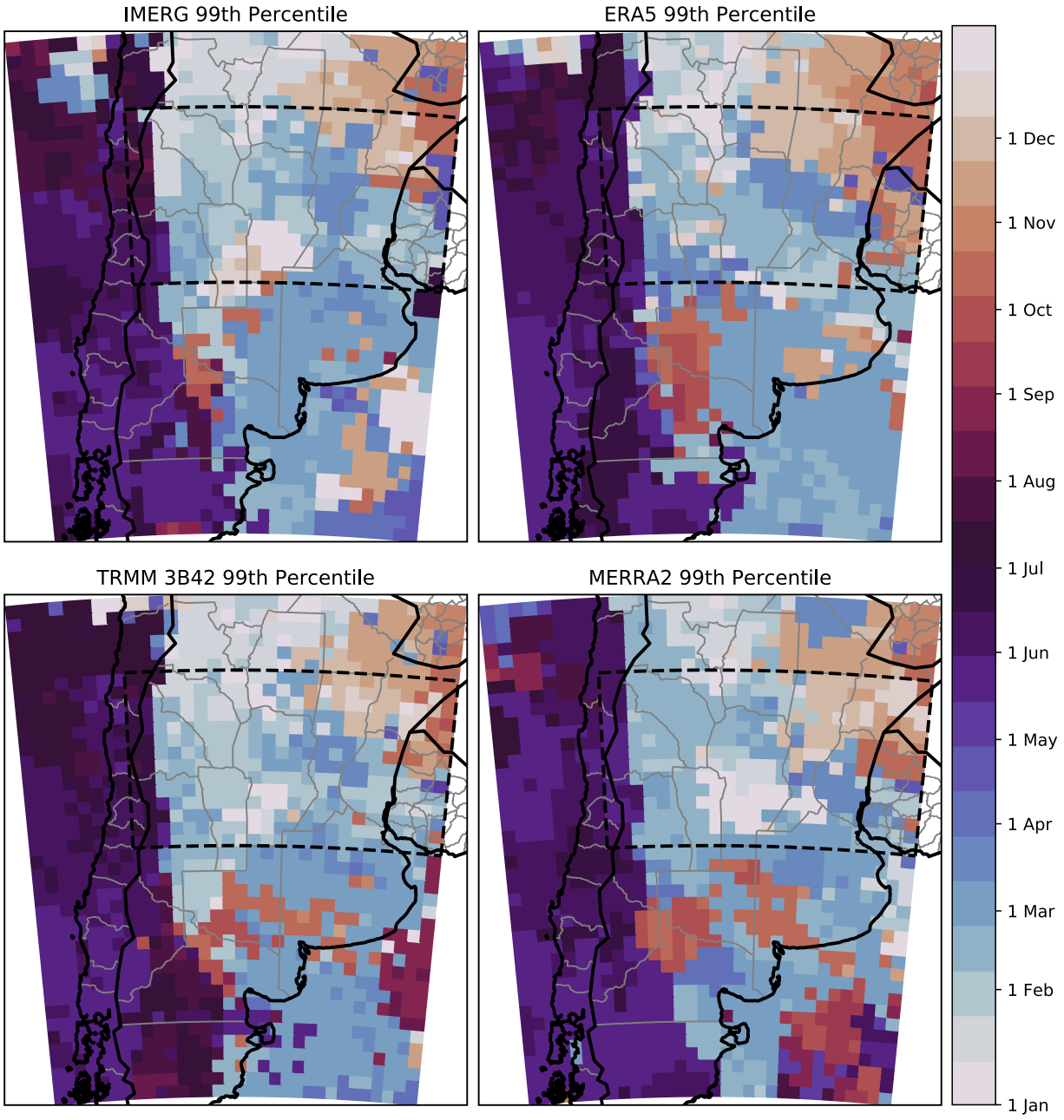

Figure 2.7: The day of year with the maximum 30-day running sum (15 days before and after date plotted) of 99th percentile events at each gridpoint. The dashed black rectangle outlines the region used for the construction of the Hovmöller plots in Fig. 2.11 and Fig. 2.12.

relatively lacking in moisture, which is further discussed in the next section. All areas show a stronger seasonality of events than would be expected if events were evenly distributed throughout the year. The region with the highest seasonality of events in the northern part of the domain is shown most clearly in IMERG and ERA5. IMERG (half-hour) has a higher native temporal resolution than TRMM (three hour) and ERA5 (0.1 x 0.1 degrees) has a higher spatial resolution than MERRA (0.5 x 0.625 degrees). These differences in resolution would lead to the detection of smaller and/or shorter lived systems in IMERG and ERA that are not resolved as well in TRMM and MERRA2.

The next question to be addressed is how well the datasets match in their representation of the seasonal and diurnal cycle of events. Fig. 2.7 shows the day of year when the 30-day running sum of events is maximized. The corresponding map for events above the 99.9th percentile threshold looks very similar, though with more noise (not shown). At the 99th percentile each of the four datasets show largely the same pattern with small variations. In Patagonia and west of the Andes, events occur during the Austral winter. The rest of the domain, where a large portion of rain is convectively driven, shows a general progression from late spirng and early summer in the north to late summer in the south. The exception to this is in south central Argentina where all datasets show an area where 99th percentile events peak in the spring. All datasets but TRMM retain this area at the 99.9th percentile. Based on case study analysis of selected events of this type (not shown), they are likely the result of convergence along a strong lee trough coupled with the increased moisture of the spring season resulting in the increased potential for rainfall in this small region during the early spring. In the northeast part of the domain there is a split between a preference for early spring events toward the coast and early summer events farther inland. A climatology of the South American Low Level Jet (SALLJ) by Montini et al. (2019) suggests that this split is likely due to the seasonal variability of the SALLJ, with the jet climatologically preferred to be stronger over the coastal regions in the fall and spring and stronger over the inland areas during summer. The results presented here also largely agree with the lightning climatology of South America as documented by Rasmussen et al. (2014). Their results show maxima of lightning frequency in

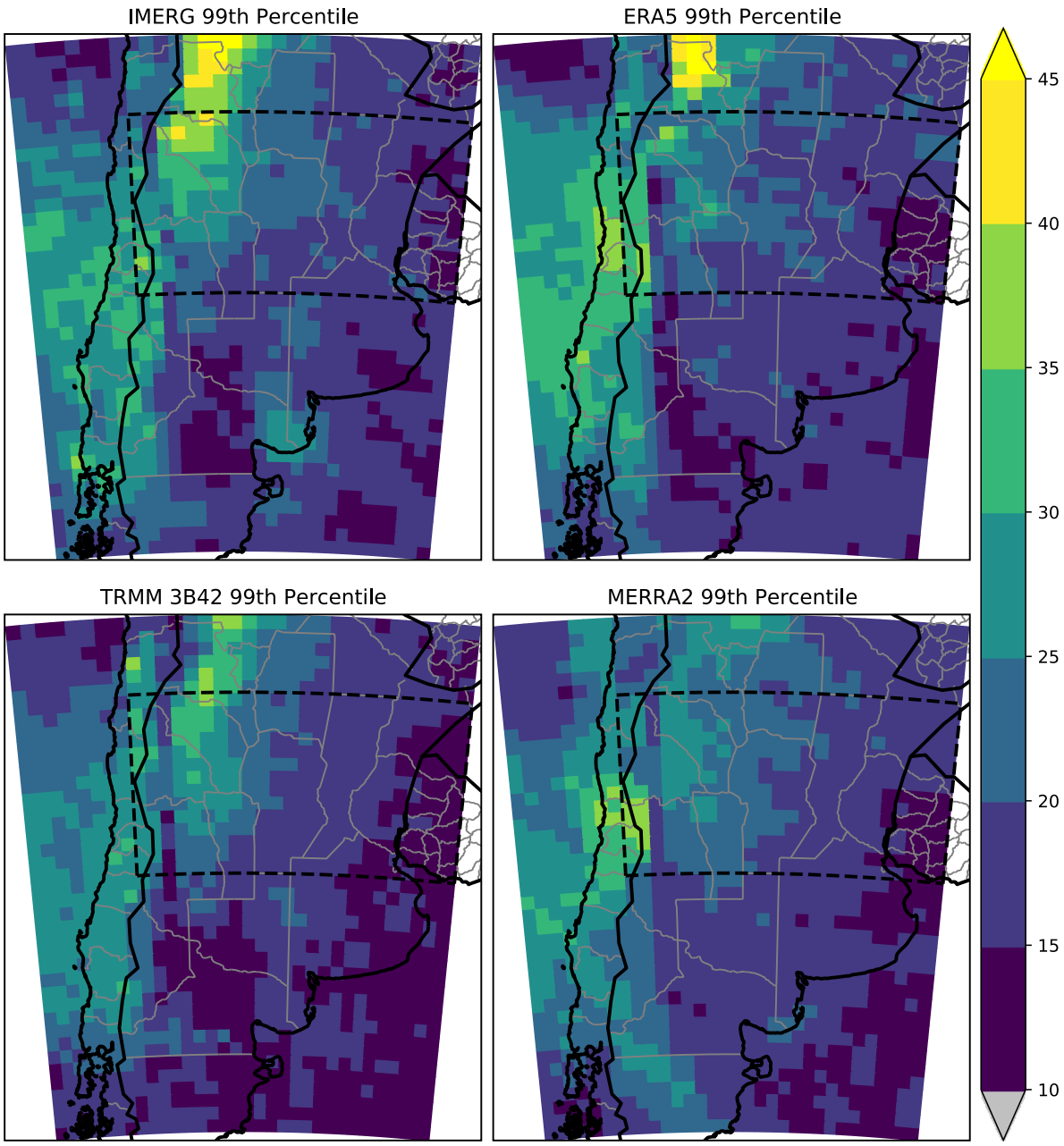

Figure 2.8: The percentage of events occurring during the maximum 30-day period plotted in Fig. 2.7 The dashed black rectangle outlines the region used for the construction of the Hovmöller plots in Fig. 2.11 and Fig. 2.12.

the northeastern part of the domain displayed in Fig. 2.7 during the austral autumn, coinciding with the maxima of three hour extreme rain events seen in that region during austral autumn. Lightning maxima during the early part of the austral summer (December and January) also match well. Lightning frequency during February and March is relatively low however, despite many gridpoints having event maxima during those months. Maximum flash rate then shifts back to the northeast, overlapping the region of April event maxima seen in Fig. 2.7. These results are encouraging because they show that despite the lack of overlap between specific events, the four datasets largely show the same climatology of events with minor differences and also match the climatology of lightning and the low level jet.

Many events in the datasets occur during consecutive or closely spaced three hour periods. To determine the extent to which this occurs the percentage of events in each gridpoint that end at least 24 hours after the end of the last event are plotted in Fig. 2.9. It can be seen that the two reanlayis datasets (MERRA2 and ERA5) contain a higher proportion of events occuring independently. Of note is that the area along the Andes in the northern part of the domain discussed in the previous paragraph with the highest seasonality of events in IMERG and ERA5 contains a relative maxima of independent events in IMERG and ERA5, and a relative minima in TRMM and MERRA2. This is supportive of the hypothesis that higher native temporal resolution in IMERG and higher native spatial resolution in ERA5 than TRMM and MERRA2 respectively allows IMERG and ERA5 to resolve more shorter or spatially smaller events thus accentuating the seasonality of the region. While overall the percentage of events that are indpendent at any one gridcell is less than 50% in many areas, it can be seen in Fig. 2.10 that only including independent events does not dramatically change the overall seasonal pattern of events, indicating that weather systems that produce events in multiple three hour periods occur at the same times of year as events covering only a single three hour period.

The diurnal frequency of events was also compared for latitudes between 35° S and 28° S east of the Andes mountains (indicated in Fig. 2.7). This domain was chosen because it is the area of South America observed to have some of the most intense thunderstorms in the world

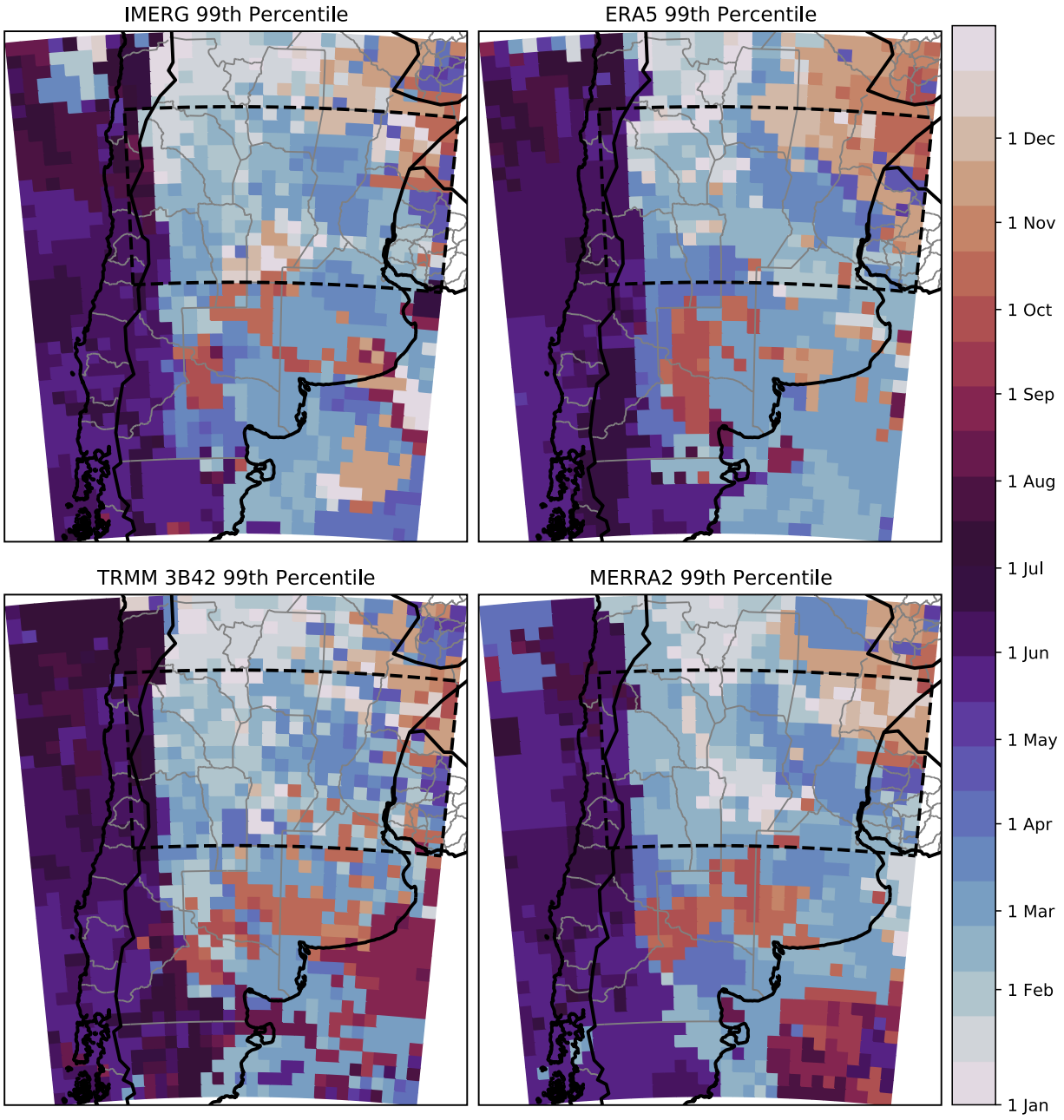

Figure 2.9: Same as Fig. 2.7 except only including events that ended more than 24 hours after the previous event ended. The dashed black rectangle outlines the region used for the construction of the Hovmöller plots in Fig. 2.11 and Fig. 2.12.

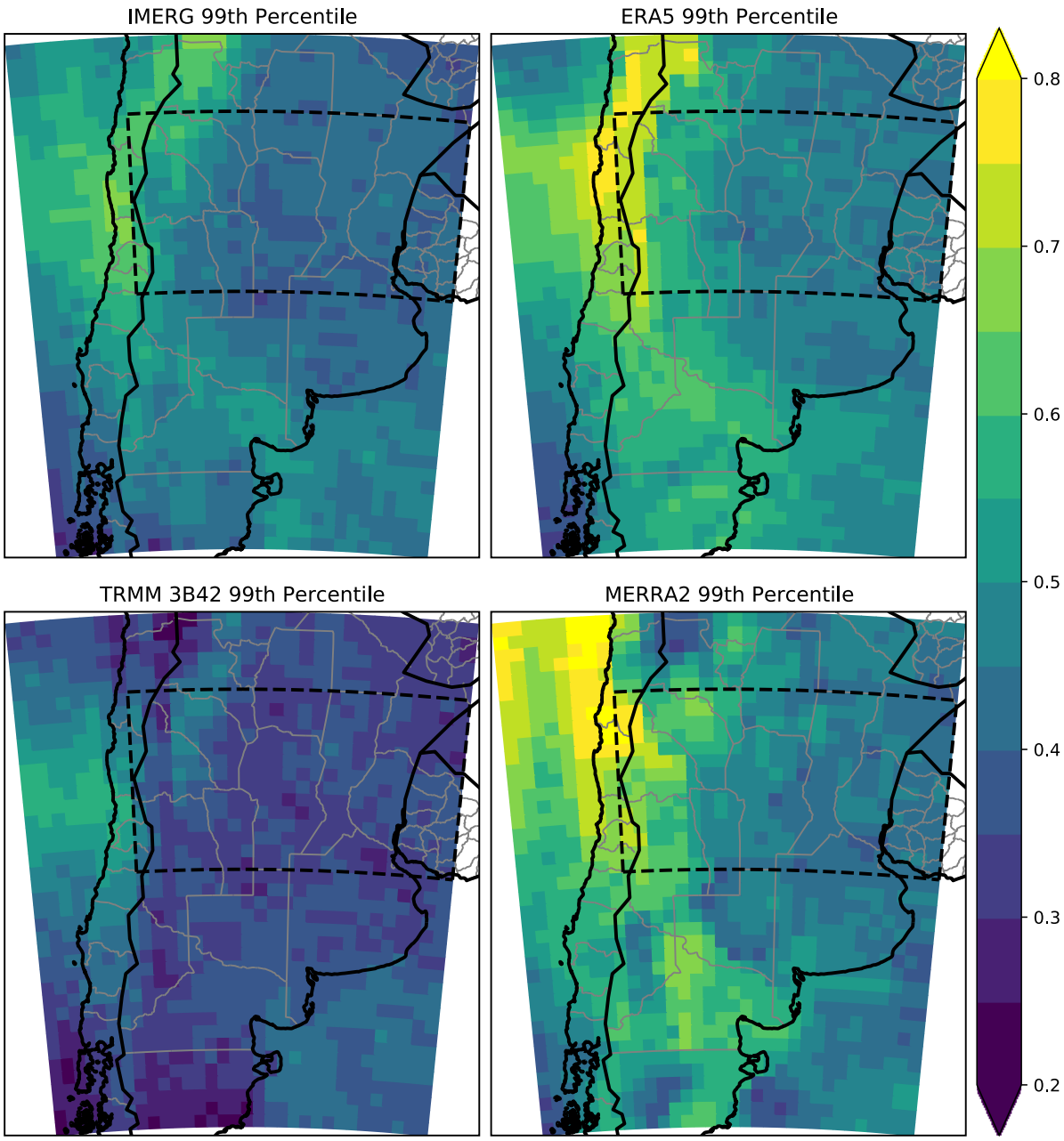

Figure 2.10: The percentage of events in each gridcell that end more than 24 hours after the previous event ended. The dashed black rectangle outlines the region used for the construction of the Hovmöller plots in Fig. 2.11 and Fig. 2.12.

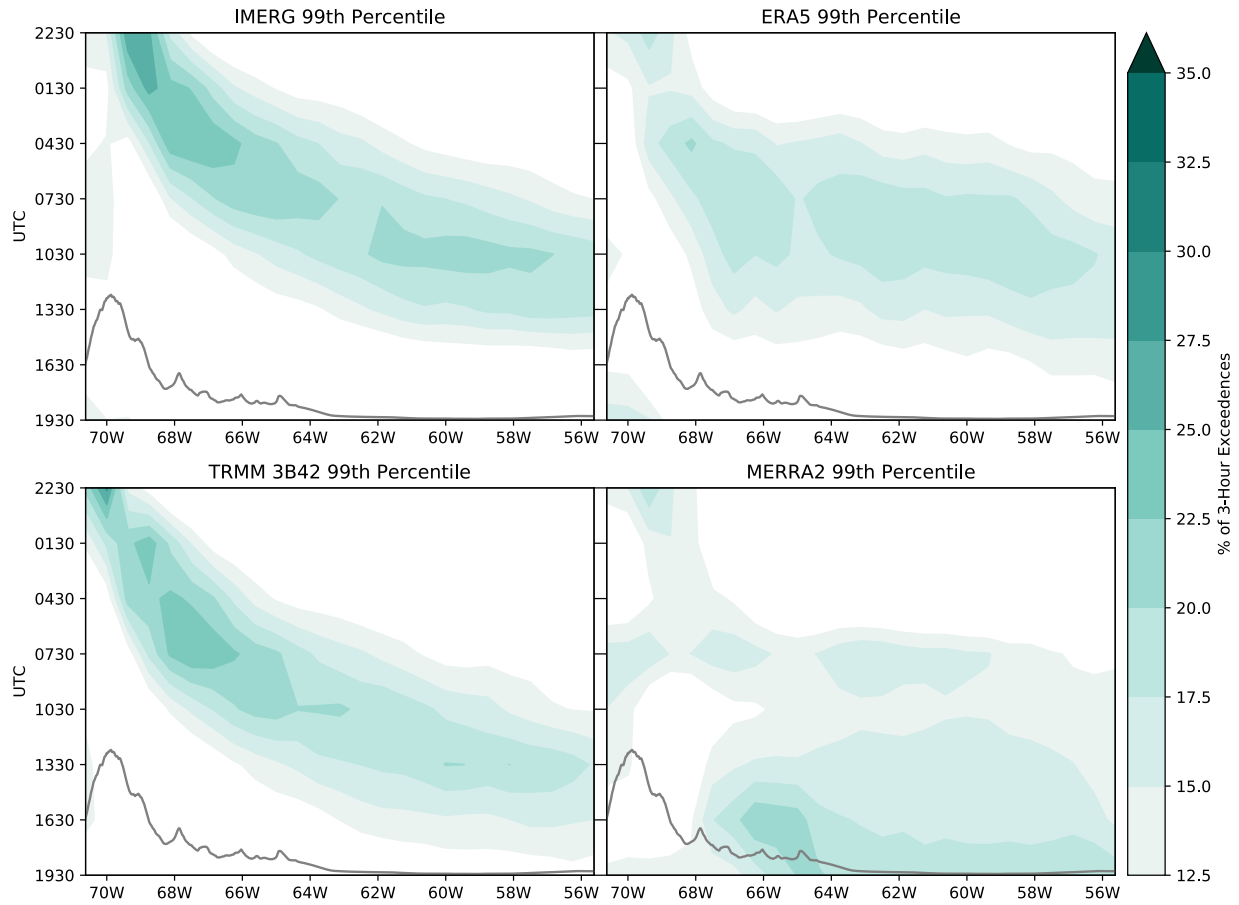

Figure 2.11: A Hovmöller plot indicating the average percentage of 99th percentile events between 35S and 28S ending at each time (y-axis) in each longitude band (x-axis). The grey line is the average topography in each longitude band, shown for reference. Local time is UTC-3.

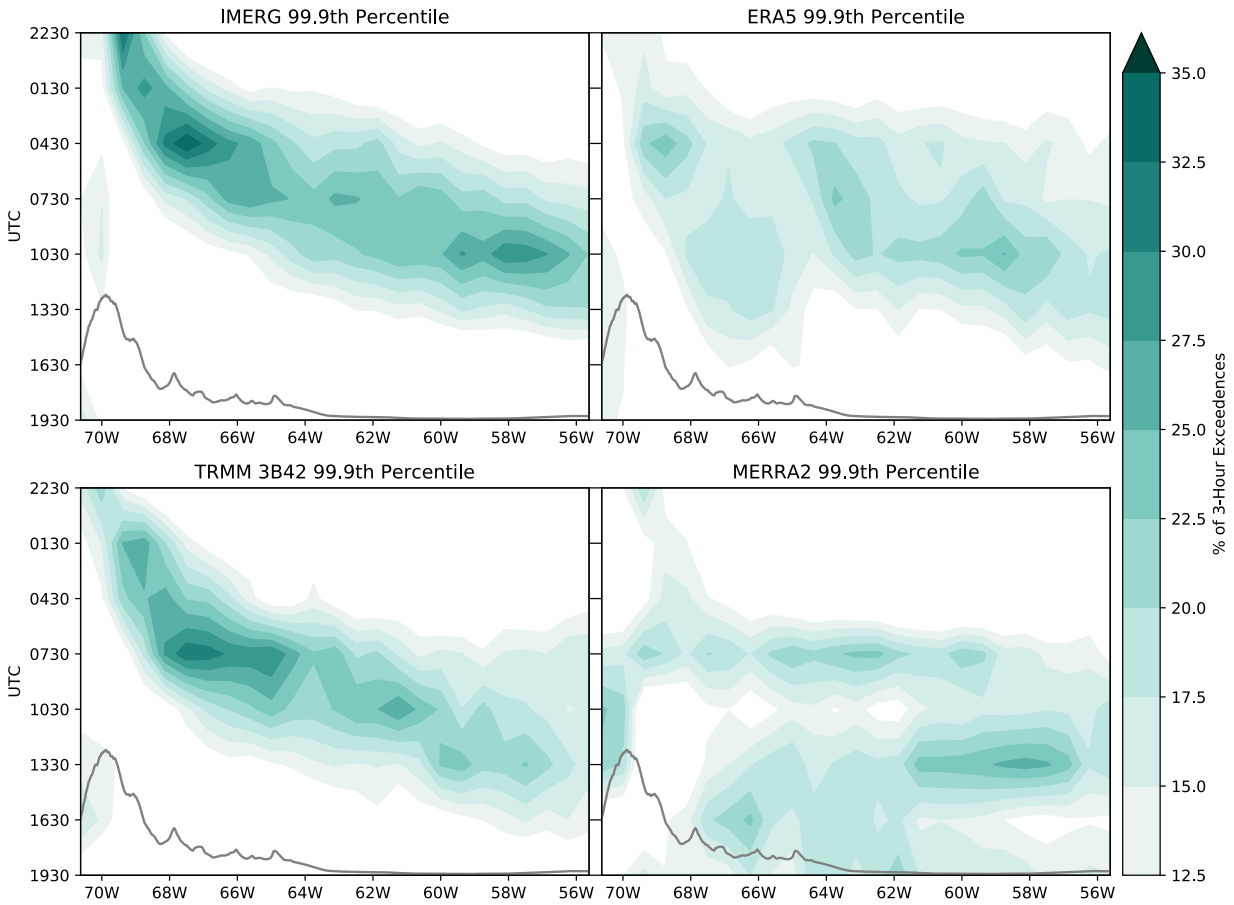

Figure 2.12: As in Fig. 2.11 but for 99.9th percentile events

by Zipser et al. (2006). Additionally, Mulholland et al. (2018) utilized a recently installed radar at Córdoba in this region (near the location of the scatterplots in Fig. 2.4) that provides a rare opportunity for in situ validation of the diurnal cycle observed in the four datasets based on the time of convective initiation. Fig. 2.11 and Fig. 2.12 show Hovmöller plots of the percentage of events ending at each time indicated on the x axis averaged across each latitude band indicated on the y axis. At both the 99th and 99.9th percentile thresholds, TRMM and IMERG show a well defined progression of the preferred time of event occurrence from west to east. However, TRMM shows this pattern occurring three hours later than IMERG, however. Villarini and Krajewski (2007) found that TRMM correlates best with 100-minute gauge accumulations starting 30 to 90 minutes before the midpoint of each three hour accumulation window. Foelsche et al. (2017) found that IMERG half-hourly rainfall estimates correlate best with 25 minute gauge accumulation beginning 10 minutes after the end of the nominal half hour period. Combined, these time offsets would contribute to the offset in time between TRMM and IMERG extreme events seen in the Hovmöller diagrams. In the Andes, events end most frequently in the late evening, and the preferred ending time is progressively later further to the east. At the Atlantic coast a preferred ending time in the early to mid-morning is observed. ERA5 events also follow this same general trend, but with lower magnitudes indicating that event times in ERA5 are more spread through the day than in the satellite products. Transition from late evening events to early-morning events also occurs over the Andes foothills in ERA5, instead of further east as in the reanalysis datasets. MERRA2 shows no well defined progression of events. Events in MERRA2 show a bimodal distribution, either ending in the early morning hours or the afternoon hours, with the afternoon being slightly more likely. The results from Mulholland et al. (2018) show that around Córdoba (at about 64° W) convective initiation shows a bimodal distribution with one peak between the early to mid afternoon hours and the other from the late evening to early morning hours. Rasmussen et al. (2014) also analyzed the diurnal cycle of deep convective cores, wide convective cores, and deep wide convective cores using criteria based on TRMM precipitation radar data. These results show deep convective cores and deep wide convective cores peaking around 0300 UTC for longitudes

between 65° W and 70° W, corresponding with the peak of three hour rainfall events in IMERG shown in Figs. 2.11 and 2.12. 0300 UTC is also the time that hail probability peaks at these longitudes (Bruick et al., 2019). The peak of wide convective cores in this latitude band occurs three hours later (Rasmussen et al., 2014). The results observed in the four analyzed datasets suggests that extreme 3 hour accumulations are more likely to occur during late evening to early morning three hour accumulation periods, coinciding with results reported by Rasmussen et al. (2014) that found an overnight peak in lightning in this same region using a lightning dataset based on polar orbiting satellites. Only MERRA2 shows a significant amount of events occurring during early afternoon accumulation periods, which agrees with previous literature noting that MERRA2 often does not represent the diurnal cycle well. Based on this prior research and the comparisons undertaken in this study it is likely that the peak in extreme three hour rain events in this region is indeed in the overnight hours, as recorded by IMERG, TRMM and ERA5 and that MERRA2 does not well represent the diurnal cycle of heavy rain producing convection in this region.

2.5 Comparison of Thermodynamic Environment

The events identified by the four datasets were also compared based on the values of PWAT, CAPE, and CIN they are associated with. These variables were chosen because they are important for extreme rainfall, and represent vertically integrated quantities, making them easy to compare between gridpoints without the need for multiple composites. Fig. 2.13 and Fig. 2.14 show the differences between the average PWAT during events for each pair of datasets, as represented by MERRA2's PWAT variable. The representation of PWAT in MERRA2 was chosen for the analysis presented here because MERRA2 was found to produce events in lower PWAT environments. Using the MERRA2 PWAT indicates that this relationship is due to differences in how each of the reanalyses produce precipitation and not merely a case of ERA5 precipitation being higher where ERA5 PWAT is higher, and MERRA2 precipitation being higher where MERRA2 PWAT is higher. Maps created using the ERA5 PWAT variable are similar and are not shown for brevity. For each dataset, PWAT amounts were assigned to events by using an average of the PWAT during the three

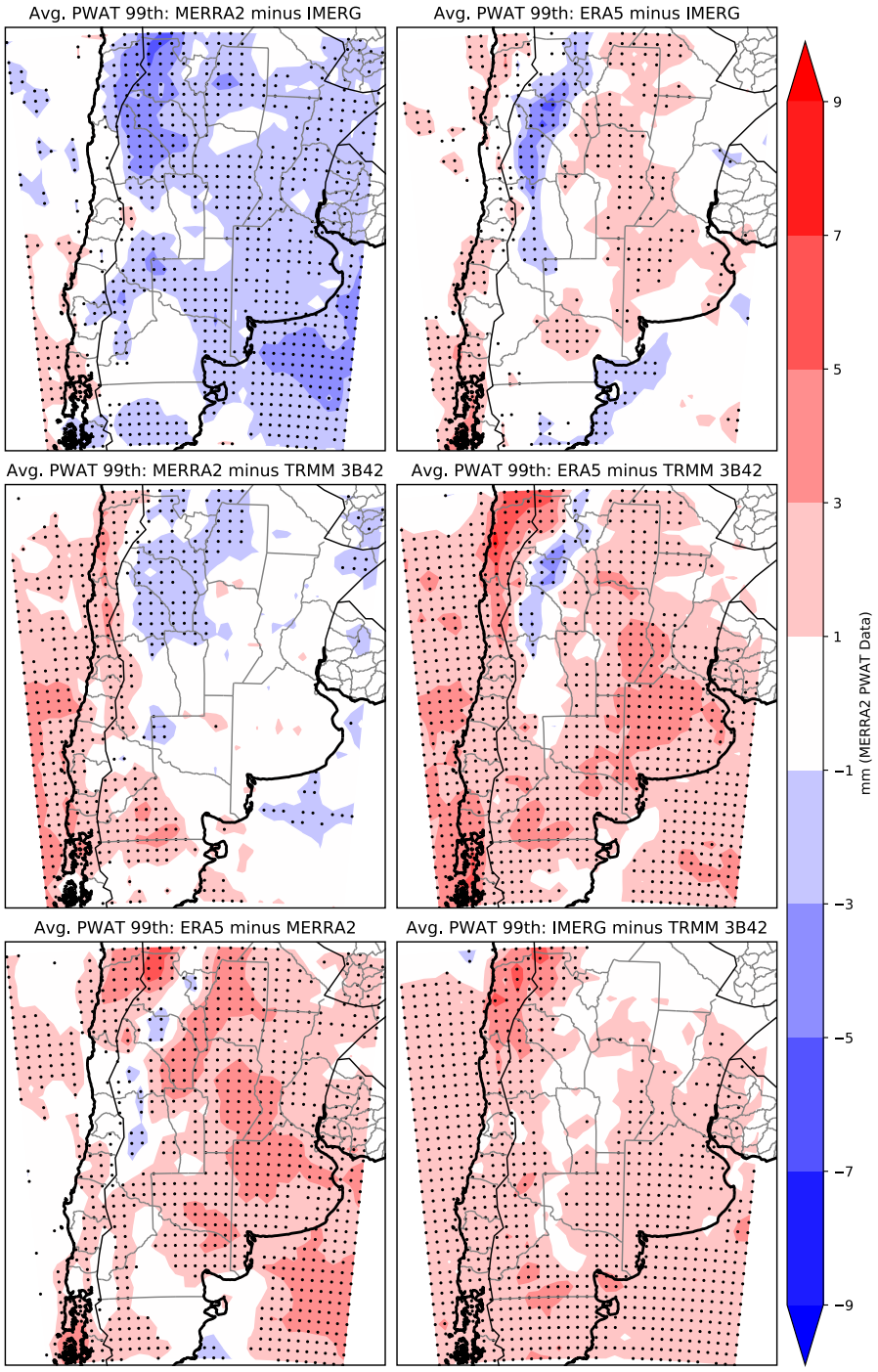

Figure 2.13: Difference in average PWAT during events between each pair of datasets at each gridpoint. Dots indicate significance at the 99% confidence interval using Welch's two-sample t-test. N = 439 events above the 99th percentile.

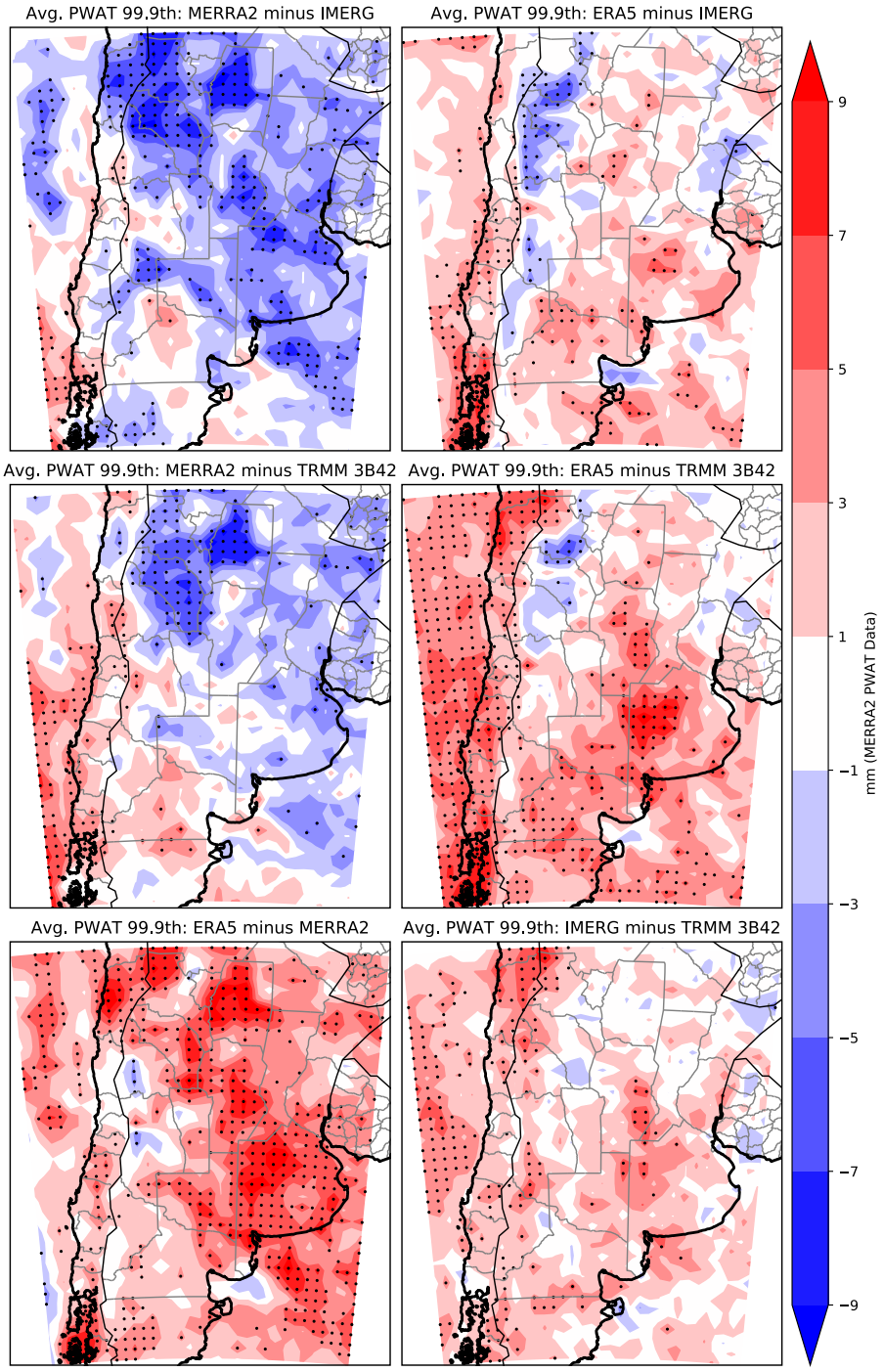

Figure 2.14: As in Fig. 2.13 but for 99.9th percentile events. N = 44 events above the 99.9h percentile.

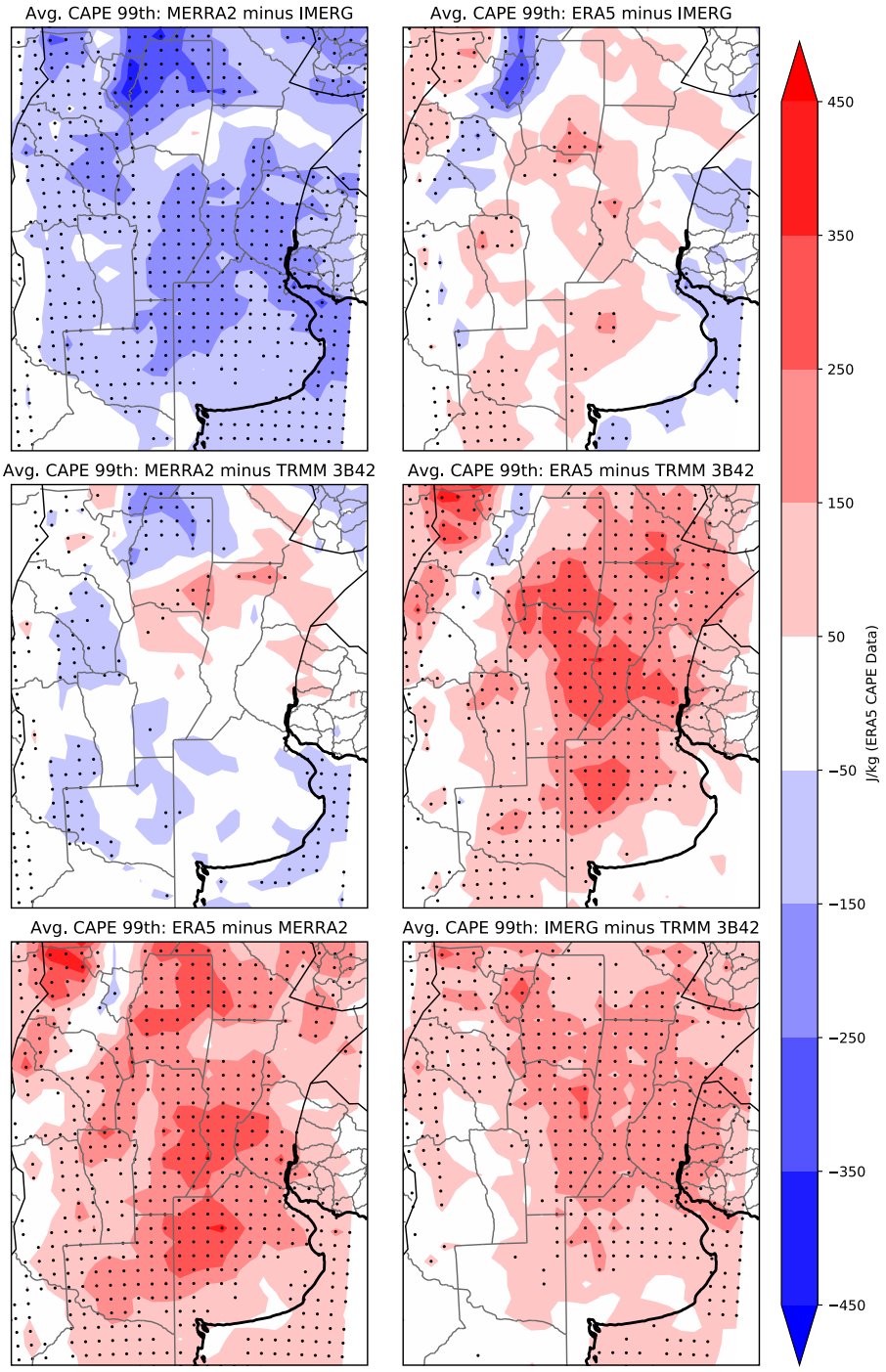

Figure 2.15: Difference in average CAPE during events between each pair of datasets at each gridpoint. Dots indicate significance at the 99% confidence interval using Welch's two-sample t-test. N = 439 events above the 99th percentile.

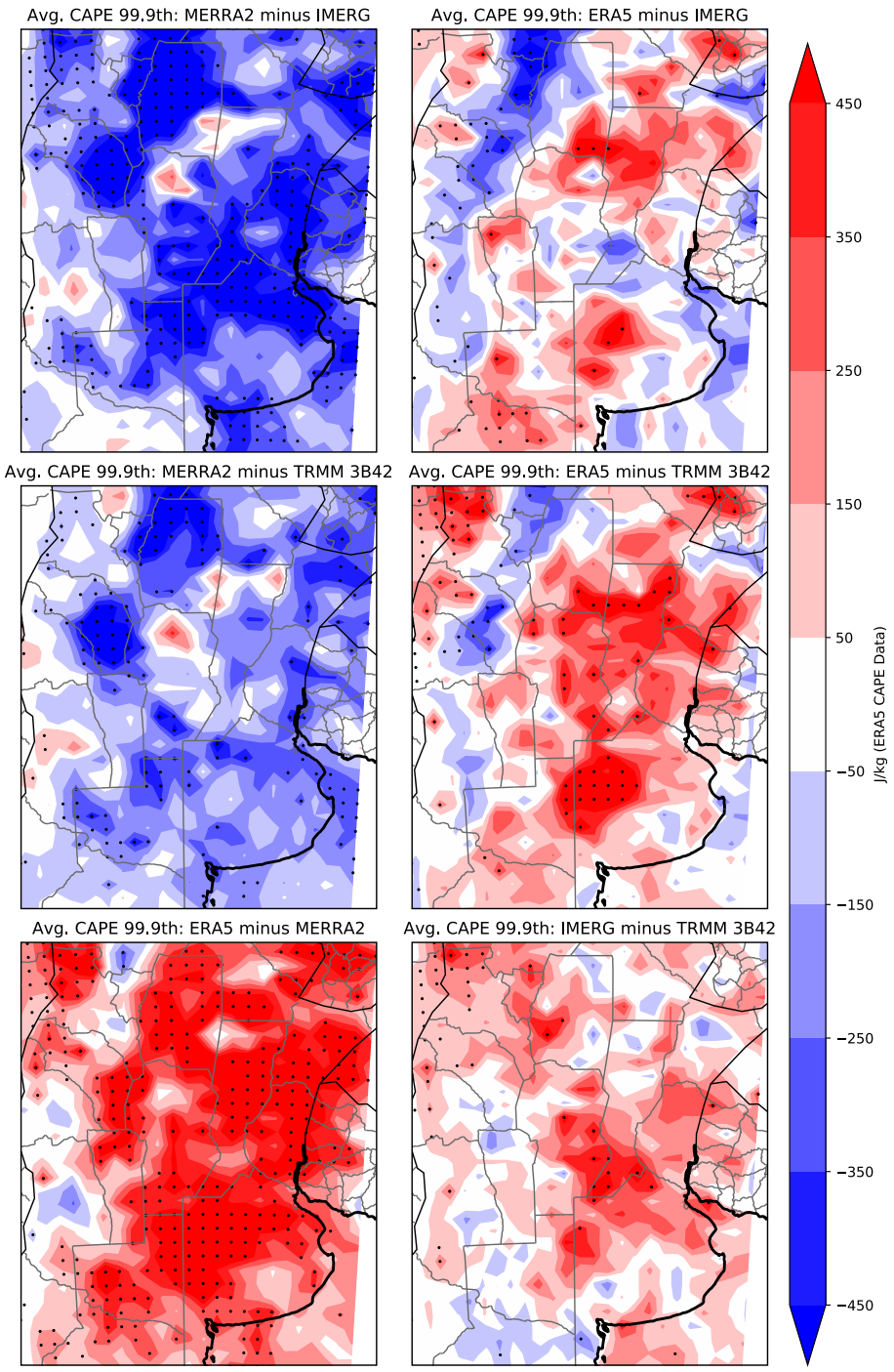

Figure 2.16: As in Fig. 2.15 but for 99.9th percentile events. N = 44 events above the 99.9h percentile.

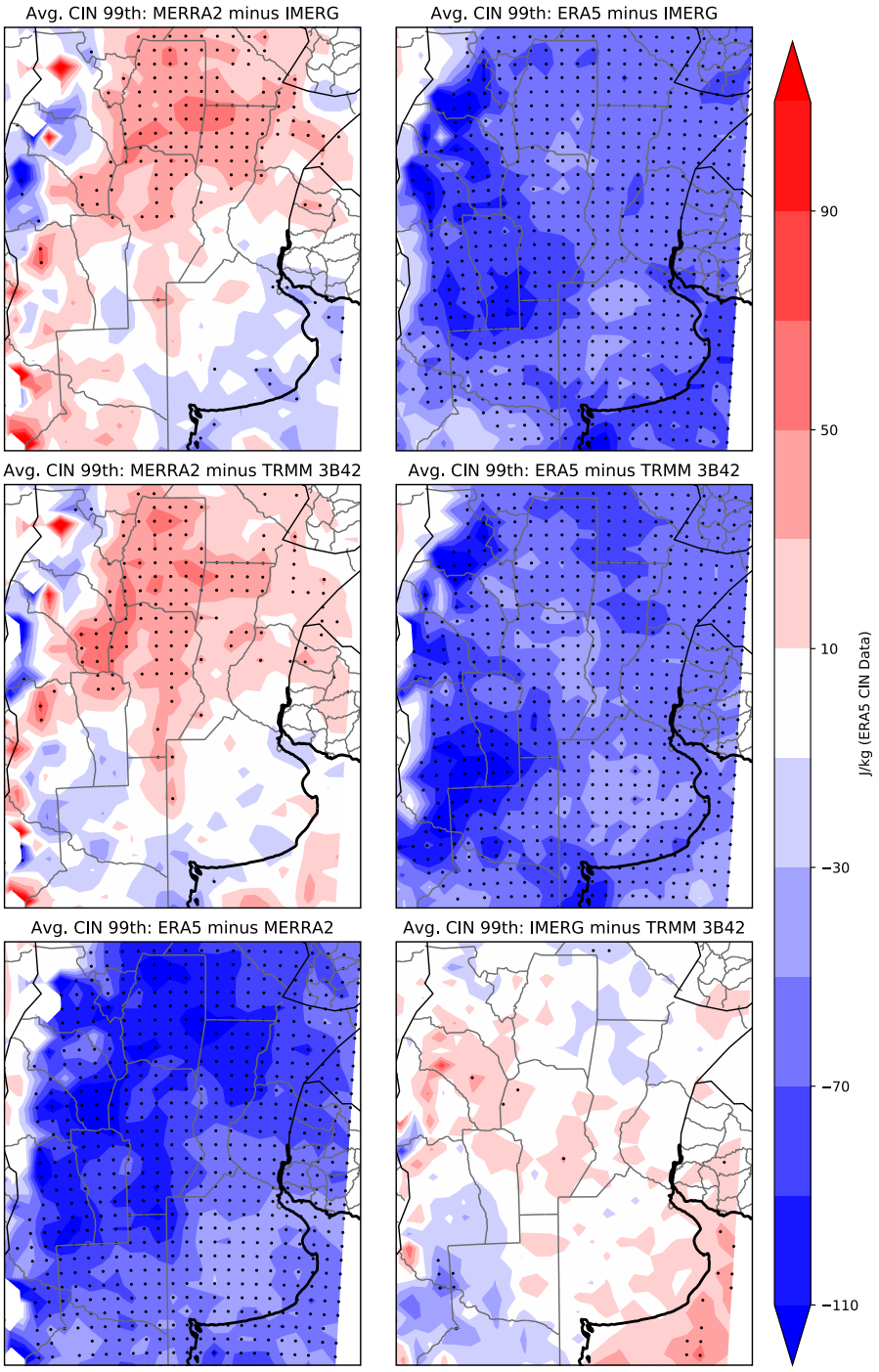

Figure 2.17: Difference in average CIN (positive value = more inhibition) during events between each pair of datasets at each gridpoint, using only events that occured in the presence of CAPE. Dots indicate significance at the 99% confidence interval using Welch's two-sample t-test. Sample size is variable between gridpoints because of the requirement that CAPE be present for CIN to be a meaningful thermodynamic variable.

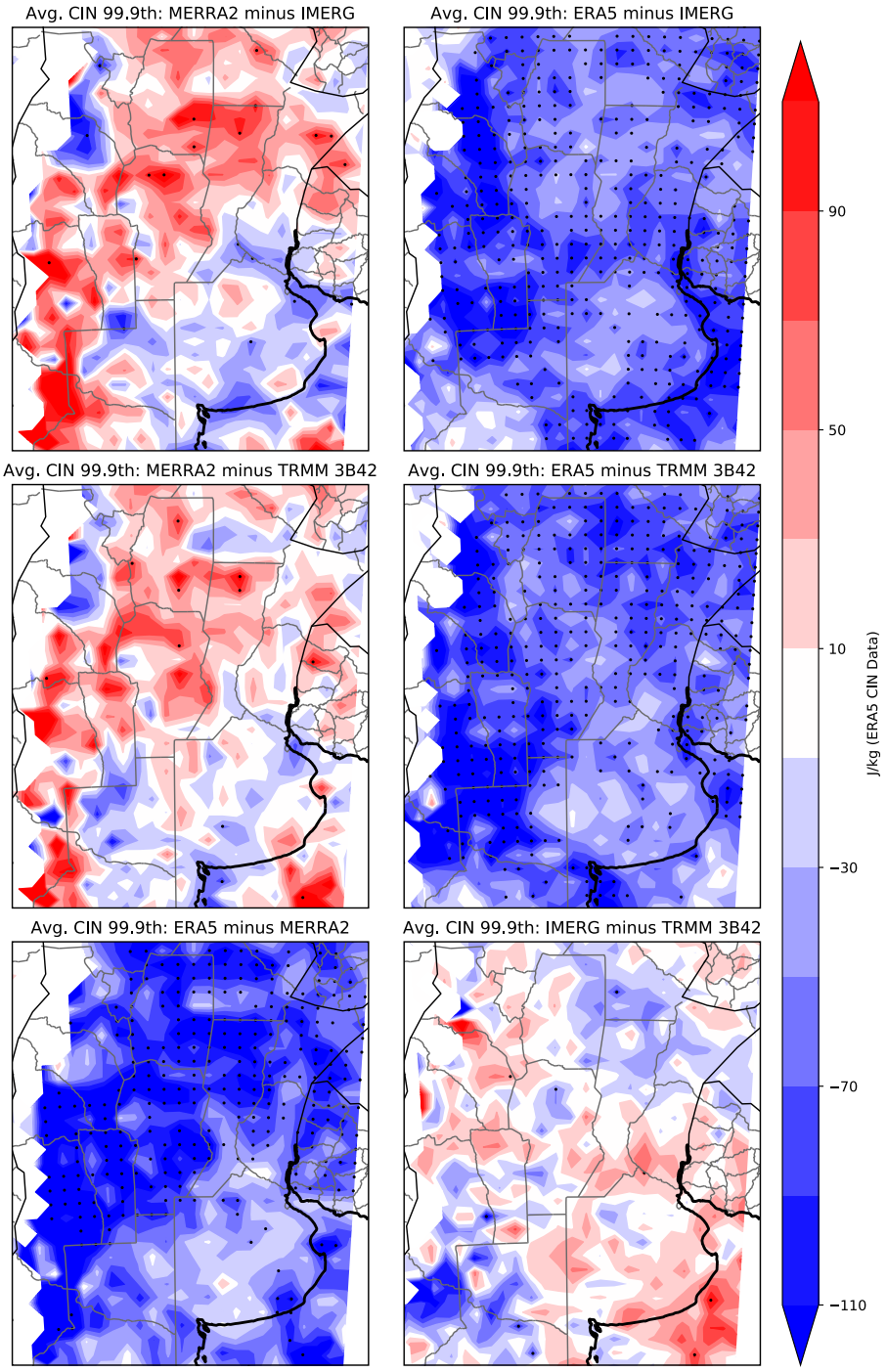

Figure 2.18: As in Fig. 2.17 but for 99.9th percentile events.

hour period that the event occurred. Patterns of PWAT difference between datasets look similar at both percentile thresholds. At both thresholds MERRA2 is associated with lower PWAT during events than IMERG and ERA5 and roughly the same amount of PWAT as TRMM events. ERA5 is generally associated with higher PWAT than the other datasets with the exception of arid areas in the northwest near the Andes. IMERG is the dataset that is the closest to the PWAT values of ERA5 events at most locations, particularly the regions around Córdoba province where convection provides a majority of rainfall. The difference between ERA5 and MERRA2 is up to 5mm for 99th percentile events and above 9mm for 99th percentile events at some locations, indicating that between these two datasets there are very significant differences in environment between events. Average PWAT during ERA5 events is between 40 and 50mm at gridpoints in this region, and thus a 5mm difference represents a 10-12% difference. These results show that MERRA2 indicates more events in environments that are more marginal for extreme precipitation as defined by PWAT. MERRA2 also produces more events in lower CAPE environments than the other datasets. CAPE represents the amount of buoyancy in the atmosphere if all latent heat is released in a rising parcel, and CIN represents the amount of energy the parcel would have to expend to become buoyant. The CAPE and CIN variables used here are taken from ERA5 because MERRA2 does not output them as variables, and when CAPE and CIN were calculated from the vertical profiles in each reanalysis ERA5 was found to have more fidelity to corresponding radiosonde observations (Taszarek et al., 2020). The differences in CAPE are shown in Fig. 2.15 and Fig. 2.16. At the 99th percentile it is clear that differences in CAPE largely follow the same patterns as the differences in PWAT, with ERA5 events on average occurring in higher CAPE environments than MERRA2 and TRMM, while not being significantly higher than IMERG events in many areas. At the 99.9th percentile the patterns are even more dramatic, with CAPE in ERA5 more than 450 J/kg greater than the average CAPE during MERRA2 events at many gridpoints, again indicating a significant difference in environment at these locations. Fig. 2.17 and Fig. 2.18 show the comparison of average CIN between events at both percentiles. ERA5 has significantly lower CIN (convection less inhibited) than both IMERG and TRMM, despite having about the same amount of CAPE as IMERG and

higher CAPE than TRMM. This suggests that perhaps there are events that are depicted in TRMM and IMERG that are not depicted in ERA5 during periods with higher CIN.

To examine the environment spatially and temprally near to an event occurence in each dataset composites were made of precipition, CAPE, and 10m wind differences between events in the different datasets. These composites were made for the RELAMPAGO main operations domain and the area imeediately to the east. ERA5 was used to supply the CAPE and 10m wind values during the events in each dataset. The composite includes 99th percentile events from 25 different gridpoints for a total of 10975 events, some of which overlap. For each of these 10975 events a square grid around each gridpoint five gridpoints in each direction is created, and these grids are averaged to produce the composite. The precip composite shown in Fig. 2.19 illustrates again that the satellite datasets have overall larger precipitation amounts. The spatial perspective surrounding the central point where the event is occuring shows that these differences are largely concentrated at the gridpoint containing the event. The differences between the reanalysis datasets MERRA2 and ERA5 and the satellite datasets TRMM 3B42 and IMERG drops off rapidly with distance from the central point, with MERRA2 and to a lesser extent ERA5 differences showing that at the edges of the composited area these datasets actually have more precipitation than the satellite datasets. This indicates that the event causing storms in the satellite datasets cover a smaller spatial footprint than those in the reanalysis datasets. CAPE differences are presented in Fig. 2.20. MERRA2 events are seen to be associated with less obvious frontal boundaries, as indicated by the north to south gradient of CAPE differences during MERRA2 events. Relative to other datasets, MERRA2 has lower CAPE equatorward, and higher CAPE poleward, with the exception of the comparison to IMERG where MERRA2 CAPE is lower everywhere but with a notable north to south gradient. In contrast, ERA5 CAPE shows the opposite struction in the CAPE differences, with ERA5 CAPE larger to the north and lower to the south than in other datasets, thus indicating stronger frontal structures during ERA5 events. The satellite datasets illustrate a middle ground between the stronger frontal structures in ERA5 and weaker in MERRA2, with IMERG events occuring in higher CAPE environments than TRMM. The 10m wind differences plotted in both the figures

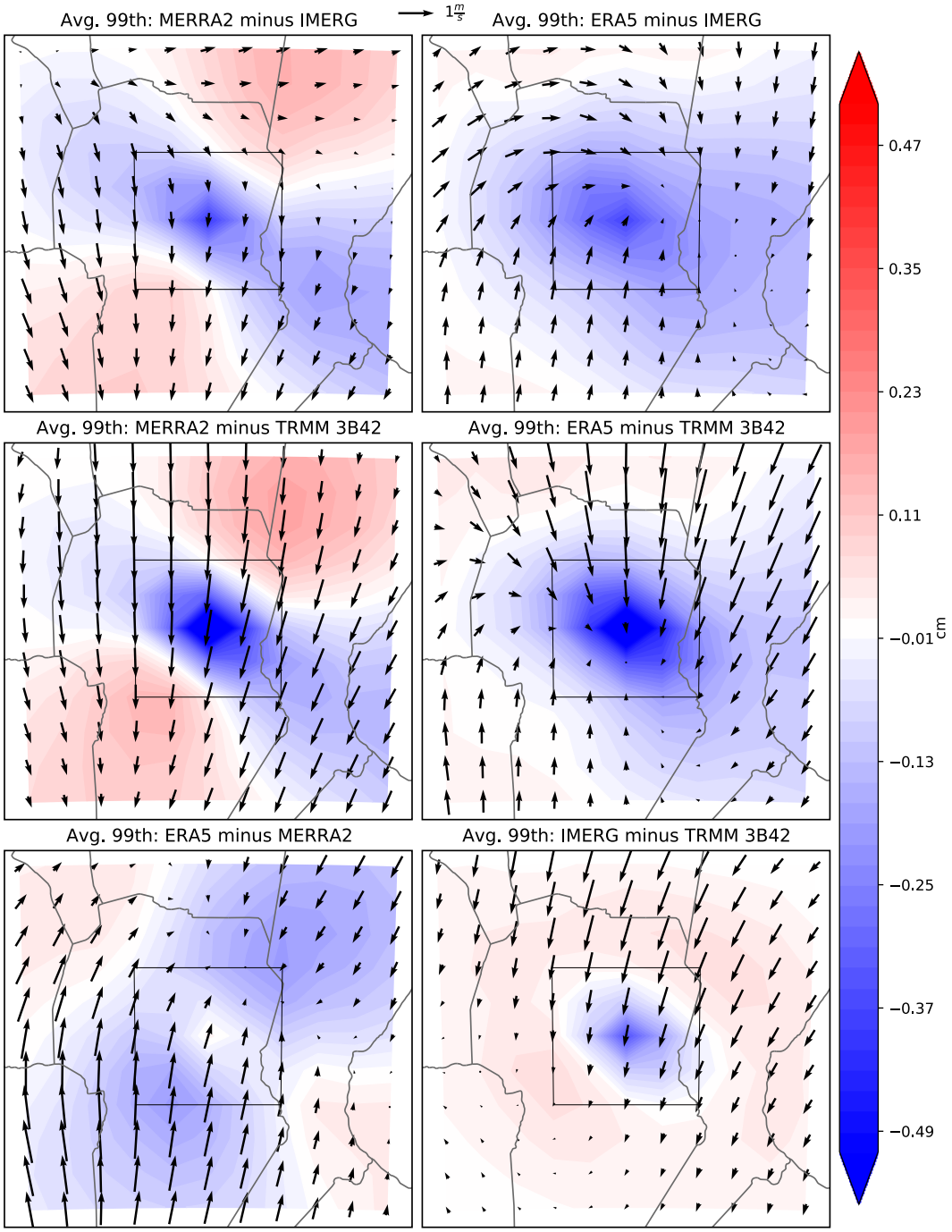

Figure 2.19: Composites of precipitation differences in cm between events in the four datasets. The square on the map represents the area of the gridpoints used for generating the composite. Vectors represent the vector difference of the 10m wind.

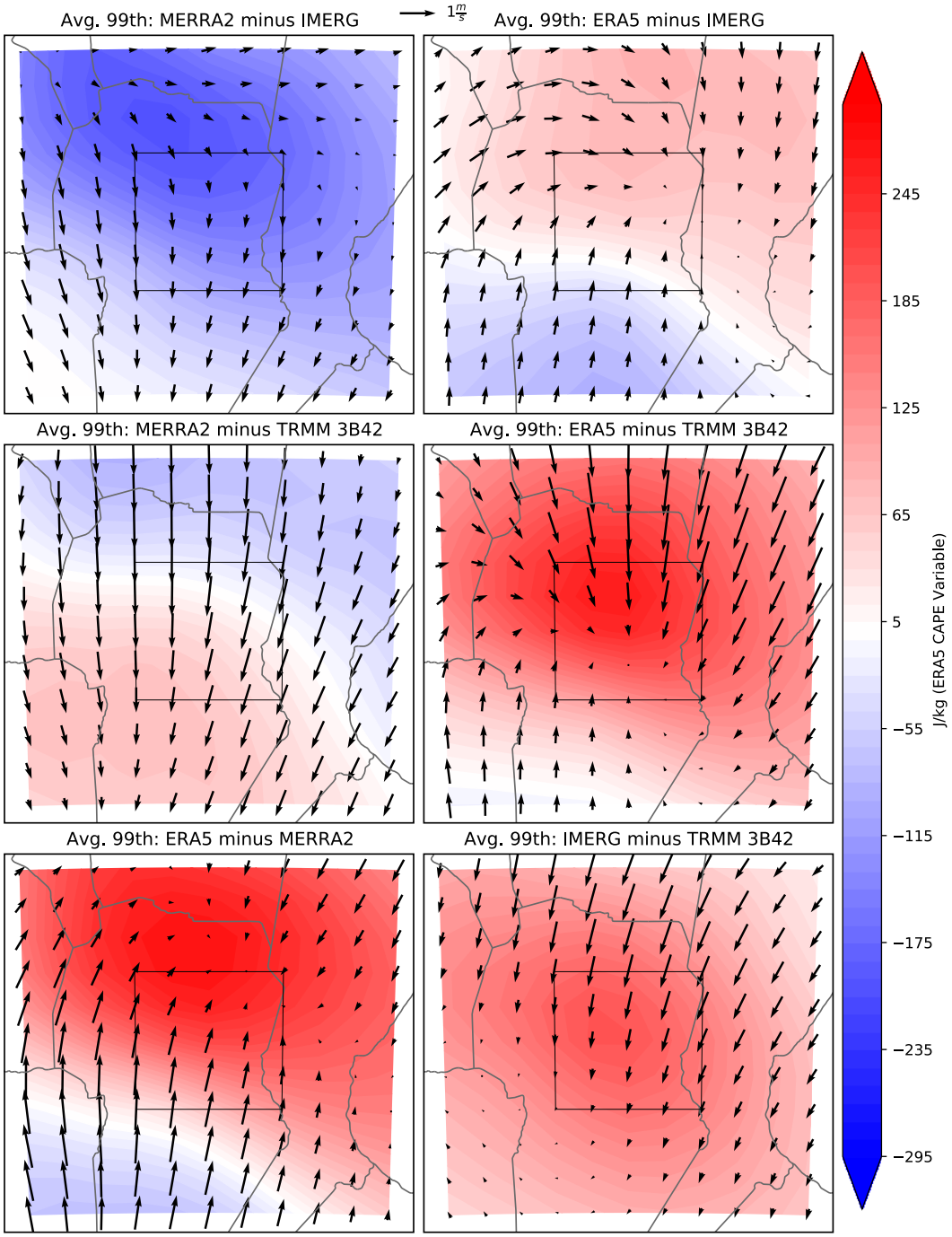

Figure 2.20: As in Fig. 2.19 but for CAPE.

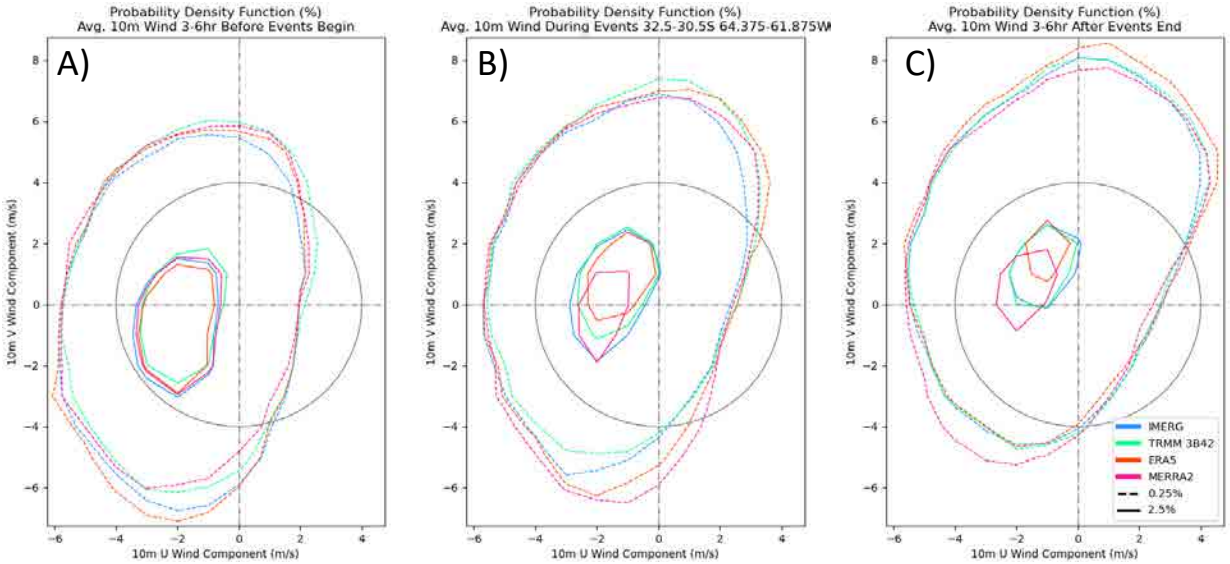

Figure 2.21: Probability density functions of average 10m U and V wind A) 3-6 hours before an event begins B) During Event C) 3-6 hours after an event ends. Circle plotted is a magnitude of 4 m/s and 0 lines are provided for reference. The 2.5% probability contour is solid and the 0.25% contour is dashed.

show that ERA5 events occur in situations with a stronger circulation around a surface low than in the other datasets, which is expected given the observed stronger CAPE gradients. The southerly wind anomalies shown in the MERRA2 comparisons also coroborate that the frontal structures in MERRA2 events are weaker, at least in this particular area. Fig. 2.21 shows the distribution of the 10m U and V wind during events at the central point of the composites presented in Fig. 2.19 and Fig. 2.20. Over the 15 hours between 6 hours before a 3 hour event begins and 6 hours after an event ends the general wind shift between east-northeast to southeast during a frontal passage is apparent. This change is most apparent in ERA5 and least apparent in MERRA2, indicating that of all the datasets MERRA2 has the least events associated with a strong cold frontal passage and ERA5 has the most, with the satellite datasets falling in between.

Fig. 2.24 provides an example of a situation identified as an extreme rain event in the TRMM and IMERG datasets but not the MERRA2 or ERA5 datasets that occurred in a high CAPE environment equatorward of a cold front. Along the cold front, all datasets except MERRA2 show a 2.5cm rainfall contour in the nine hour accumulation field, although in different places. Ahead of the cold front along the 200m terrain contour both IMERG and TRMM show a separate maxima

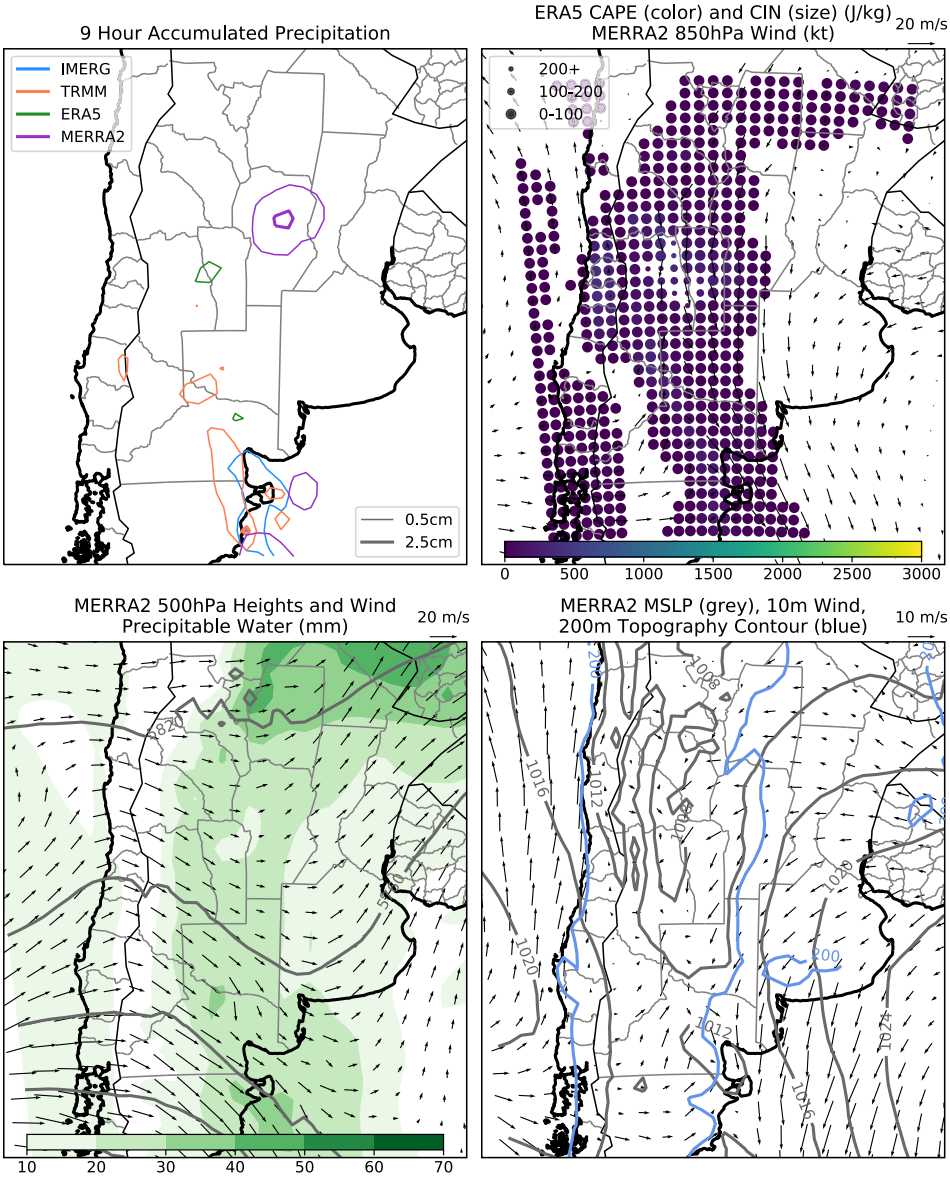

Figure 2.22: Environmental conditions associated with an event ending at 0730 UTC 10 November 2005. Panel A shows the nine hour accumulation in each dataset for the period 0130 UTC - 1030 UTC 10 November 2005. Panel B illustrates CAPE and CIN from the ERA5 dataset at 0630 UTC 10 November 2005, with the color of the dot indicating CAPE in J/kg according to the colorbar at bottom and CIN in J/kg according to the legend in upper left. Also depicted is the 850hPa winds from MERRA2 at 0600 UTC 10 November 2005. Panel C depicts 500hPa height and wind as well as PWAT from MERRA2, and panel D depicts MERRA2 MSLP, 10m wind, and 200m terrain contour, at 0600 UTC 10 November 2005.

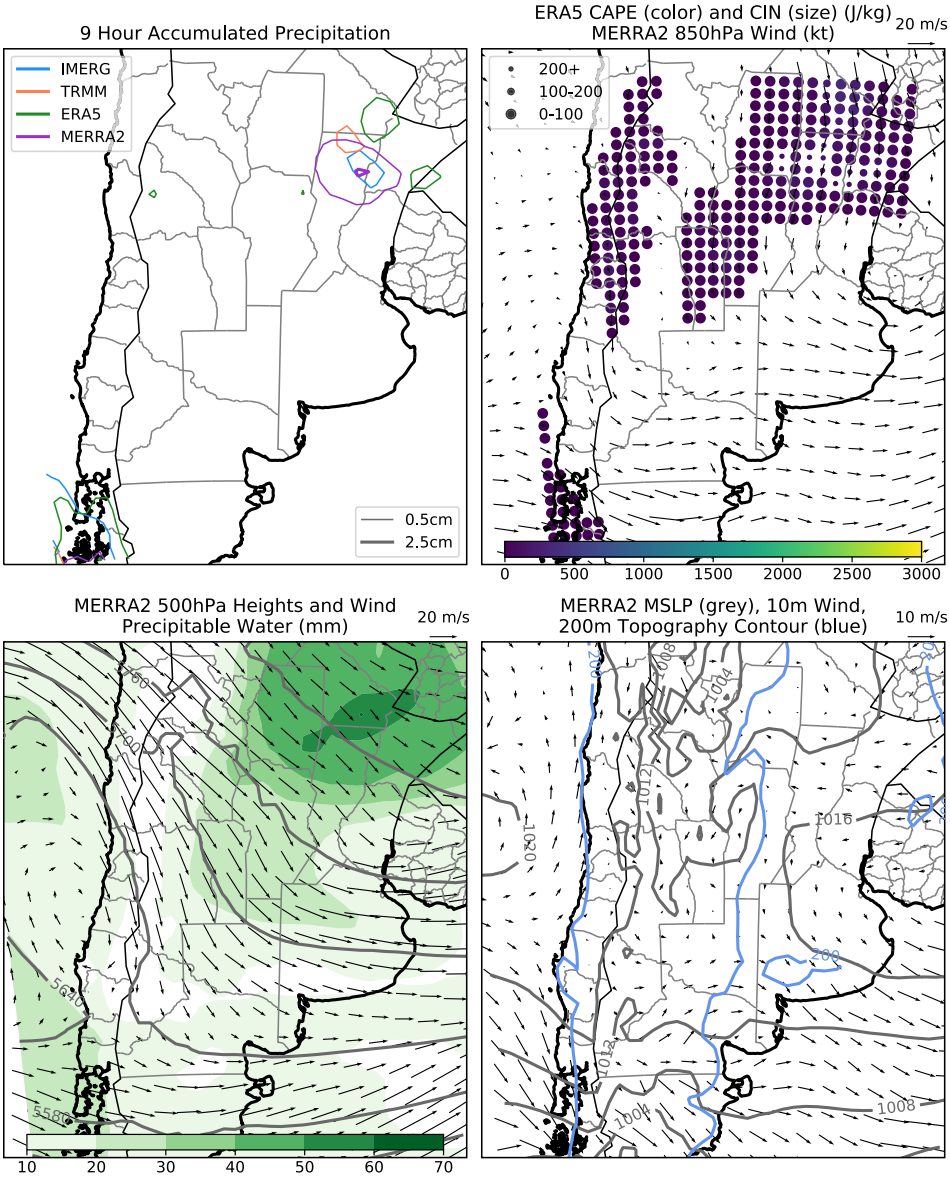

Figure 2.23: As in Fig. 2.22 but for an event ending at 0730 UTC 24 May 2011, with nine hour accumulations for the period 0130 UTC 24 May 2011 - 1030 UTC 24 May 2011, and instantaneous CAPE and CIN variables at 0630 UTC 24 May 2011 and other variables from 0600 UTC 24 May 2011.

of precipitation that is not present in ERA5 or MERRA2. This precipitation occurs in an area with high CAPE (>2500 J/kg) and absolute values of CIN >80 J/kg, illustrating an event that contributes to the difference in CIN between ERA5 and IMERG/TRMM at these gridpoints. As seen in Fig. 2.24 a potential mechanism for convective initiation despite the moderately high CIN values could be upslope flow as seen by the wind vectors at 850hPa and 10m relative to the 200m elevation contour. Fig. 2.17 also shows a number of gridpoints away from terrain where ERA5 events are shown to have significantly lower CIN than TRMM and IMERG. Fig. 2.25 shows an event where this is the case. All four precipitation datasets display a 2.5cm contour, but the area of the 2.5cm contour in ERA5 (green) is much smaller than the others, and is also co-located with the area of lowest CIN, suggesting that convective rainfall outside of this area was suppressed by the magnitude of the CIN values in the area where the other three datasets produced large areas of rainfall. Taken together, these two cases provide examples of processes that result in ERA events occurring in lower CIN environments across the entire domain east of the Andes mountains.

Examination of cases with substantial discrepancies between the preciptation datasets revealed four primary meterological situations: 1) MERRA2 event in a marginal thermodynamic environment; 2) MERRA2 event with a strong approaching trough; 3) TRMM/IMERG event in a high-CAPE environment, and 4) ERA5 events with comparitively low CIN. Fig. 2.22 illustrates a MERRA2 case in a marginal environment. Total precipitation over the 9 hour period resulted in a 2.5cm MERRA2 contour in north central Córdoba province (center of plot) with no other dataset producing more than 0.5cm of rain in the vicinity during this 9 hour period. CAPE and CIN are both low in the region, and CAPE is zero on the eastern half of Córdoba Province, while 850hPa flow is generally northerly due to a high pressure system to the southeast. 500-hPa heights and wind show a small shortwave approaching the region with anticyclonically curved flow over the location of heaviest rainfall. As at 850hPa ,MSLP and surface wind again indicate the high pressure to the southeast, as well as a lee trough. The surface and 850hPa flow are both upslope into Córdoba Province, as indicated by winds with an easterly component intersecting the 200m terrain contour on the surface plot. This case provides an example for how MERRA2 can produce a 99.9th

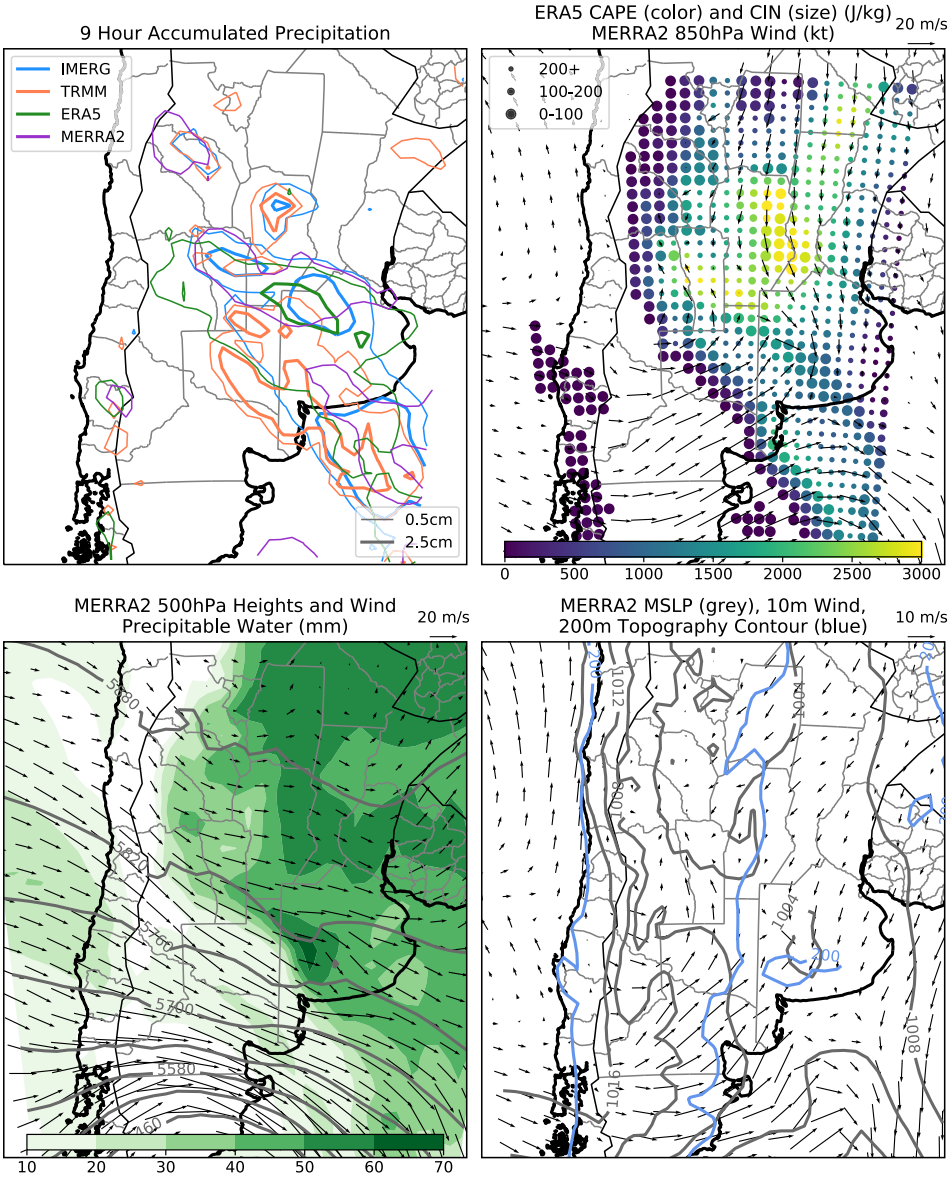

Figure 2.24: As in Fig. 2.22 but for a TRMM event ending at 0430 UTC 24 December 2009, with nine hour accumulations for the period 2230 UTC 23 December 2009 - 0730 UTC 24 December 2009, and instantaneous CAPE and CIN variables at 0330 UTC 24 December 2009 and other variables from 0300 UTC 24 December 2009.

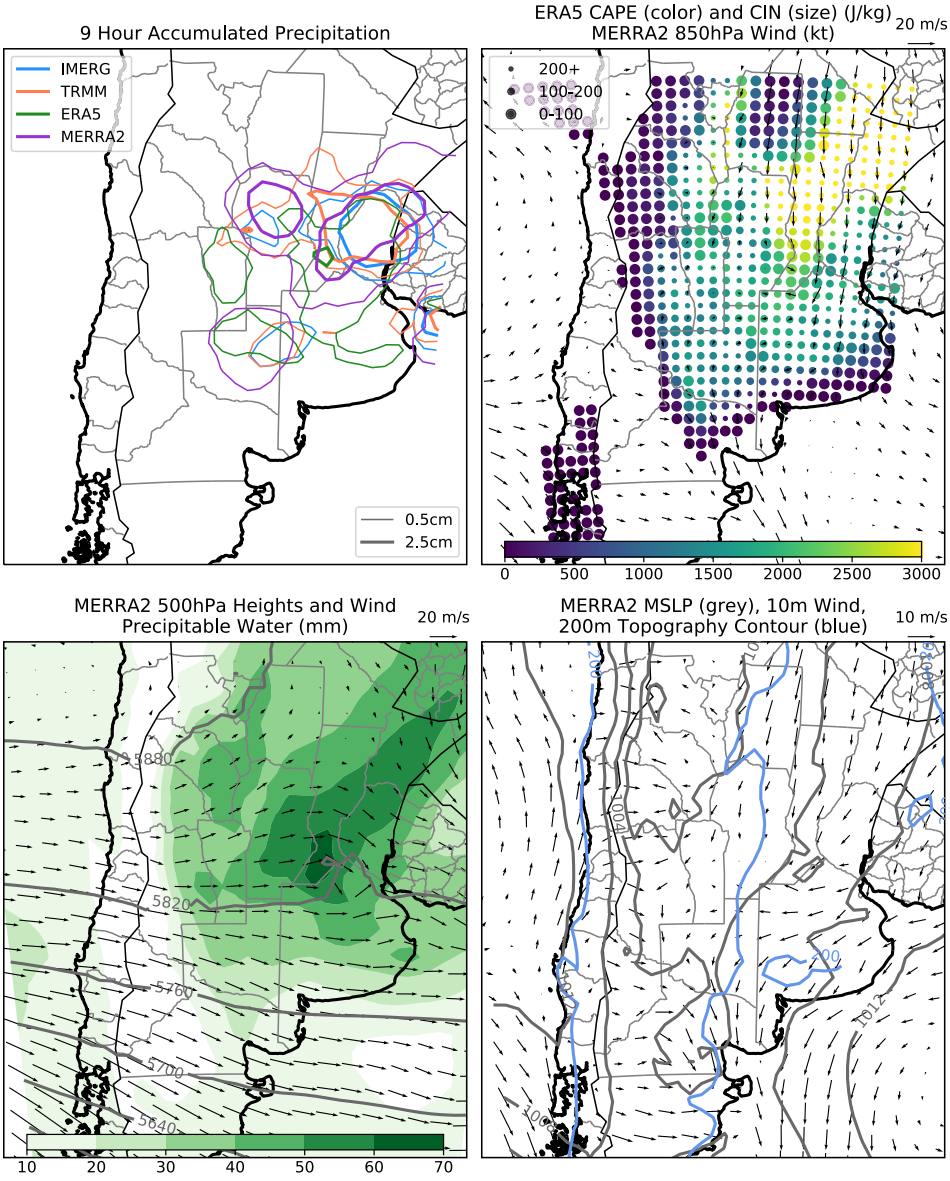

Figure 2.25: As in Fig. 2.22 but for an event ending at 1630 UTC 8 February 2001, with nine hour accumulations for the period 1030 UTC 8 February 2001 - 1930 UTC 8 February 2001, and instantaneous CAPE and CIN variables at 1530 UTC 8 February 2001 and other variables from 1500 UTC 8 February 2001.

percentile three hour event in an environment with average PWAT and the absence of significant CAPE via upslope flow. Many MERRA2 events in low CAPE environments also occurred in areas where upslope flow would be an insignificant factor, often in association with a strong trough at 500hPa. Fig. 2.23 is one such example, showing a deep, nearly cut off, trough at 500hPa accompanied by a wide area of rainfall to the east of the trough in all datasets. CAPE in the area of this rainfall are less than 500 J/kg and at the surface there appears to be convergence coincident with the area of rainfall. Of all four datasets, the 2.5-cm contour encloses the largest area in MERRA2. This low-CAPE event thus provides another example of the type of event that results in MERRA2 events being associated with lower average CAPE.

2.6 Chapter 2 Conclusions

This study has found that four global precipitation datasets (ERA5, MERRA2, TRMM 3B42 and IMERG) are poorly to moderately correlated with each other over subtropical South America for three hour accumulation periods. Extreme events identified by appying a percentile threshold to these datasets found that events were generally independent between datasets, with little overlap between identified events except between TRMM and IMERG. At most areas east of the Andes mountains the percentage of events that did not overlap closely in space or time with the corresponding dataset was between 30 and 50%. When the seasonality of events in different datasets were compared, similar patterns were found in all datasets with small differences at both the 99th and 99.9th percentile. The northeast of the domain is characterized by events in the spring, the north central part of the domain by summertime events, and events on average occurred steadily later in the summer at more poleward gridpoints until the poleward extent of the convective region. IMERG, TRMM and ERA5 all showed a pattern of events ending in the late evening along the Andes mountain range, and a preference for events ending at steadily advancing times through the night moving eastward toward the Atlantic Ocean. This pattern is evident at both the 99th and 99.9th percentiles. MERRA2 showed a bimodal distribution of events at most longitudes with events preferred to end in the afternoon hours with a secondary peak in the early morning. ERA5

was found to have the lowest CIN during three hour extreme rain events, and CAPE and PWAT values during events much greater than MERRA2, slightly greater than TRMM and about equal to IMERG. MERRA2 events by contrast were associated with the lowest CAPE and PWAT. These results could indicate that MERRA2 is overproducing rain in more marginal environments while not producing enough in more thermodynamically rich environments. The difference between ERA5 and the satellite datasets could be related to events where the ERA5 convective parameterization was unable to overcome CIN that did not completely suppress convection as seen from space by the satellite datasets. These differences are crucial to understand for the researcher seeking to make conclusions about the meteorological environments associated with extreme rain after compiling a list of extreme precipitation events. QPE is a hard problem, particularly at the tail of the distribution examined in this study. These results help further understanding of the behavior of each of these four datasets at the extremes in a data sparse region to help researchers make informed decisions about dataset choice.

For the region of Argentina discussed here, it is notable that the satellite datasets contain a larger proportion of events that are smaller spatially and less obviously forced by the synoptic meteorological setup. This indicatest that the convective parameterizations of both reanalysis datasets are not able to resolve the mesoscale features that can cause the creation of very deep storms that produce large amounts of rainfall but that are smaller spatially than a frontal boundary. Such a storm was observed on 25 January 2019 in Argentina (Rocque and Rasmussen, 2022). More strongly forced storms, such as the 13-14 December 2018 event that will be discussed herin, are captured by all datasets but enough of the spatially smaller, more weakly forced events exist in the satellite datasets that the composites clearly show their presence. For MERRA2 events this may be partially a resolution problem as the native MERRA2 resolution is 0.5 x 0.625 degrees. However, ERA5 and TRMM 3B42 are produced on the same native resolution, 0.25 x 0.25 degrees, and despite this the same patterns are observed relative to the satellite datasets in ERA5 as well as MERRA2. With this higher resolution ERA5 does produce realistic precipitation patterns with precipitation falling in a northwest-southeast oriented oval similar to both satellite datasets, while

MERRA2 tends to produce largely circular precipitation patterns in the convective environments found in this region. Overall, for applications within the coverage period of IMERG the author would recommend using that dataset for precipitation studies as it captures both the more strongly and weakly forced events that occur in the domain. For applications requiring a longer period, ERA5 has an advantage over MERRA2 in that it produces a shape of precipitation events close to what is expected of the large MCSs in the region, while MERRA2 creates more circular storms and is therefore not as suitable for a case study type of analysis.

Chapter 3

Impact of Model Vertical Resolution on a RELAMPAGO Case: 13-14 December 2018

3.1 Chapter 3 Introduction

The mobile operations period of the Remote Sensing of Electrification, Lightning, and Mesoscale/Microscale Processes with Adaptive Ground Observations (RELAMPAGO) field campaign took place from 1 November 2018 to 15 December 2018 in the Córdoba and Mendoza provinces of Argentina (Nesbitt et al., 2021). This project aimed to explore the processes behind the extreme convection in this region recognized in Zipser et al. (2006), and particularly how these processes interact with the terrain in the region. Two mountain ranges have a strong influence on the weather in the region: the Andes mountains along the west coast of the continent and the SDC mountain range which runs north-south through Córdoba province. Rocque and Rasmussen (2022) found that by varying the height of these mountain ranges resulted in differences in storm evolution during two RELAMPAGO cases. Reducing the height of the Andes during a strongly synoptically forced case (the same case that will be discussed herein) resulted in a weaker MCS, while removing the SDC with the Andes at full height resulted in few differences from the control run. Anabor et al. (2009) used a composite of initial conditions for ten MCSs that occurred in the RELAMPAGO region to investigate the causes of backbuilding using the WRF model with 10km resolution, and found that initial upstream propagation was driven by gravity waves created by the storm and later by outflow from the storms lifting air from the low level jet. Piersante et al. (2021) produced synoptic composites leading up to days when the TRMM precipitation radar detected a wide convective core in the region. These composites indicate that most wide convective cores are strongly synoptically forced as was the 13-14 December case that will be analyzed here. Mesoscale convective systems (MCS) in the region are also associated with high probabilities of hail using

microvave satellite observations (Bang and Cecil, 2019; Bruick et al., 2019), and hail was observed during the 13-14 December case (Nesbitt et al., 2021). Another feature observed during this event was backbuilding, a common occurence among storms of the region (Rasmussen et al., 2014). Backbuilding occurs when an MCS expands on the upstream side of the storm (Peters and Schumacher, 2015). Analysis of backbuilding storms was a goal of the RELAMPAGO campaign, and this case provides a good example of the phenomenon. Many cases during the campaign were not well forecast more than 36 hours before the event and probability of detection of rain events greater than 10mm/day less than 50% (Nesbitt et al., 2021; Casaretto et al., 2022). Convection allowing models used for real-time forecasting during the campaign in this case did indicate storms in the area, but did not capture the full extent of the MCS or the backbuilding component of this system, even within 18 hours of the event.

To assess why backbuilding was not well forecasted by the operation models used during the campaign two model simulations are presented in this study; one a close representation of the model setup in place for the real time forecasts and the other using the same setup but with 81 vertical levels instead of the 51 in the real-time simulation. Both simulations were performed using computer resources from Computational and Laboratory (2019). Many previous studies have been performed assessing the effect of an increased vertical resolution. Chou (2011) reports that increasing the vertical resolution of the data assimilation using NAM model initial conditions improved the initial analysis of surface pressure and low level temperature due to a reduction in upper level interpolation errors. Two studies of sea breeze dynamics in complex terrain, one in southwestern India and the other southern Italy, found no sensitivity to model vertical resolution during a sea breeze simulation (Aravind et al., 2022; Avolio et al., 2017). Over the flat terrain of the ocean Hahmann et al. (2015) also found little impact of varying model vertical resolution. Aligo et al. (2009) found that increasing vertical resolution in thunderstorm cases over the Midwestern United States improved rainfall forecasts in weakly forced situations during which fine scale variations in thermodynamic variables were important but had a a larger positive bias in more strongly forced cases when the increased vertical resolution led to more saturated gridcells and thus an increase

in rainwater production by the microphysics scheme. Xia et al. (2021) found minor impacts from changing vertical resolution; a simulation with 66 vertical levels better matched observations taken during a mountain wave case in the lee of the Cascade mountain range than a control simulation using 44 vertical levels. Cannon et al. (2017) also found minor differences in winds above the mountaintop in a mountain wave case in a study of "sundowner" winds near Santa Barbara, California between simulations utilizing 41 and 61 vertical levels. However, these differences were unable to be compared to observations because they were found above the surface. Increasing resolution from 40 to 60 vertical levels was also found to make a positive impact on forecasts of barrier jet formation in the Denmark Strait (DuVivier et al., 2017). Taken together, these studies indicate that for strongly forced situations in complex terrain, increasing the number of vertical levels used in a WRF model simulation can improve forecast results. Section 2 of this paper describes the meteorological history of this event, Section 3 describes the modeling studies underdaken, and briefly discusses what wider application the results of this case study may have using a tracking algorithm to identify preferred areas of convective initiation in the region.

3.2 Overview of 13-14 December Case

The case observed by RELAMPAGO field instruments on 13-14 December provides an excellent opportunity for research into the storms of the region. A large MCS formed near the SDC and merged with a previous MCS to the east to form a system that by 0600 UTC 14 December spanned from central Córdoba province to beyond the east coast of South America as can be seen in Fig. 3.1. Fig. 3.2 illustrates the supportive environment for convection in this case. As a strong 500hPa trough approached from the west, lee cyclogenesis occurred which in turn led to a strong low level jet. This jet carried moisture rich air from the Amazon south to the RELAMPAGO study region, with over 50mm of precipitable water located over northeastern Córdoba province, and high amounts of CAPE coupled with low CIN in the same region. Aiding in lift was a shortwave at 500hPa that can be seen in Fig. 3.2 as a turning of the 500hPa wind vectors over northern Córdoba province. At 1200 UTC 13 December (the initialization time of the model experiments)

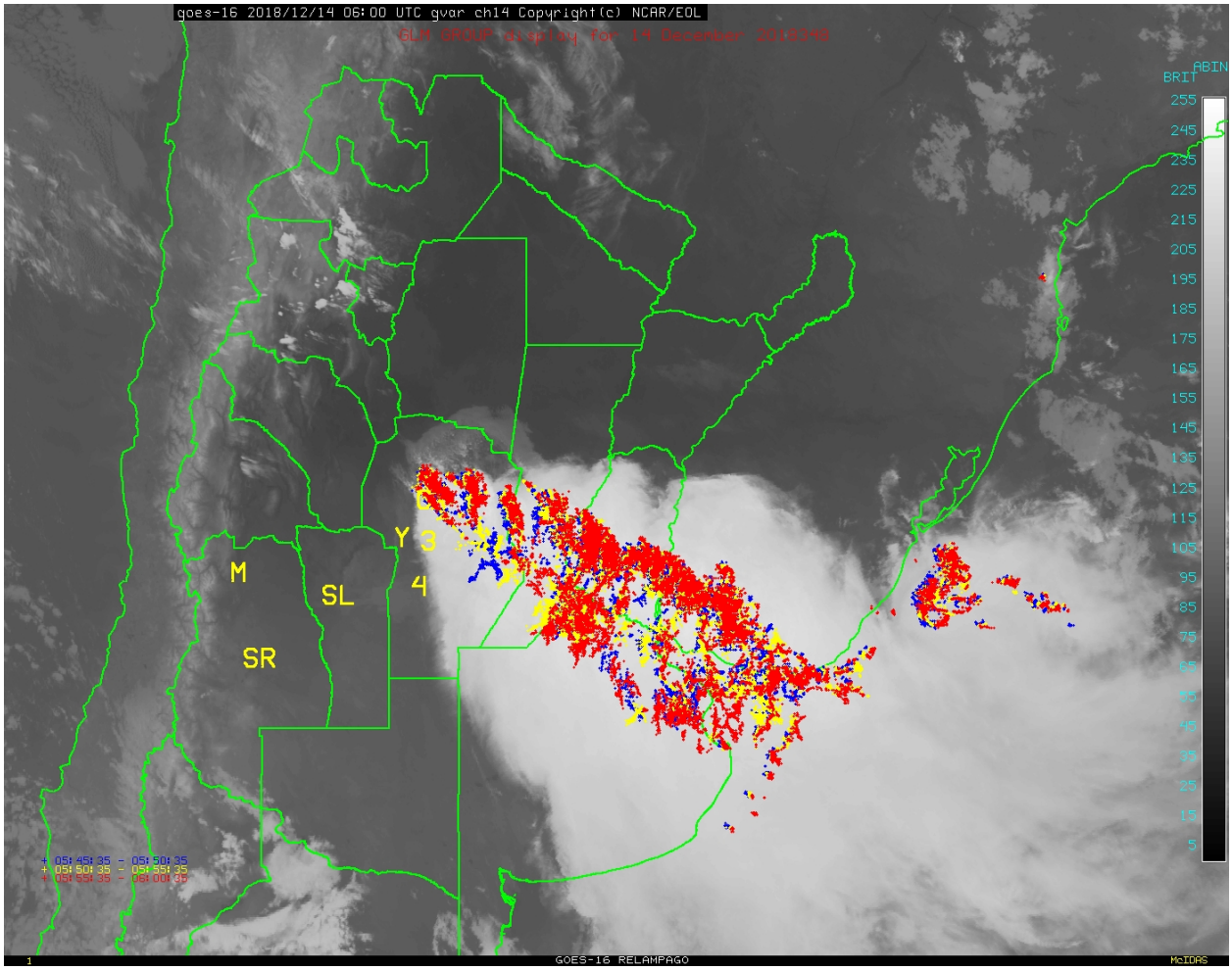

Figure 3.1: Infrared satellite image at 0600 UTC 14 December from the RELAMPAGO field catalog maintained by the Earth Observation Laboratory showing the MCS with recent lightning data from the Global Lightning Mapper overlaid. Red indicates strikes within the last 5 minutes, yellow strikes 5-10 minutes old and blue strikes 10-15 minutes old

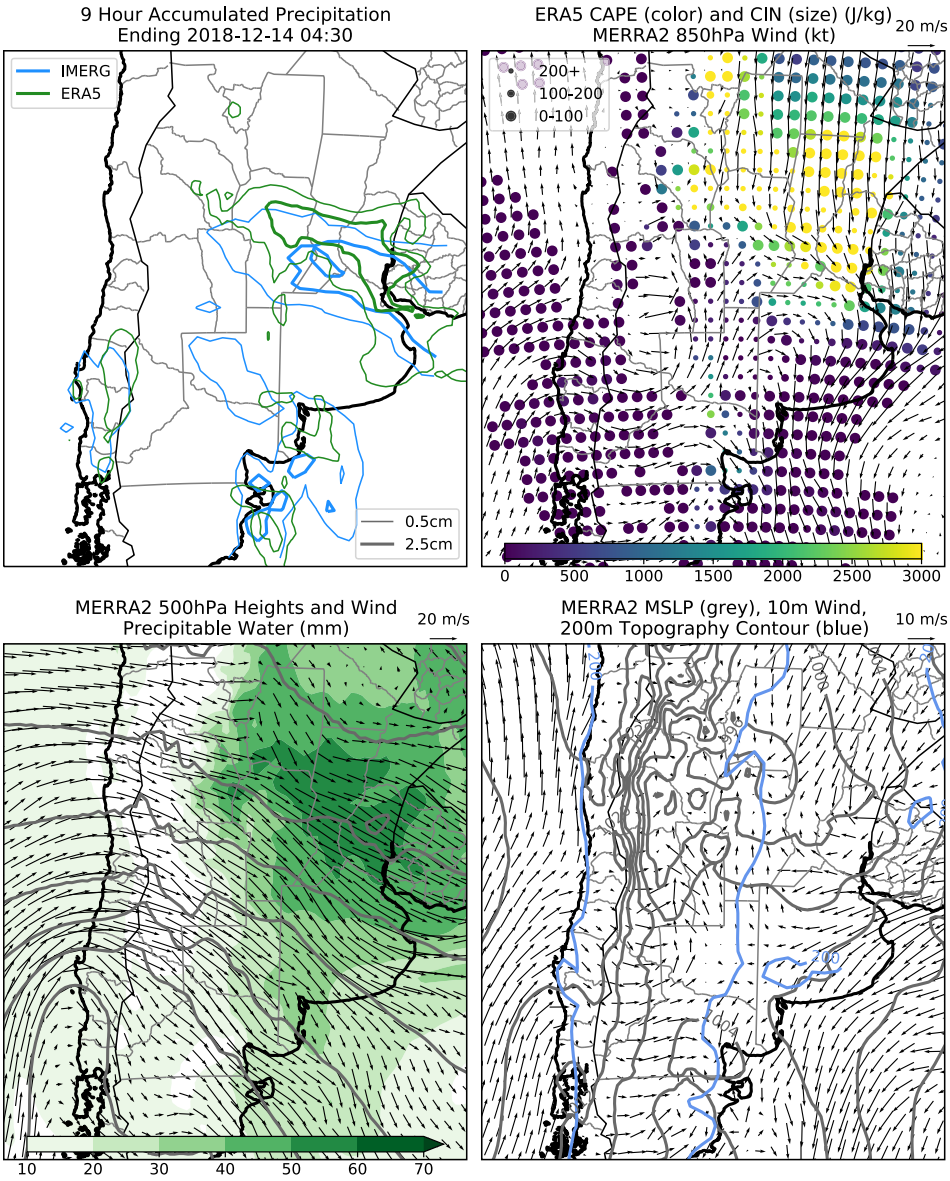

Figure 3.2: As in Fig. 2.22 but for an event ending at 0430 UTC 14 December 2018, with nine hour accumulations for the period 2230 UTC 13 December 2018 - 0730 UTC 14 December 2018, and instantaneous CAPE and CIN variables at 0330 UTC 14 December 2001 and other variables from 0300 UTC 14 December 2018.

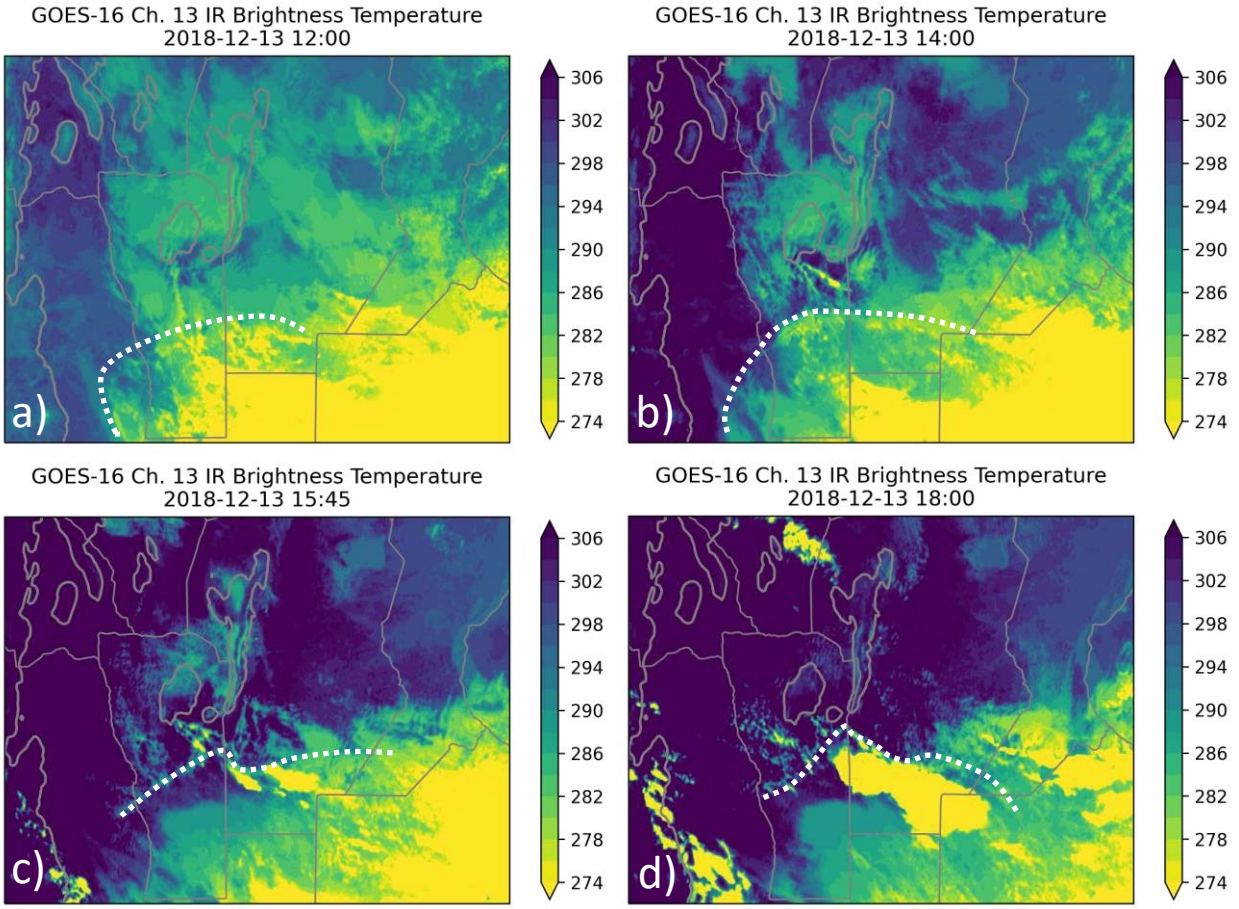

Figure 3.3: Top of atmosphere brightness temperatures from the GOES-16 channel 13, the clean IR window, at (clockwise from top left) 1200 UTC , 1400 UTC,1800 UTC and 1545 UTC 13 December. The location of the outflow boundary discussed in the text is noted with a dotted white line, and 1000m elevation si contoured with a thick grey line, while province borders are outlined with a thin grey line.

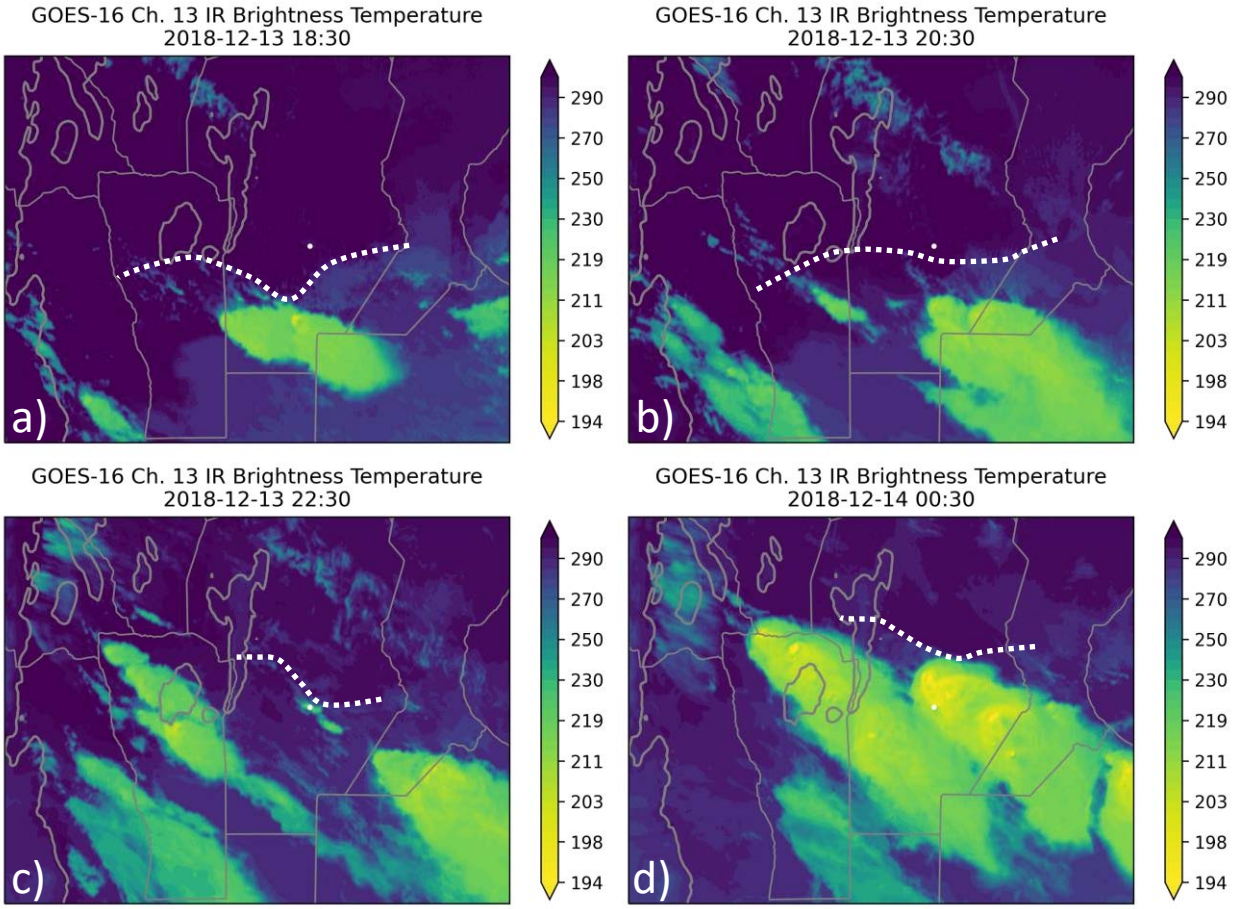

Figure 3.4: As in Fig. 3.3 but with a new colorbar to highlight storm detail. Times depicted are (clockwise from top left) 1830 UTC 13 December, 2030 UTC 13 December, 0030 UTC 14 December, and 2230 UTC 13 December. The white dot denotes the location of the sounding presented in Fig. 3.7.

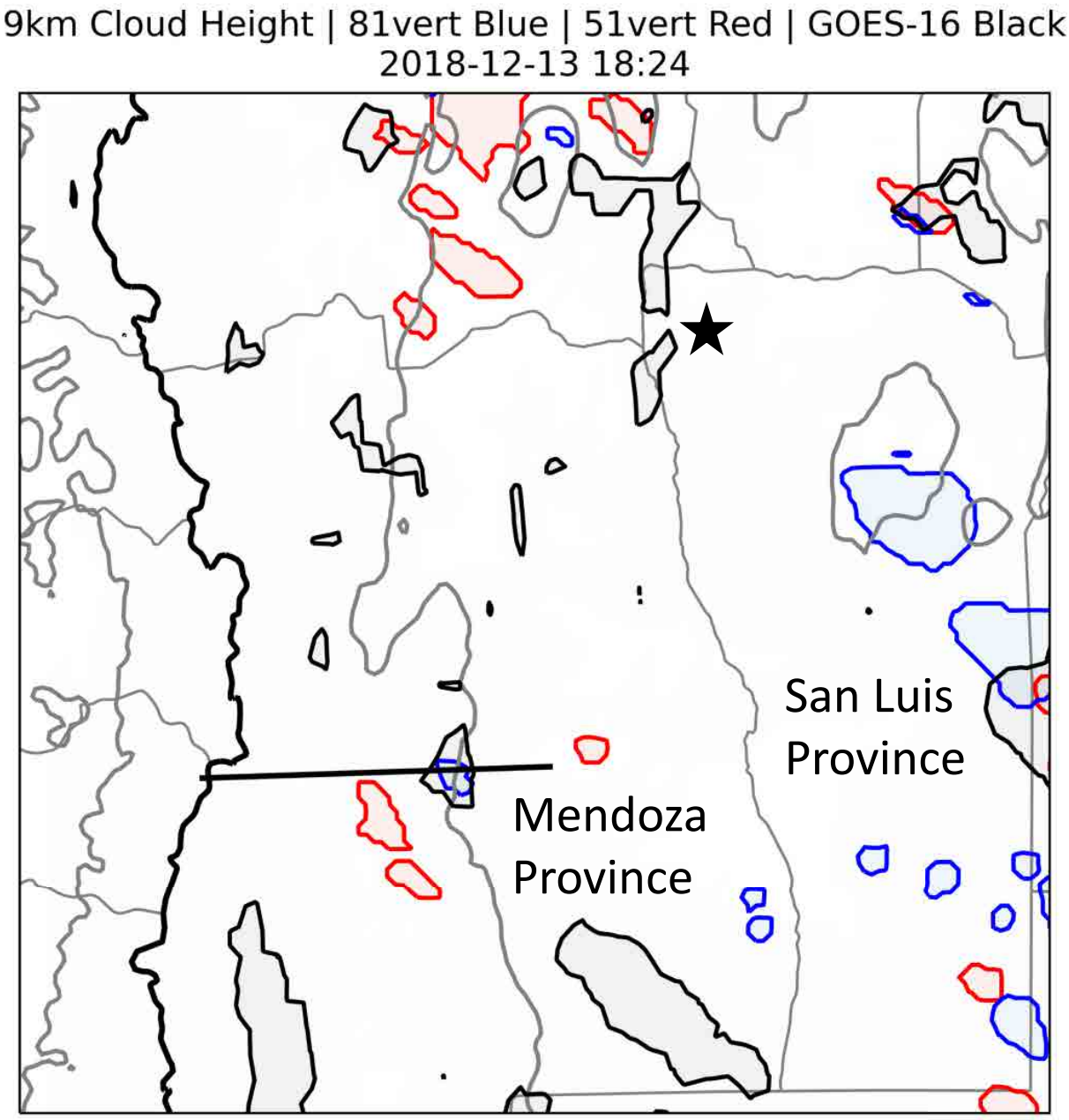

Figure 3.5: Map of 9km cloud top heights at 1824 UTC 13 December from the GOES-16 geostationary satellite (black), 81vert model simulation (blue) and 51vert model simulation (red). Mendoza and San Luis provinces are labeled for reference, and the star marks the location of convective initiation at 2130 UTC 13 December. The black line across western Mendoza procinvce is the line along which the cross section shown in Fig. 3.6 is taken.

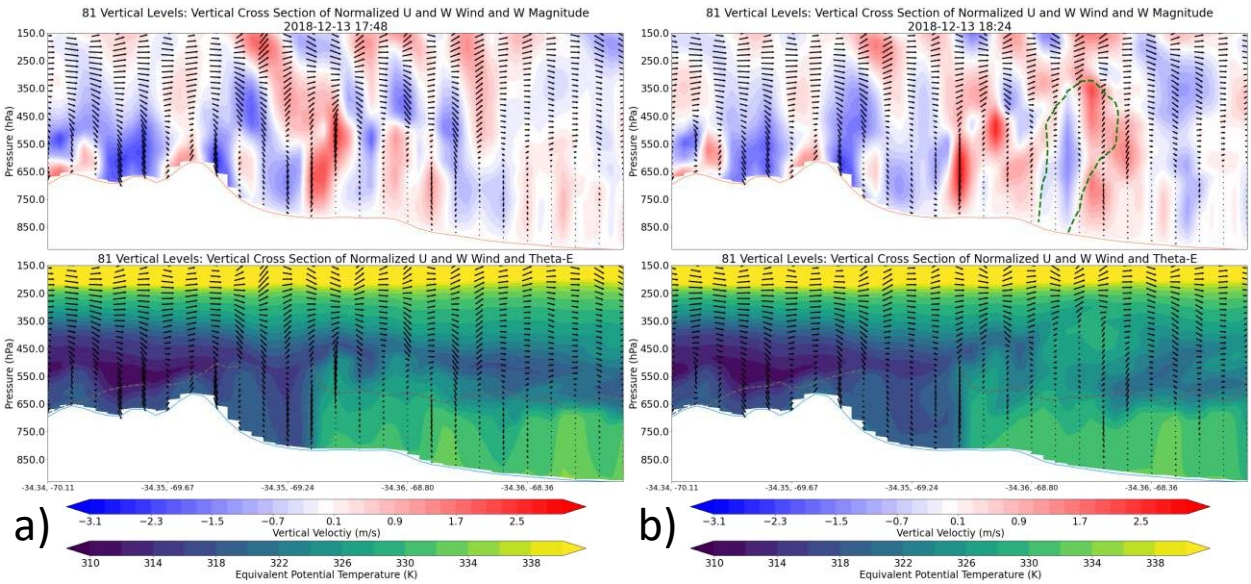

Figure 3.6: Cross sections of vertical velocity and θ_e at 1748 UTC and 1824 UTC 13 December from the 81vert model simulation. Green dashed line on the vertical velocity plots is the modeled 20dbz reflectivity contour, and the grey dashed line on the θ_e plots is the LFC of a surface based parcel. Wind vectors in both plots are normalized by the maximum component magnitude of u and w in the 51vert simulation in order to highlight vertical motions.

an MCS was ongoing to the southeast of Córdoba province that had formed from convection that initiated in and near southern Córdoba province and grown upscale. This convection left behind an outflow boundary in its wake. This boundary, combined with convergence from the flow of the low level jet around the SDC mountain range, led to two supercells initiating in southern Córdoba province at 1700 UTC 13 December. Fig. 3.3 shows this sequence. At 1200 UTC 13 December the outflow boundary is expanding to the north and west from the MCS visible in the southeast quadrant of the map domain, and no convection has formed along it. At 1400 UTC 13 December a small storm is just beginning to form ahead of the outflow boundary just to the south of the 1000m elevation contour. By 1545 UTC this storm is dissipating just to the south of the outflow boundary along with another brief storm that formed at 1515 UTC. The supercells initiate between 1600 and 1700 UTC and at 1800 UTC they are mature. Fig. 3.4 shows the progression of the storms from 1830 UTC 13 December to 0030 UTC 14 December. At 1830 UTC 13 December convection is visible in the southwest quadrant of the map domain, just downstream of the Andes. This convection was initiated with the aid of mountain induced gravity waves, a process described

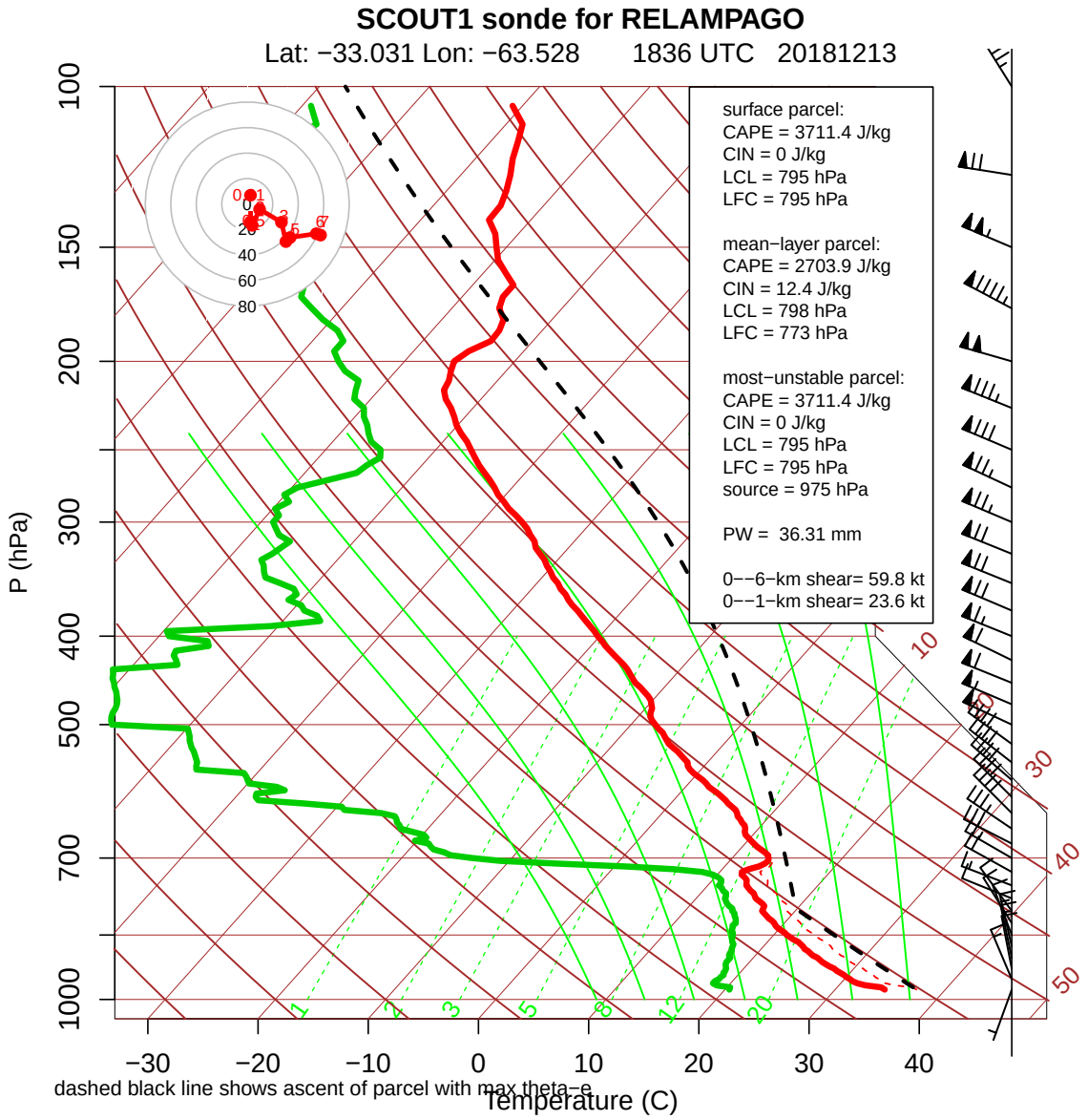

Figure 3.7: Skew-T taken near the region of rapid initiation of a line of storms at 2215 UTC 13 December. Thermodynamics strongly supportive of strong storms were observed, with a most-unstable CAPE of 3711 J/kg and a mean-layer CAPE of 2703 J/kg

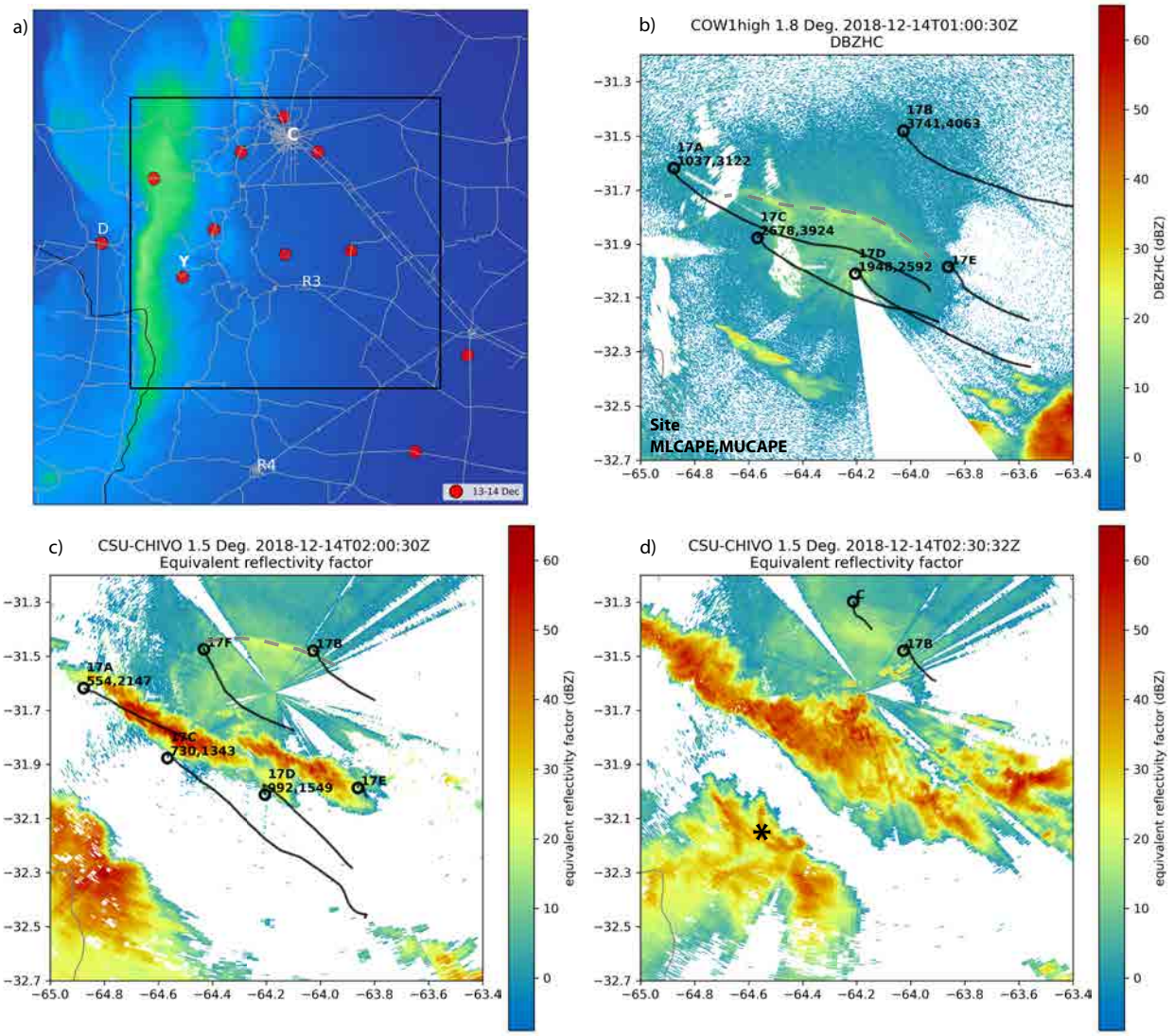

Figure 3.8: Reproduction of Fig. 18 from Schumacher et al. (2021) showing a) terrain elevation, road network, cities, and location of all soundings lauched during the 13-14 December 2018 case with red dots; b) reflectivity from the COW radar at 0100 UTC 14 December c) CSU-CHIVO radar reflectivty at 0200 UTC 14 December; and d) CSU-CHIVO radar reflectivity at 0230 UTC 14 December. Black circles and lines in each panel show the location and track of soundings launched near the time of the radar reflectivity, and at each launch location the MLCAPE and MUCAPE are listed if the sounding reached at least 500hPa. Asterisk in d) shows location of an 8cm hail report at about the time of the radar reflectivity. Note the border of Córdoba and San Luis provinces in the lower left of each panel for reference to other figures, and the black box in panel a) shows the domain for each of the other three panels. 17B in each panel is the location of the sounding presented in Fig. 3.9, The outflow boundary is noted in panels b) and c) with a grey dashed line.

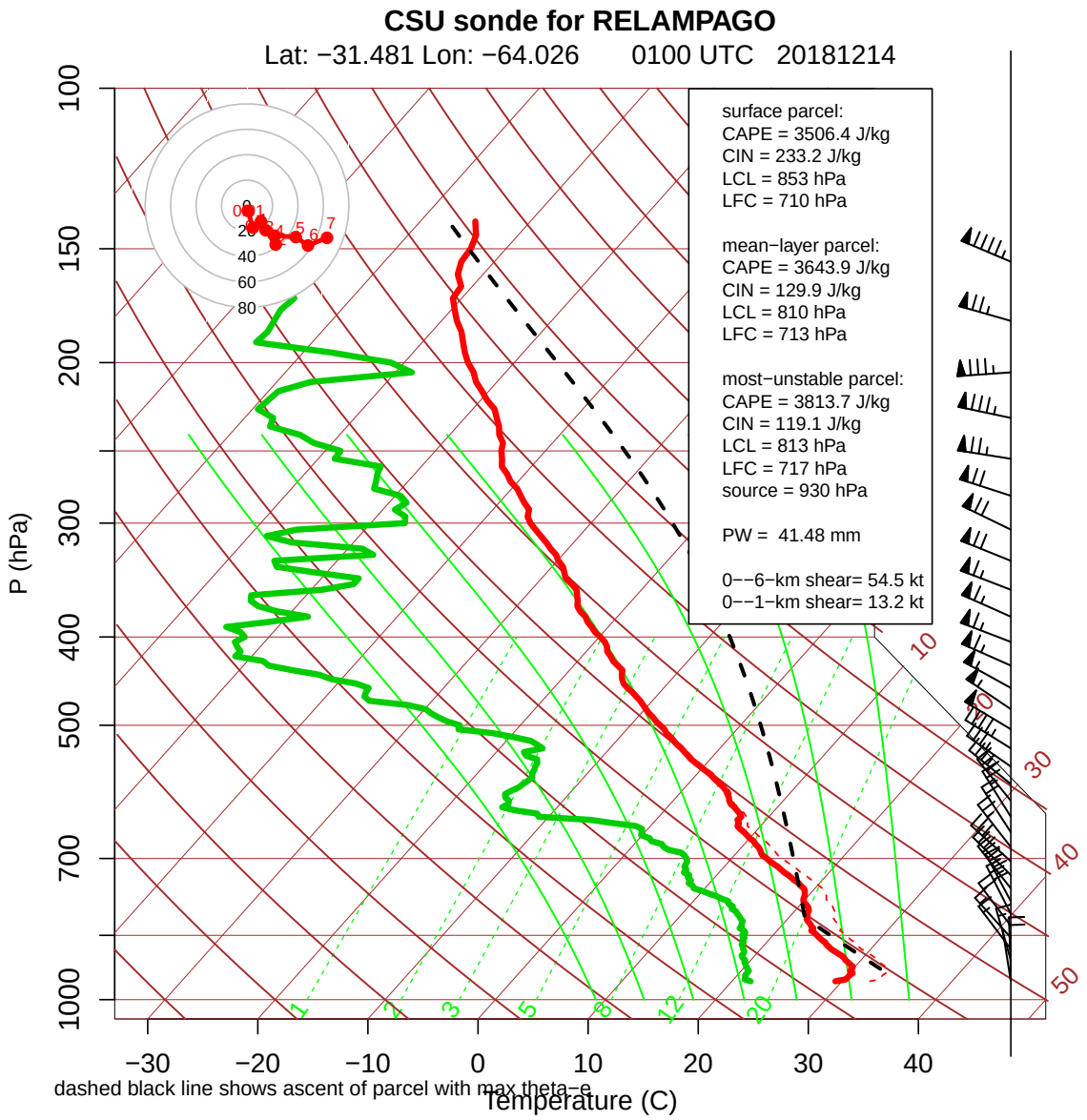

Figure 3.9: Skew-T taken near the region of rapid initiation of a line of storms at 2215 UTC 13 December. Thermodynamics strongly supportive of strong storms were observed, with a most-unstable CAPE of 3711 J/kg and a mean-layer CAPE of 2703 J/kg

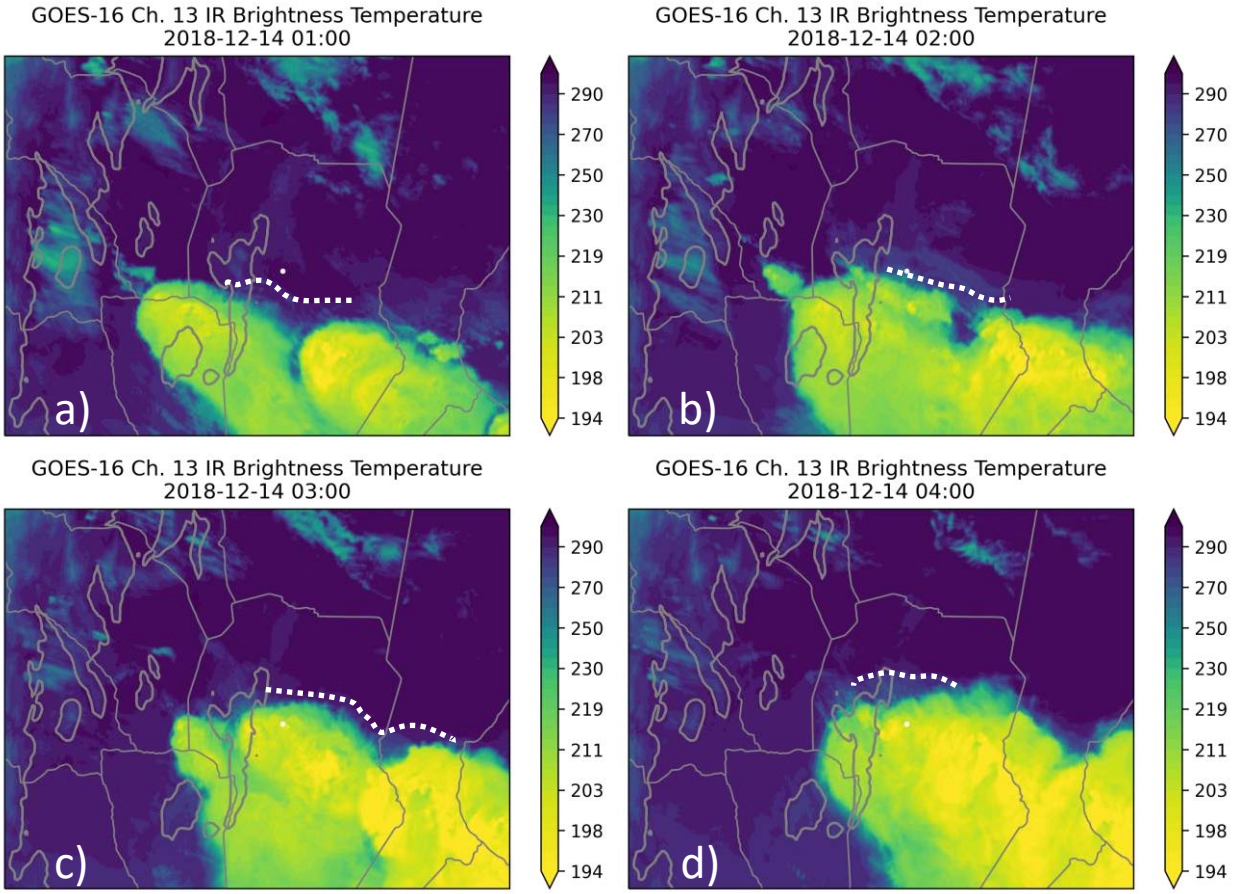

Figure 3.10: As in Fig. 3.4 but at times (clockwise from top left) 0100 UTC 14 December, 0200 UTC 14 December, 0400 UTC 14 December, and 0300 UTC 14 December, and the white dot denotes the location of the sounding presented in Fig. 3.9.

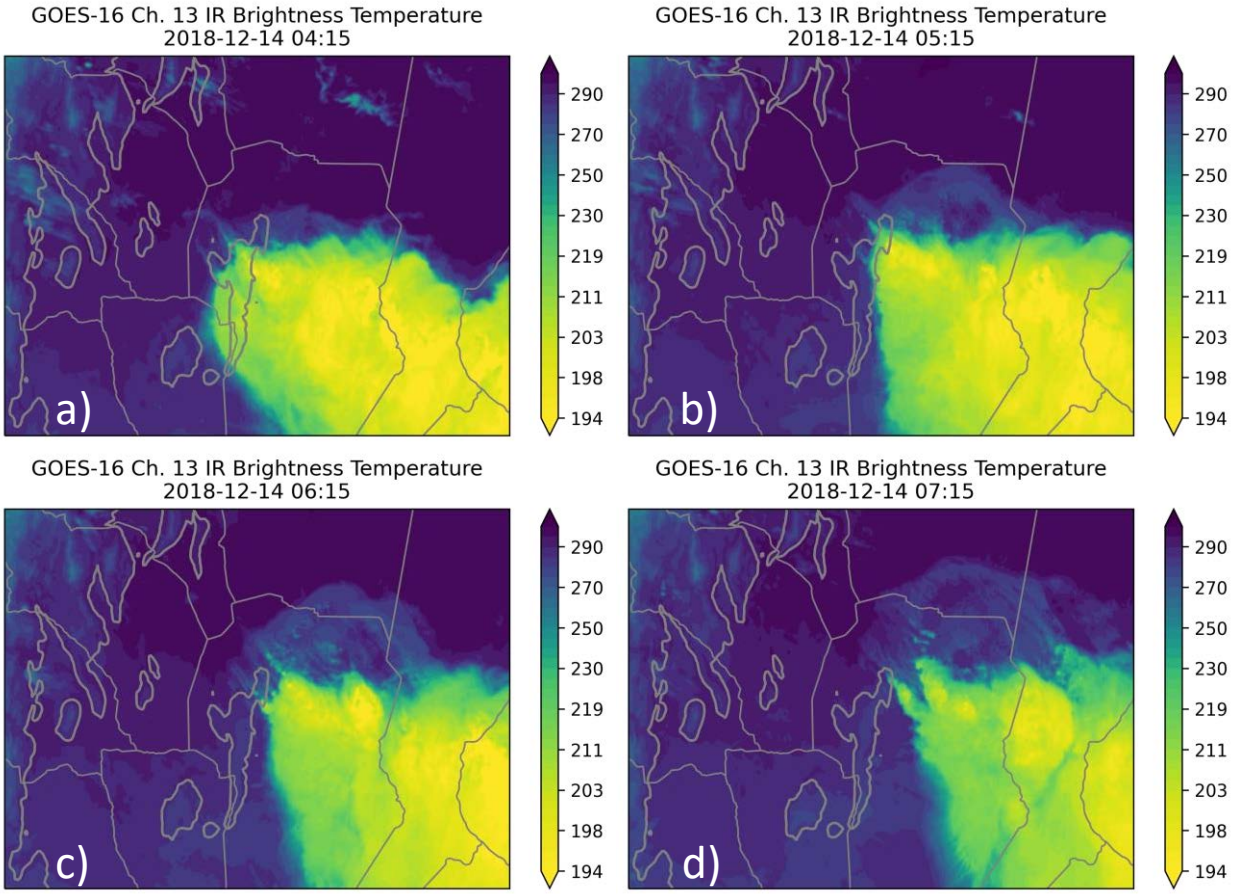

Figure 3.11: As in Fig. 3.4 but at times (clockwise from top left) 0415 UTC 14 December, 0515 UTC 14 December, 0615 UTC 14 December, and 0715 UTC 14 December.

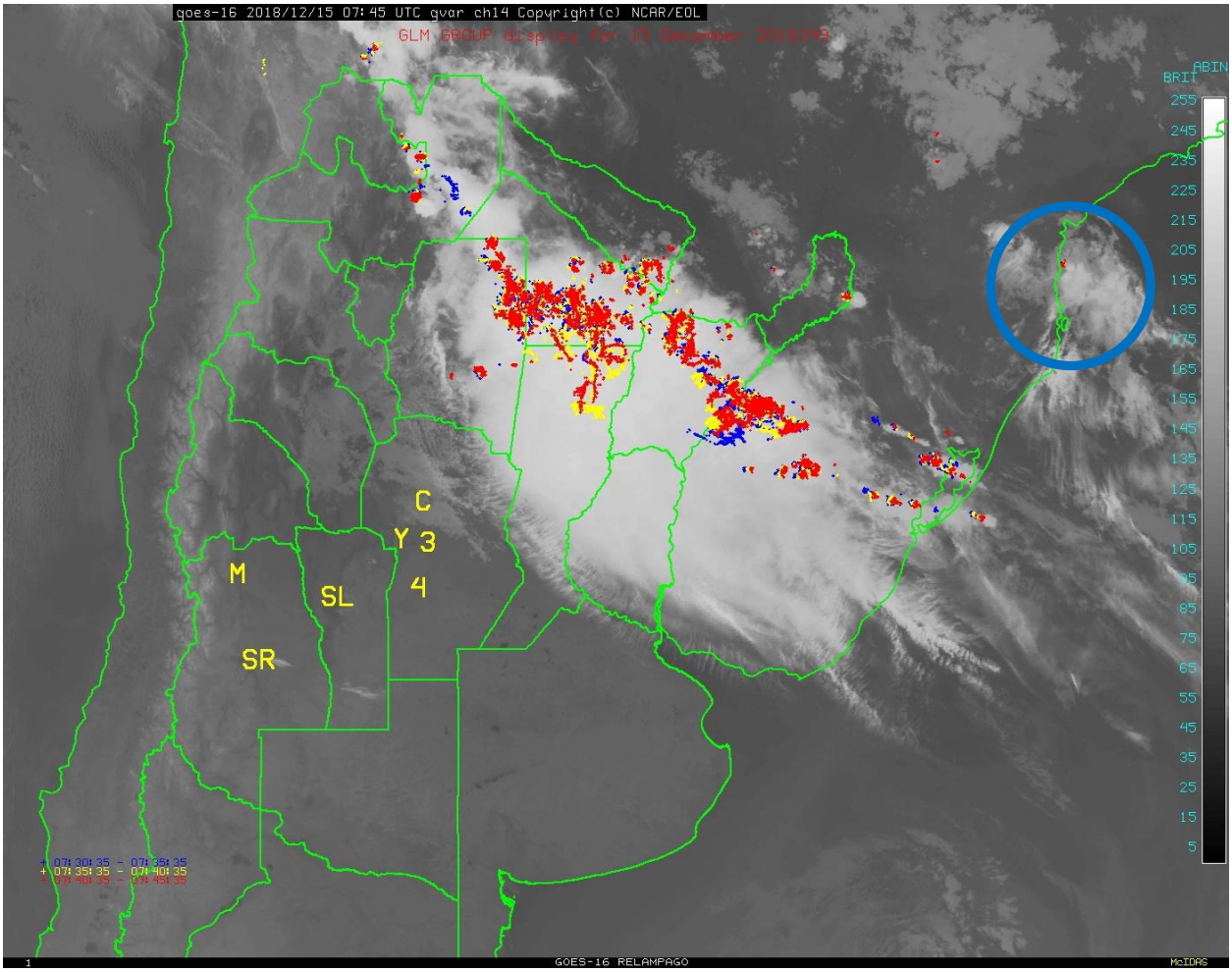

Figure 3.12: As in Fig. 3.1 but for 0745 UTC 15 December. Blue circle denotes remnants of the 13-14 December event MCS.

in the region by de la Torre et al. (2011) as having a role in the initiation of severe hailstorms in the Mendoza region. Fig. 3.5 shows the situation at 1748 UTC 13 December, comparing the 9km cloud height contour produced by model simulations to be discussed in the next section with data from GOES-16. The simulation with 81 vertical levels produced a developing storm in exactly the same place (blue contour within black contour along the 1000m terrain line bisecting Mendoza Province) as occurred in the real event. This convection formed south-southwest of the initiation location of the storms that began at 2130 UTC 13 December, noted on the figure with a star and visible at 2230 UTC in Fig. 3.4. The black line east-west line through Mendoza Province shows the location of the cross section presented in Fig. 3.6 which shows vertical velocity and equivalent potential temperature (θ_e) at 1748 and 1824 UTC 13 December. At 1748 UTC, there are two locations between 68.8W and 69.2W where higher θ_e air is being lofted above the boundary layer, and well above the level of free convection (LFC) for a surface parcel. These locations are colocated with the upward branch of rotors occurring in conjunction with lee waves induced by the Andes. At 1824 UTC, the further east of these locations has begun producing precipitation, as evidenced by the 20dbz reflectivity contour. This storm would go on to grow upscale, but eventually be starved of moisture when the storms initiated at 2130 UTC grew upscale upstream. While this wave aided initiation was occurring, the outflow from the supercell storms reinforced the existing ouflow boundary from the overnight MCS, seen at 1830 UTC and 2030 UTC 13 December in Fig. 3.4. At 2130 UTC 13 December convection was initiated in northwest San Luis province, just to the southwest of Corodba province along the outflow boundary. This convection soon merged with the storms that had formed in the northwest corner of San Luis province to form an MCS spanning from northwest to south east across the souther end of the SDC at 0030 UTC 14 December. At the same time (2230 UTC 13 December and 0030 UTC 14 December) to the east of the SDC, the northward moving outflow boundary caused the remarkably rapid initiation and growth of a line of convection through Córdoba province. This convection occurred in a strongly supportive thermodynamic environment as can be seen in Fig. 3.7, showing a relatively small capping inversion combined with large CAPE. The location of this sounding is noted in Fig. 3.4 with a white dot

on all panels, and at 2230 UTC convection can be seen developing at exactly the same point this sounding was launched three hours prior. This line of convection then merged with the convection that had previously initiated on the west side of the SDC as it moved over the mountain range. A second instance of rapid convective development occurred just to the north of this merged complex between 0130 UTC and 0200 UTC 14 December. Fig. 3.8 reproduces Fig. 18 from Schumacher et al. (2021), showing this rapid growth along the outflow boundary. At 0100 UTC 14 December the outflow boundary is visible, with convection just beginning to initiate to the southwest of the radar site. By 0200 UTC 14 December this convection has grown into a line with maximum reflectivities > 50dBz. Fig. 3.9 (from location 17B in Fig. 3.8 shows the environment that this rapid growth occurred in. A nocturnal boundary layer was just beginning to form, (local time is UTC-03:00) and above this was an extremely rich environment for convective development, with the most-unstable parcel calculated to have a CAPE of 3813 J/kg. As this line formed it starved the convection downstream of it of moisture and became the dominent feature on the western side of the storm complex. Fig. 3.10 shows this process from the satellite perspective. At 0100 UTC 14 December the outflow boundary continues to move northward towards the Fig. 3.9 sounding location (noted with a white dot) and at 0200 UTC the cold cloud tops associated with the development depicted in Fig. 3.8 are apparent. At 0300 UTC and 0400 UTC the warming of the cloud tops (indicating weakening updrafts) to the southwest of these new coldest cloud tops can be seen as the new line intercepts the moisture inflow. Between 0415 UTC and 0715 UTC the western tip of the complex continuously generated new updrafts to the west, shown in Fig. 3.11. Throughout this four hour period, cold cloud tops remained along the eastern edge of the Sierras de Córdoba as the storm complex as a whole moved to the northeast, making it an excellent example of backbuilding storm behavior. The final remnants of the storm ceased producing lightning strikes as recorded by GLM at 0745 UTC 15 December at a location to the southwest of Sao Paulo, Brazil, shown in Fig. 3.12. The storm lasted for about 38 hours from the initiation of the supercells in southern Córdoba to the final demise of the remmnants, and covered nearly 2000km. This makes the storm an excellent candidate for an in depth study of the important processes behind it and the reasons

that the real-time convective allowing models used during the campaign did not fully capture the intensity and scope of this event over the Córdoba region.

3.3 Results of Modeling Experiment

3.3.1 The Model Experiments

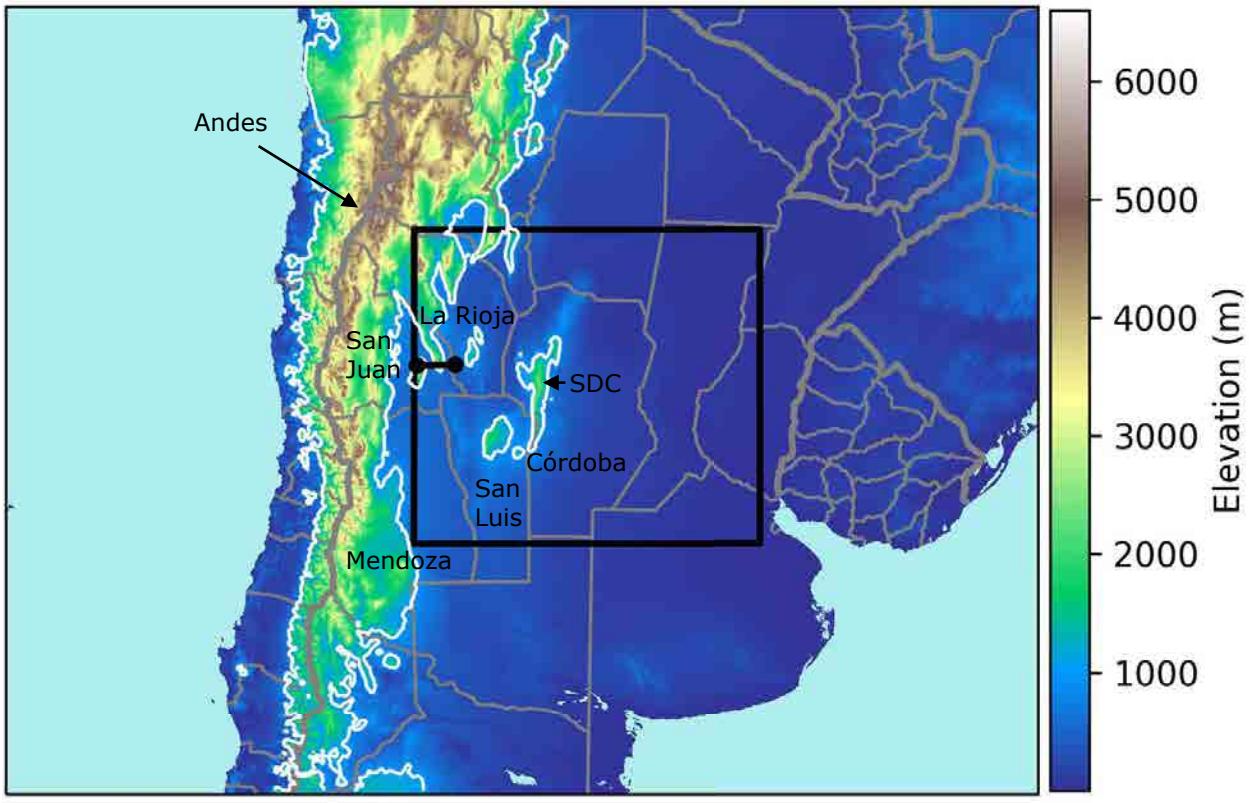

Figure 3.13: Map of 4km outer domain (edge of map represents edge of domain) and 1.33km inner domain (noted with black square) for the model experiments. Provinces are outlined with thin grey lines, and those mentioned in the text are labeled, as are the SDC and Andes mountain ranges. The thin white line represents the 1000m elevation contour, used for reference in subsequent figures. The line connecting the black dots on the west side of the inner domain near the Andes represents the cross section used to examine model level differences in Fig. 3.14.

Two model simulations were conducted as part of this study using the Weather Research and Forecasting (WRF) model. The first simulation (51vert) is intended to replicate as nearly as possible the real-time model run by Colorado State University that supported forecasting during the

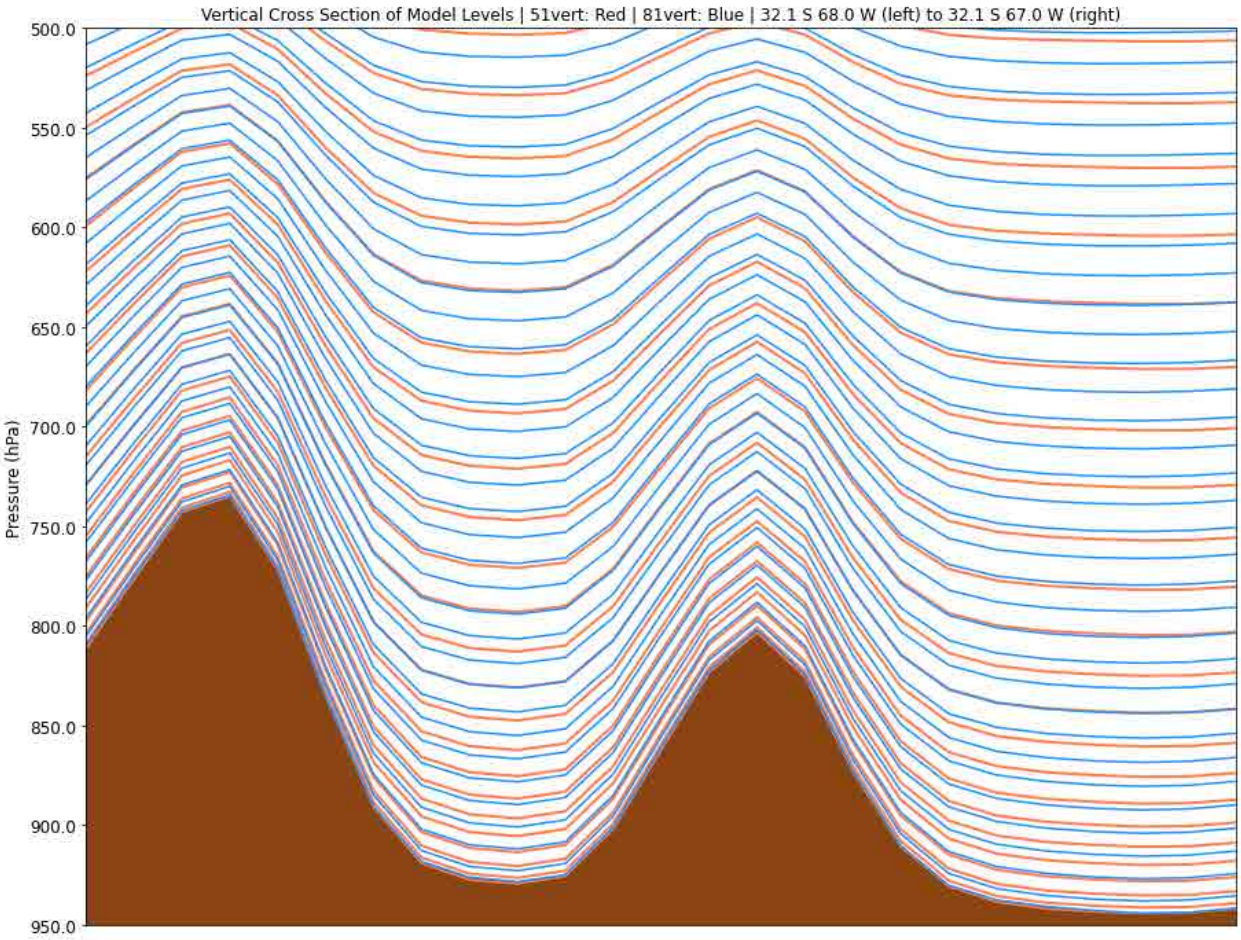

Figure 3.14: Cross section illustrating the difference between 51 (red) and 81 (blue) vertical levels over one of the many steep mountain valleys within the simulation domain, noted with the black line between black dots in Fig. 3.13. Brown represents underground areas.

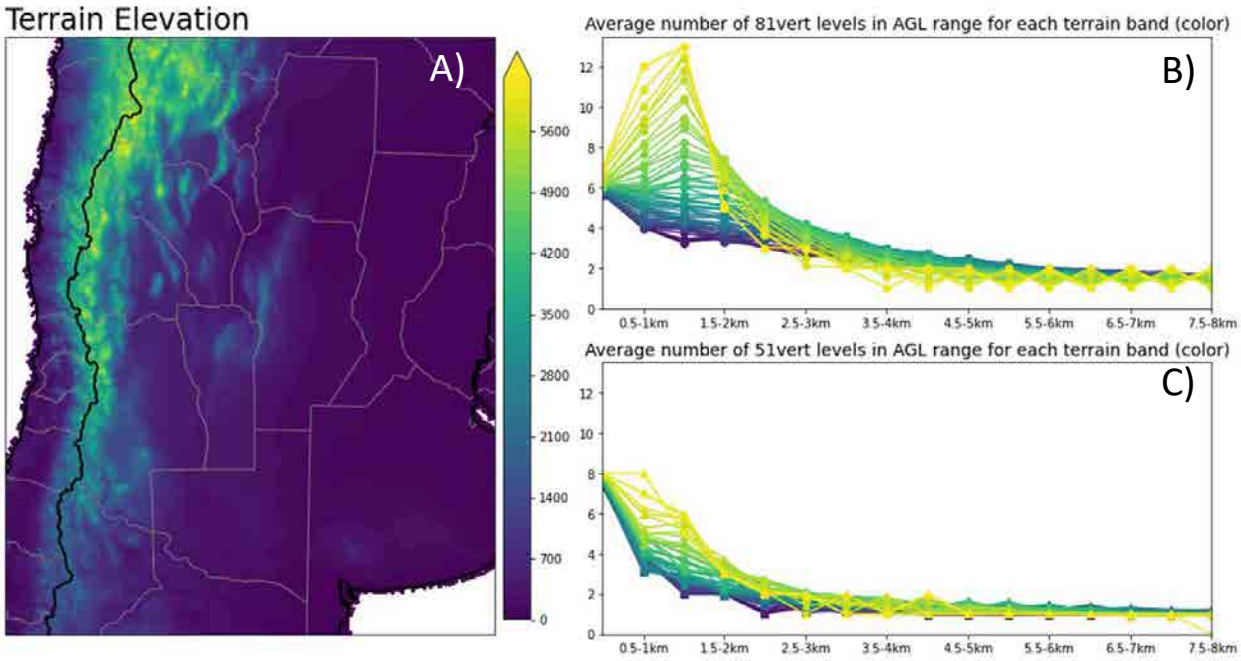

Figure 3.15: A) Map of the terrain of the study region B) Number of model levels in each band of height above ground level along the x-axis for the 81vert simulation. Color of the line corresponds to the color of the terrain in A), higher terrain causes more model levels to be at lower heights above ground level because of the shorter distance between high terrain and the top of the atmosphere. C) As in B), for the 51vert simulation.

field campaign, which did not produce a backbuilding storm. See Casaretto et al. (2022) for a detailed discussion of the performance of the real-time models used for forecasting throughout the campaign in forecasting precipitation. The second simulation (81vert) did produce a backbuilding storm, with the only difference between this simulation and the first being the addition of 30 vertical levels to the model, increasing from 51 to 81. Fig. 3.13 shows the outer (4km grid spacing) and inner domain (1.33km) for these simulations. Use of the inner nested domain that was tested but did not show significant differences from the outer domain only simulations for either model setup. Fig. 3.14 shows the model levels for the 51vert and 81vert runs over a steep mountain valley. Due to the extra model levels, the 81vert simulation model levels are able to more closely follow the terrain, enabling more model levels within the mountain valleys and more closely spaced at the mountain top level. Fig. 3.15 shows this for the whole domain, illustrating how over higher terrain the 81vert simulation has about double the number of model levels in the 1-1.5km above ground level height band compared to the 51vert simulation for a given terrain height above sea level. The simulations use Morrison two-moment microphysics and the Mellor-Yamada-Janjic boundary layer scheme. Initial conditions came from the Global Forecast System (GFS) analysis, and boundary conditions came from the GFS forecast since the goal of the 51vert run is to imitate the run of the model performed during the campaign. A model top of 50hPa was used; a 5hPa model top was tested and found to make minimal differences to either simulation. A 2km single domain run covering the same area as the 4km domain was also performed and found to have minimal differences from the 51vert simulation. The simulations are initialized at 1200 UTC 13 December, about 5 hours before the initiation of the first convection in the study region.

3.3.2 Comparison of Model Results

A mesoscale sector from the GOES-East satellite was available for this case, and the cloud height product produced from this imagery was compared to the two model simulations. Fig. 3.16 compares the area of cloud tops reaching 12km or greater between the two simulations and satellite imagery. At 1848 UTC 13 December, the supercell storms in southern Córdoba province are

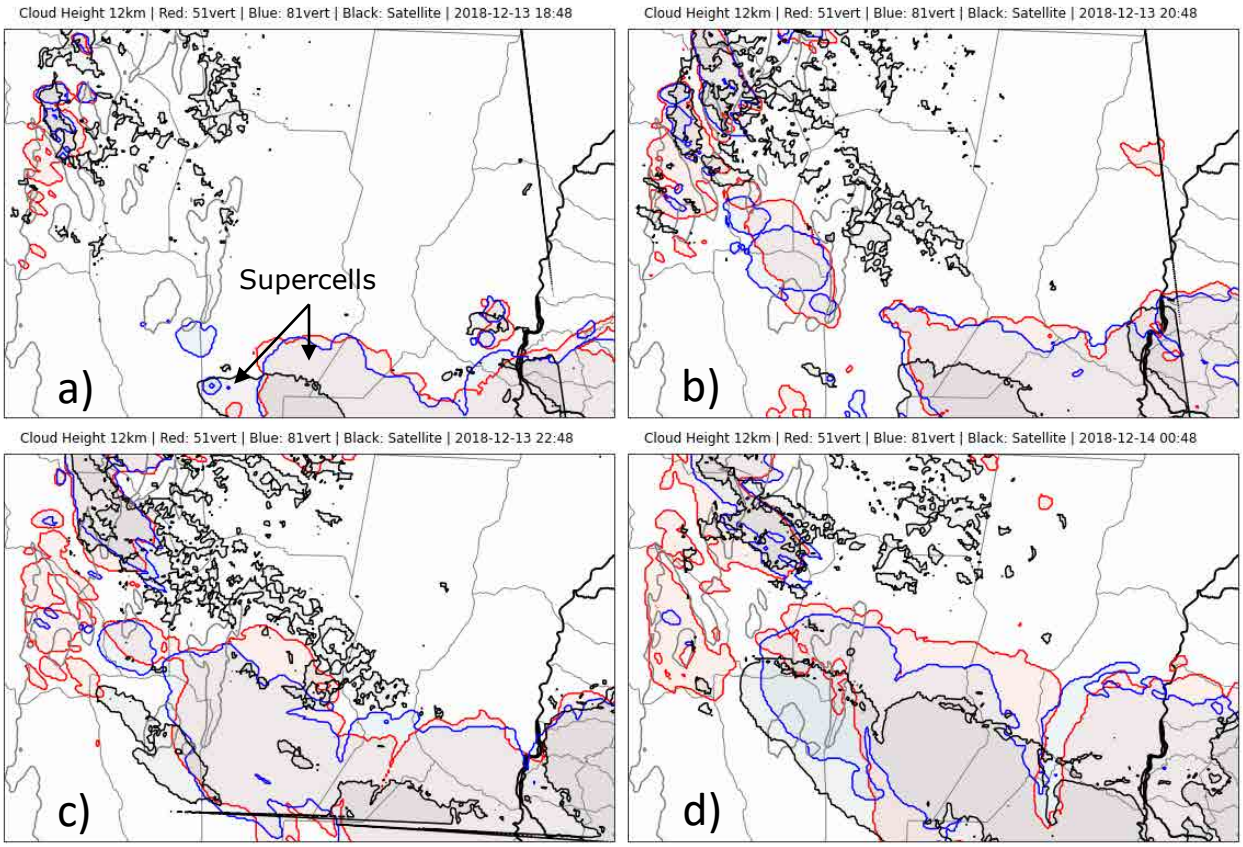

Figure 3.16: Comparison of area with cloud height greater than 12km between GOES-16 mesoscale sector (black), 51vert simulation (red) and 81vert simulation (blue) every two hours starting at 1848 UTC 13 December. Black lines in panels a), b) and c) are artifacts that occur near the edge of the GOES-16 mesoscale domain.

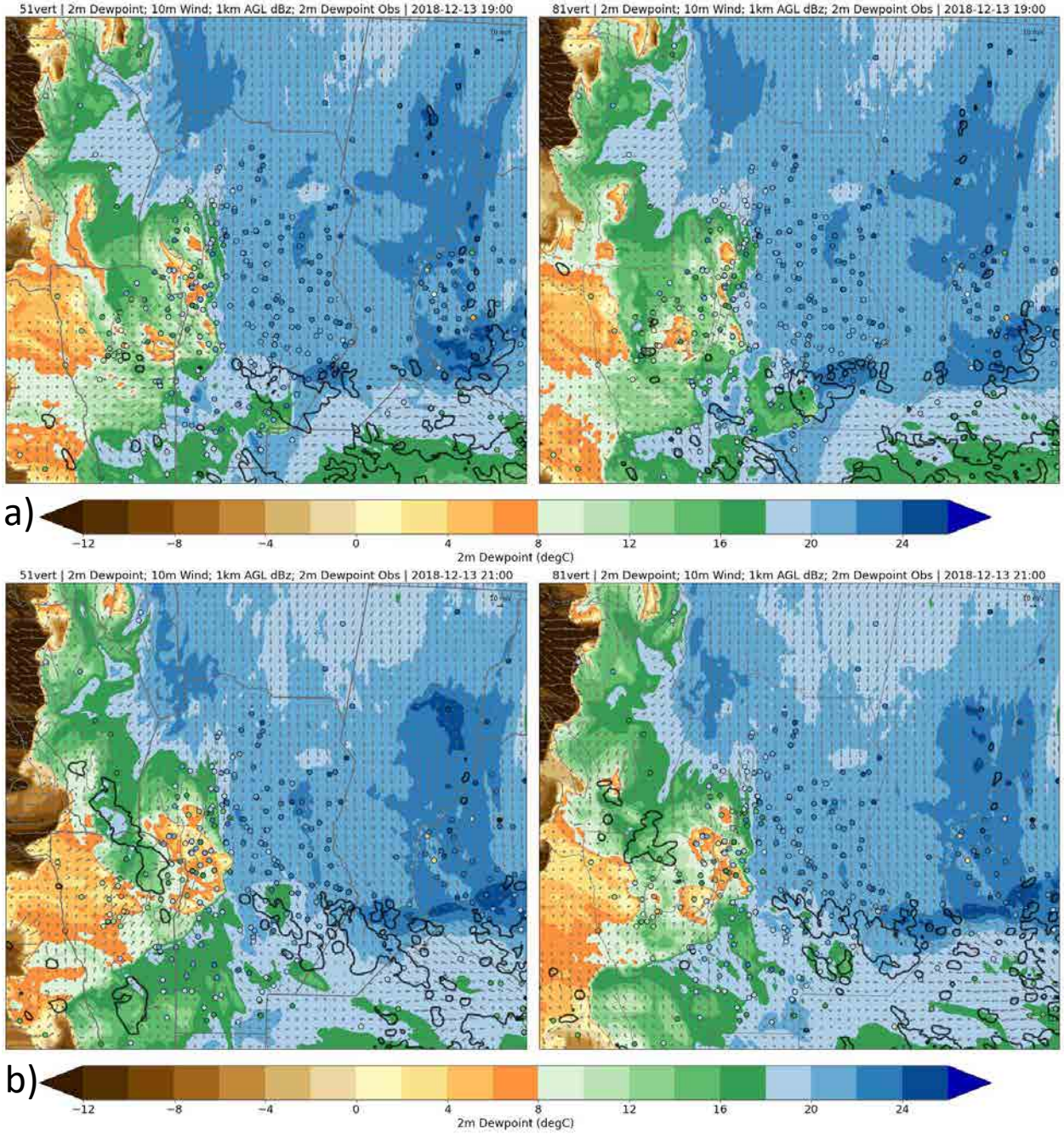

Figure 3.17: Comparison of modeled surface dewpoint in the 51vert (left column) and 81vert (right column) simulations at a) 1900 UTC 13 December and b) 21 UTC 13 December. Surface dewpoint observations are plotted with filled circles using the same color scheme as the model simulations. The 20 dBz contour of model simulated reflectivity at 1km AGL is plotted with a black contour, and modeled 10m winds are plotted with grey vectors. North is up.

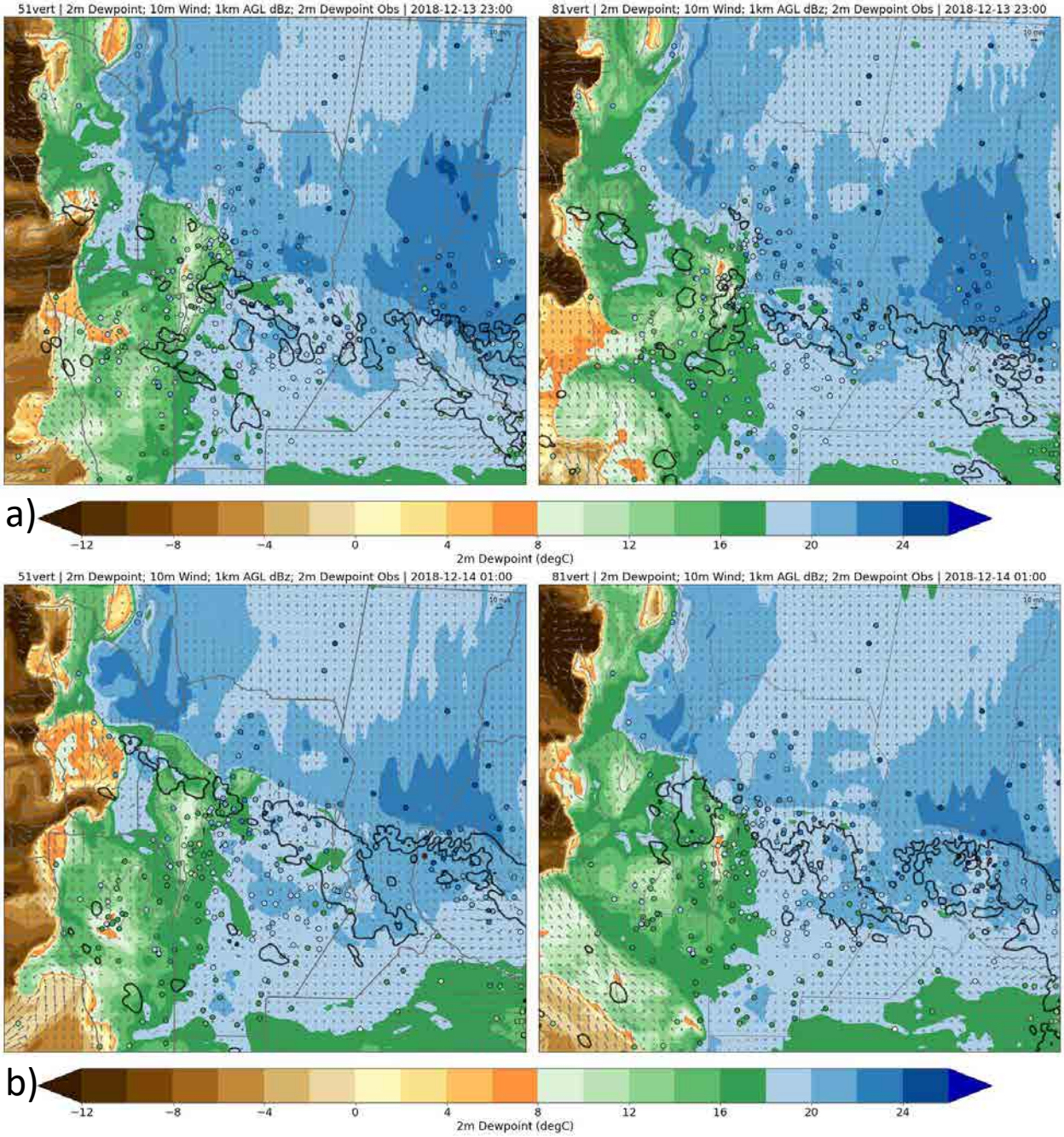

Figure 3.18: As in Fig. 3.17 but for a) 2300 UTC 13 December and b) 0100 UTC 14 December.

ongoing in all three datasets. However, both simulations initiated the supercells too early and show the location of these storms as further east than what occurred in reality. The early initiation may have been caused by a lack of mixing of dry air into the updrafts of the modeled storms, as satellite observations from earlier times than shown in Fig. 3.16 (see Fig. 3.3) show a brief burst of convection that forms in the area and at the time that the model supercells form and persist, but the observed storm dissipated after about 30 minutes. The observed supercells did not initiate until 1700 UTC 13 December, compared to 1430 UTC in the models. The early initiation of the supercells also leads to an earlier period of upscale growth for these storms compared to observations and this can be seen at 2048 UTC 13 December. The modeled MCS formed from upscale growth of the supercells has begun to backbuild into central Córdoba province at 2048 UTC, while in the actual case this has not yet occurred. Comparison between observed and modeled dewpoints at 1900 UTC and 2100 UTC (Fig. 3.17) reveals that modeled surface moisture in Córdoba province east of the SDC matches observations well. To the west of the SDC modeled surface moisture in both model simulations is less than observed, especially in northern San Luis province, with the 51vert simulation has a larger low bias than 81vert. Fig. 3.17 also shows that at both 1900 UTC and 2100 UTC the modeled 1km AGL reflectivity of both model simulations matches reasonably well.

At 2248 UTC 13 December, the first evidence of the backbuilding of the MCS in central Córdoba province during the real case can be seen (Fig. 3.16) while the modeled MCSs cover most of the southern half of Córdoba province. Cold pools from the modeled storms can be seen in Fig. 3.18, where over and east of the SDC model dewpoints affected by the cold pools are lower than observed dewpoints that have not experienced a cold pool passage. By 0048 UTC 14 December (Fig. 3.16) observed upscale growth has begun to catch up with the modeled storm, though still displaced to the south and west. At 0100 UTC modeled storms in the 51vert simulation are farther northeast than the storms in the 81vert simulation, and an area of low dewpoint accompanied by strong 10m winds is moving from San Juan province into La Rioja province is present in the 51vert simulation but not the 81vert simulation. This intrusion of dry air is not present in the observations,

which record dewpoints of 16-20°C in this region at the time compared to the modeled dewpoints of 4-8°C in the 51vert simulations. At 0100 UTC an organized line of convection has formed west of the SDC in the 51vert simulations, the western edge of which lies along the boundary between the very dry air moving down from the Andes and the moist air flowing from the north. The 81vert simulation also shows convection west of the SDC at this time, but not a well defined line and to the southwest of where the 51vert simulation places the storms. However, both model simulations place the convection west of the SDC farther north and initiating at a much earlier time than occurred in the real case. The observed case developed further south and does not yet have any cloud tops higher than 12km present at 2048 UTC (Fig. 3.16). This difference in initiation times and locations west of the SDC can be attributed to two things. First, the model simulations did not capture the outflow boundary from the morning convection that helped to organize the observed convection west of the SDC, as no such boundary exists in either of the model simulations. Since the MCS that produced this outflow boundary in the observed case was ongoing at the time of initialization of the model runs, it is not surprising that this feature was not captured. The second reason is that the modeled dewpoints in the region of initiation of convection in the observations are 5-10°C higher than they are in either of the model simulations at the time that these storms were observed to form (2100 UTC - 2200 UTC; see (Fig. 3.17).

After 0048 UTC 14 December divergence between the two simulations becomes more apparent. Fig. 3.19 depicts this by showing the comparison to mesoscale satellite imagery hourly from 0248 UTC to 0548 UTC 14 December. At 0248 UTC both the observed and modeled MCSs have grown very large, covering much of the southeastern quadrant of the mapped domain, but the observed system remains further to the southwest. As the storm moves to the east over the SDC, the observed MCS remains with the edge of its cloud shield largely parallel to the mountain range as can be seen in the bottom two panels of the figure at 0448 UTC and 0548 UTC. The modeled systems do not stay attached to the mountain range for as long. However, the 81vert model simulation can be seen to be lagging behind the 51vert simulation at 0448 UTC and 0548 UTC after matching the 51vert simulation fairly well at 0248 UTC, indicating that the 81vert simulation

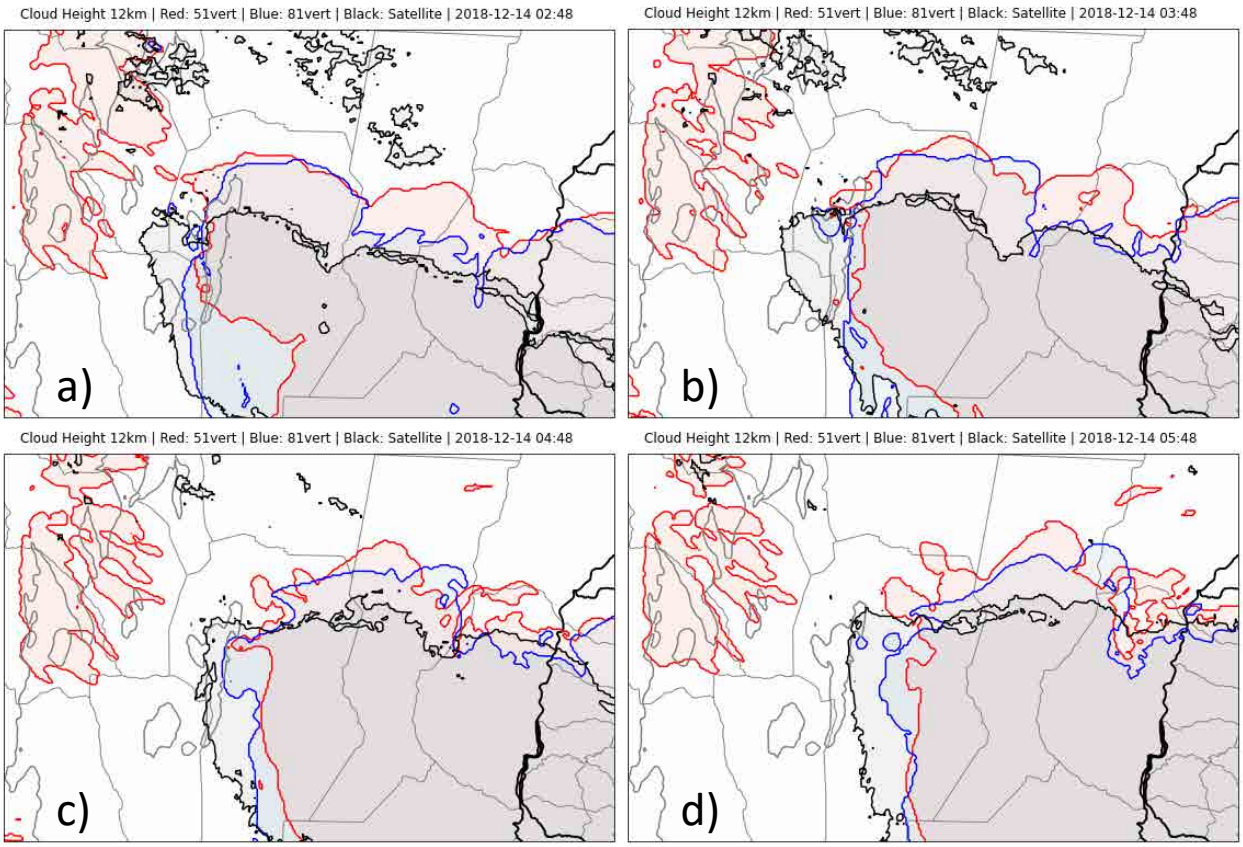

Figure 3.19: Same as Fig. 3.16; except every hour starting at 0248 UTC 14 December.

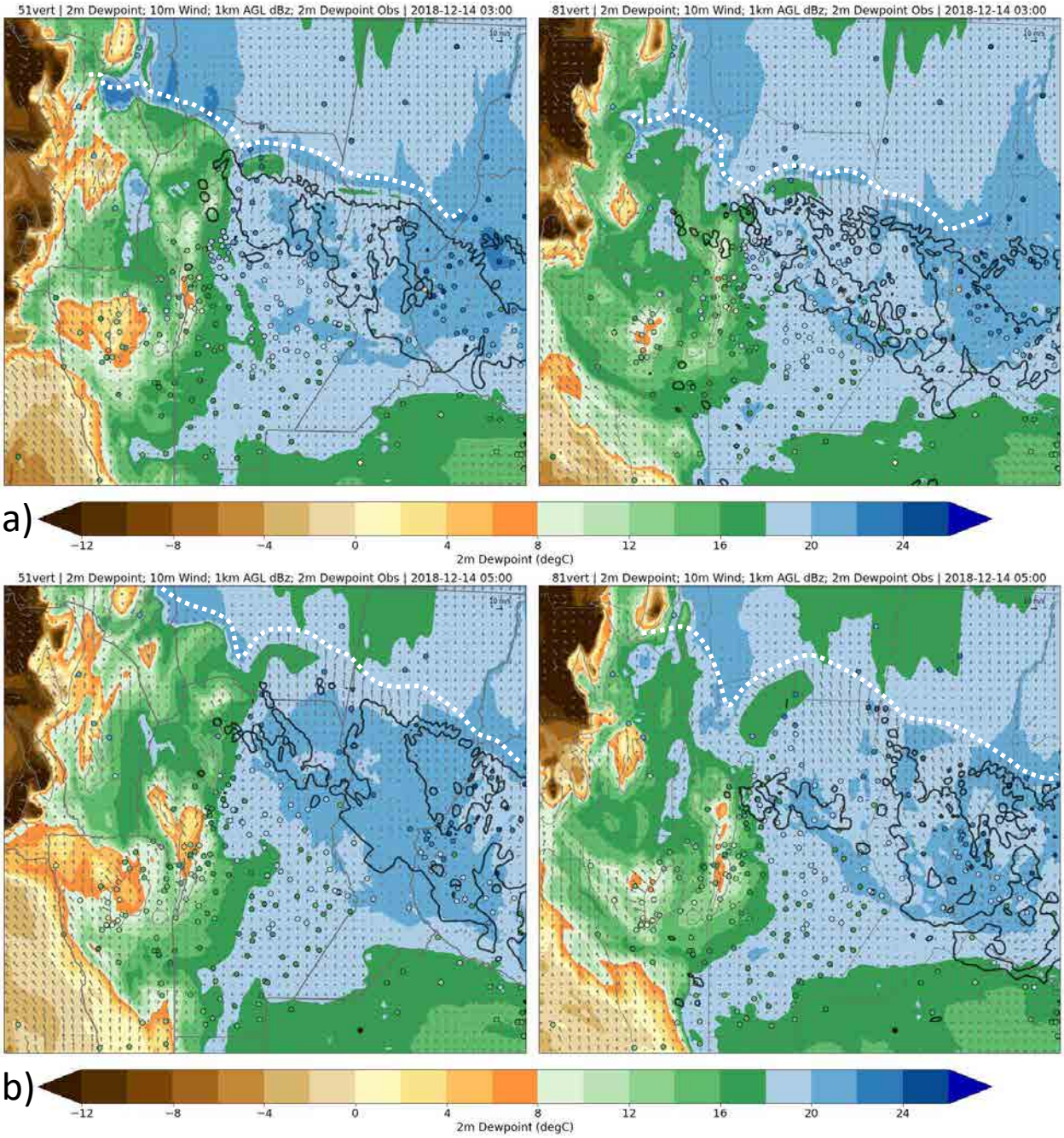

Figure 3.20: As in Fig. 3.17 but for a) 0300 UTC 14 December and b) 0500 UTC 14 December. White dashed lines denote the dewpoint boundary discussed in the text.

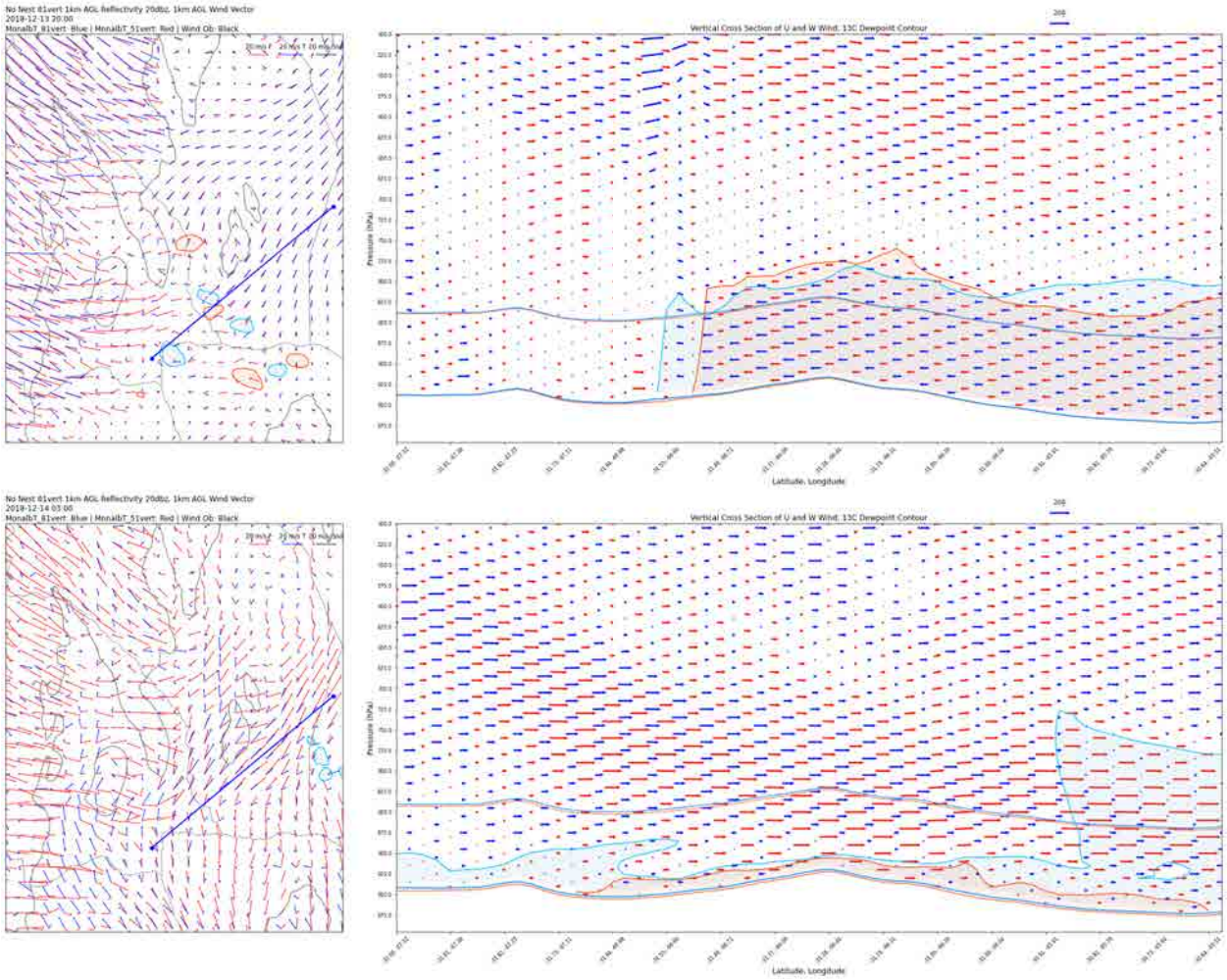

Figure 3.21: a) 1km AGL wind vectors and 20dbz 1km AGL reflectivity conotour at 2000 UTC 13 December. Blue vectors and contours represent the 81vert simulation; red vectors and contours the 51vert simulation. The thicker grey contour is the 1000m terrain elevation contour. b) Cross section of the 13°C dewpoint contour and in-plane wind along the blue line in left plot, blue contours and vectors are 81vert and red contours and vectors 51vert. Areas with dewpoint greater than 13°C are shaded. Surface and 1km AGL pressure are also contoured. c) and d) are the same as a) and b) respectively but for 0300 UTC 14 December.

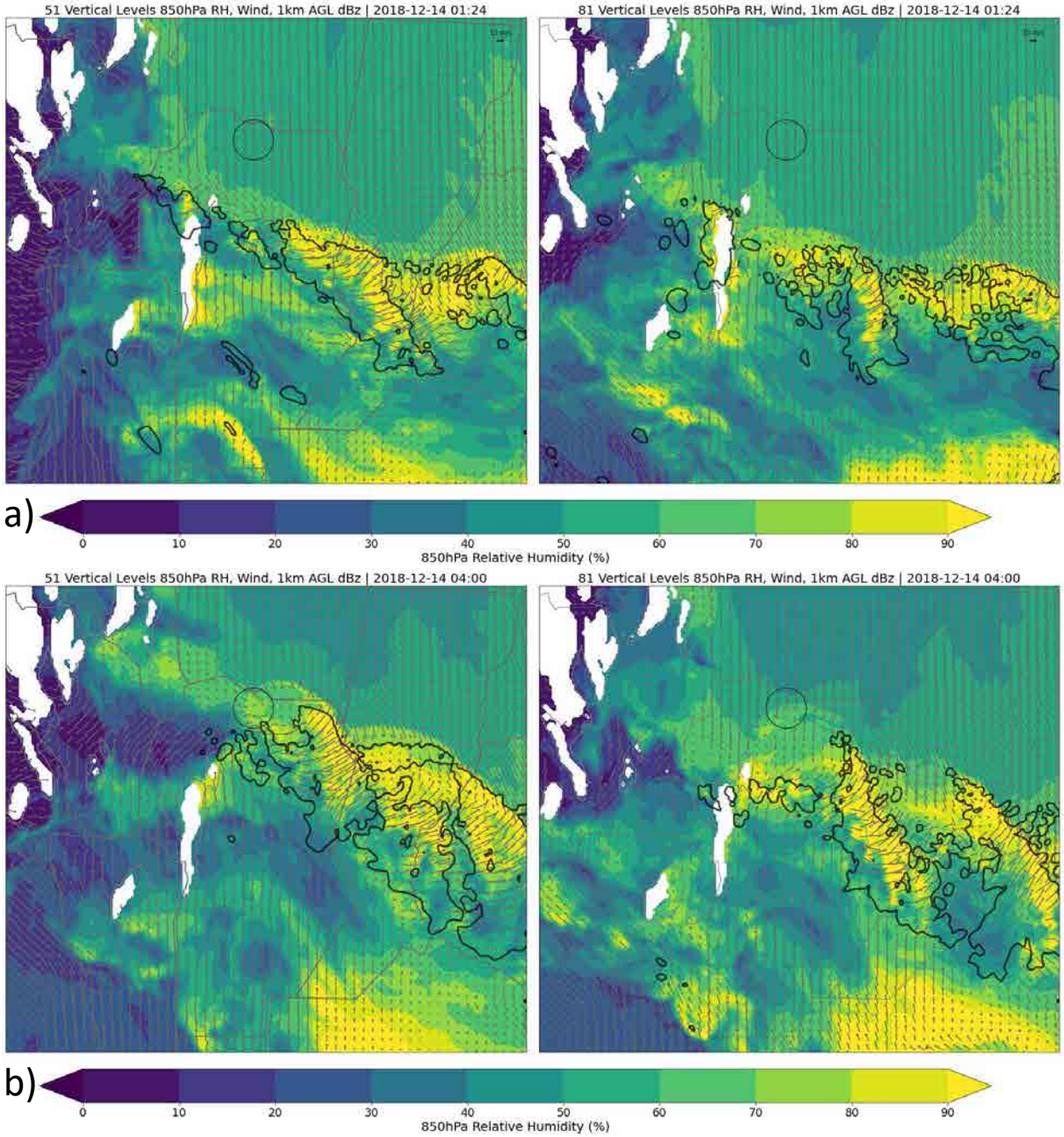

Figure 3.22: Comparison of modeled 850hPa relative humidity in the 51vert (left column) and 81vert (right column) simulations at a) 0124 UTC 14 December and b) 0400 UTC 14 December. The 20 dBz contour of model simulated reflectivity at 1km AGL is plotted with a black contour, and modeled 850hPa winds are plotted with grey vectors. The center of the black circle denotes the location of the Villa de María del Río Seco sounding location, shown in Fig. 3.24. 850hPa wind observations from soundings launched within a half hour of the nominal time are plotted with black vectors. North is up.

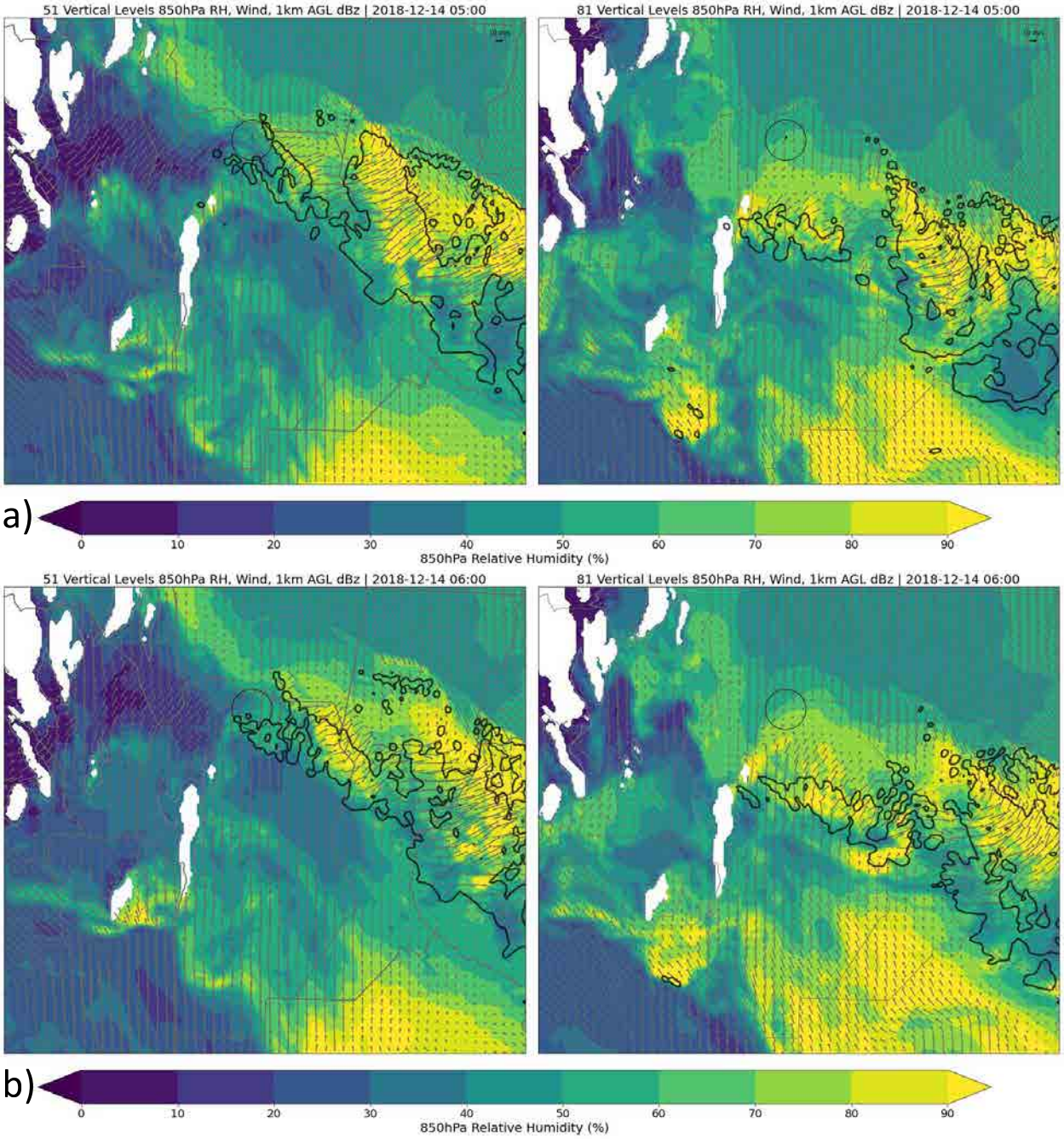

Figure 3.23: As in Fig. 3.22 but for a) 0500 UTC 14 December and b) 0600 UTC 14 December; spanning the time covered by Fig. 3.24.

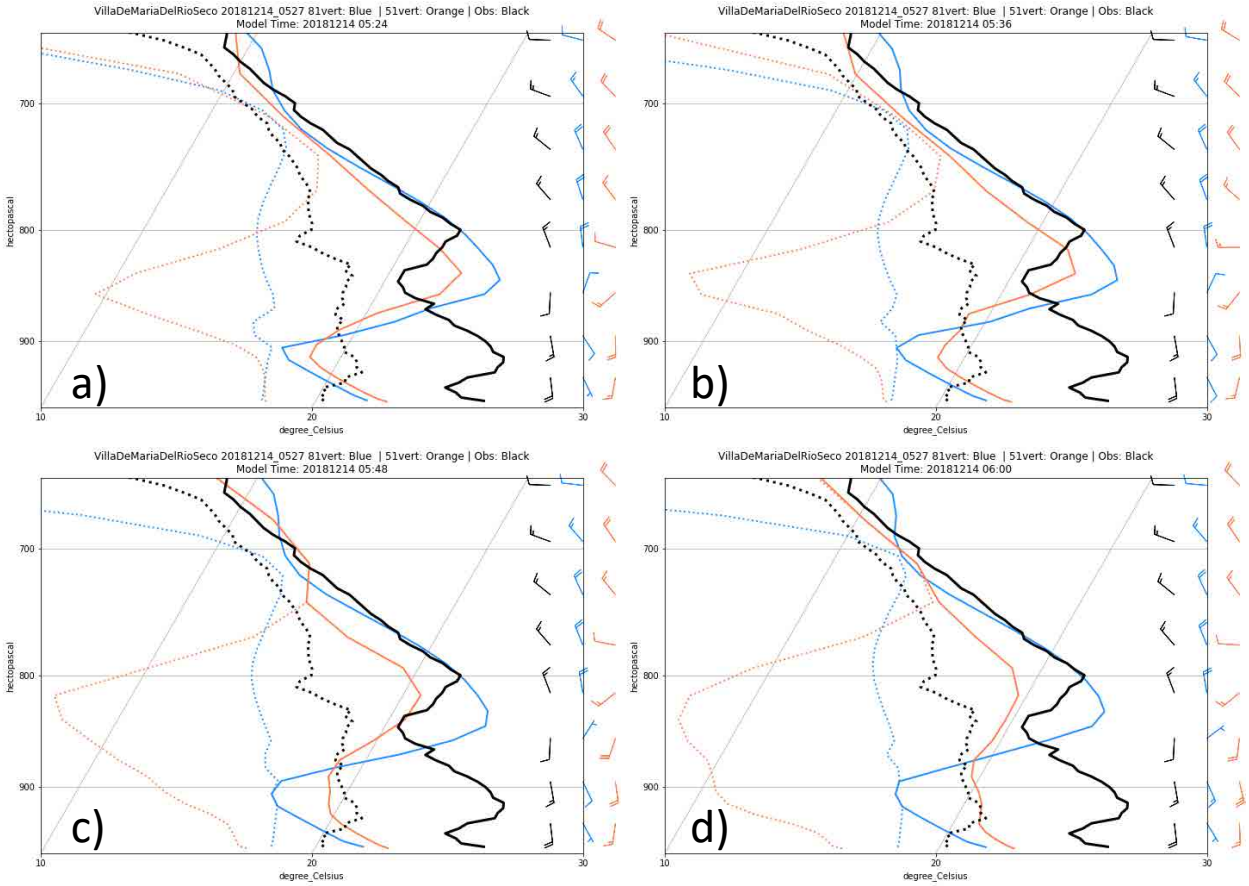

Figure 3.24: Comparison of skew-T charts of modeled soundings at a) 0524 UTC 14 December, b) 0536 UTC 14 December, c) 0548 UTC 14 December and d) 0600 UTC 14 December to the observed sounding at the same location (Villa de María del Río Seco; at the center of the black circle in Figs. 3.22 and 3.23) launched at 0527 UTC 14 December. Dewpoint lines are dashed, temperature lines are solid, and wind barbs for selected levels are presented on the right side of each panel. The 51vert sounding is orange, 81vert blue, and observed black. Also plotted are wind barbs for selected levels on the right side of each panel.

contains more backbuilding than the 51vert simulation. Fig. 3.20 presents a comparison of 2m dewpoint in both model simulations and compared to surface dewpoint observations during the period of backbuilding. At 0300 UTC 14 December the model simulations show significant differences. Surface dewpoint west of the SDC remains lower than observations at many stations in both model runs. The 51vert model run also shows a sharp boundary between the lower dewpoints west of the SDC and the very moist air to the north, whereas in the 81vert simulation this boundary is not as sharp and lies further south. The vertical structure of moisture and winds along a line perpendicular to this boundary makes plain why these differences in the modeled surface dewpoint exist (Fig. 3.21). At 2000 UTC 13 December both the 51 and 81vert simulations show the northeasterly surge of moist air with the low level jet ending in a dry line like boundary between the moist air (represented in the figure with the 13°C dewpoint contour) and the dry air south of the boundary. There are large differences in 1km AGL wind vector between the two simulations at these times. At 2000 UTC strong winds can be seen in the 51vert model run beginning to move off of the Andes foothills and into the region west of the SDC. The 81vert simulation shows strong winds confined to higher elevations. At 0300 UTC 14 December the area of strong northeasterly winds in the 51vert simulation has continued to expand, while in the 81vert simulation winds have calmed on the higher terrain while winds forced by the lee trough move into the region from the south. At 0300 UTC, the depth of the 13°C contour has decreased significantly, indicating that moisture has been advected away from the region by the winds descending the Andes. Moisture is also being advected away in the 81vert simulation, but the origin of the winds causing this advection is southerly winds from Patagonia induced by the lee trough carrying more moisture than the wind descending from the mountains. This can be seen by the fact that the southwestern corner of the map domain in the 0300 UTC 14 December plot in Fig. 3.21 shows southeasterly winds in the 81vert simulation at the same locations as the 51vert simulation shows calm winds or even north-westerlies as a result of the downslope flow.

The effect that this removal of moisture had on the ongoing convection over the SDC at 0300 14 December can be seen in Figs. 3.22 and 3.23. At 0124 14 December (Fig. 3.22) the convection

west of the SDC discussed above can be seen, but in the 51vert simulation the western edge of this convection is being intruded by the very dry winds from the mountains, as can be seen by 850hPa relative humidity of less than 30%. The 81vert simulation at this same time shows convection over the northern end of the SDC, and a few cells to the west, largely surrounded by 850hPa relative humidity values of more than 50%. A few hours later, at 0400 UTC, the area of very low 850hPa relative humidity in the 51vert simulation has expanded into the area covered by convection at 0124 UTC. The 81vert simulation shows a similar area of low relative humidity at 850hPa at both 0124 UTC and 0400 UTC, but the associated winds are weaker and the surge of dry air does not reach Córdoba province. This leaves moisture available for the convection that at 0400 UTC is ongoing at the northern end of the SDC in the 81vert simulation, while in the 51vert simulation convection is almost entirely off the terrain. This process continues through 0500 UTC and 0600 UTC (Fig. 3.23), and dry air can be seen impinging on the Villa de María del Río Seco sounding site during the period.

Comparing the sounding taken at this site at 0527 UTC 14 December to model soundings for the period 0524 UTC to 0600 UTC (Fig. 3.24) shows the drying in the lower levels (below 750hPa) in the 51vert simulation associated with the downslope wind. This drying is not observed in the 81vert simulation, which is closer to the observed sounding with northerly wind below 850hPa and southerly wind above (compared to the steadily backing wind in the 51vert sounding) and no strong decrease in dewpoint between the surface and 800-850hPa. At the time of the soundings, modeled convection is passing over the site in the 51vert simulation which is the cause of the saturation in the skew-T above the drying layer. By 0600 UTC 14 December 850hPa relative humidity is below 50% around the SDC in the 51vert simulation while in the 81vert simulation the low level jet continues to reach the northern SDC, with 850hPa relative humidity in the inflow region greater than 60%. These differences in moisture availibility result in backbuilding convection over the SDC in the 81vert simulation while the 51vert simulation depicts a system contending with dry air as it moves to the northeast. The next section will examine the reason why the 51vert simulation produced strong dry winds off of the Andes and the 81vert simulation did not.

3.3.3 Differences Between Model Simulations

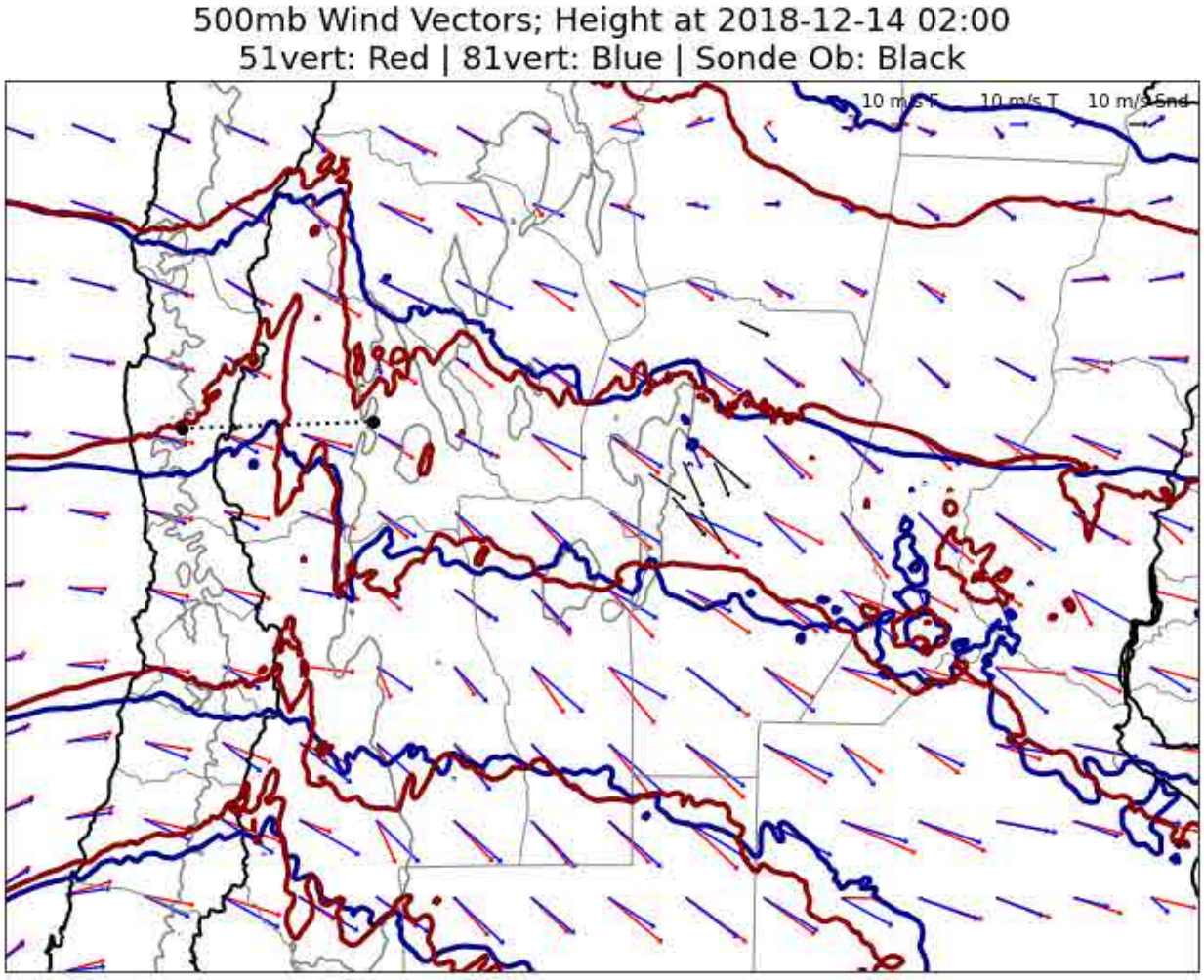

Figure 3.25: 500hPa wind and height at 0200 UTC 14 December. Red vectors and contours are from the 51vert simulation, blue vectors and contours are from the 81vert simulation. The black dotted line shows the line of the cross sections presented in Figs. 3.26 - Fig. 3.33.

At 0200 UTC 14 December the 500hPa trough axis has nearly reached the spine of the Andes, and flow is nearly perpendicular over the mountain crest (Fig 3.25. A smaller mountain induced trough can be seen along the spine of the Andes. This smaller trough is deeper in the 51vert simulation than in the 81vert simulations. This is due to the flow over the barrier being faster in the 51vert simulation, which can also be seen by comparing the wind vector arrows. Fig. 3.26 displays the difference in vertical resolution between the two simulations and the vertical velocity

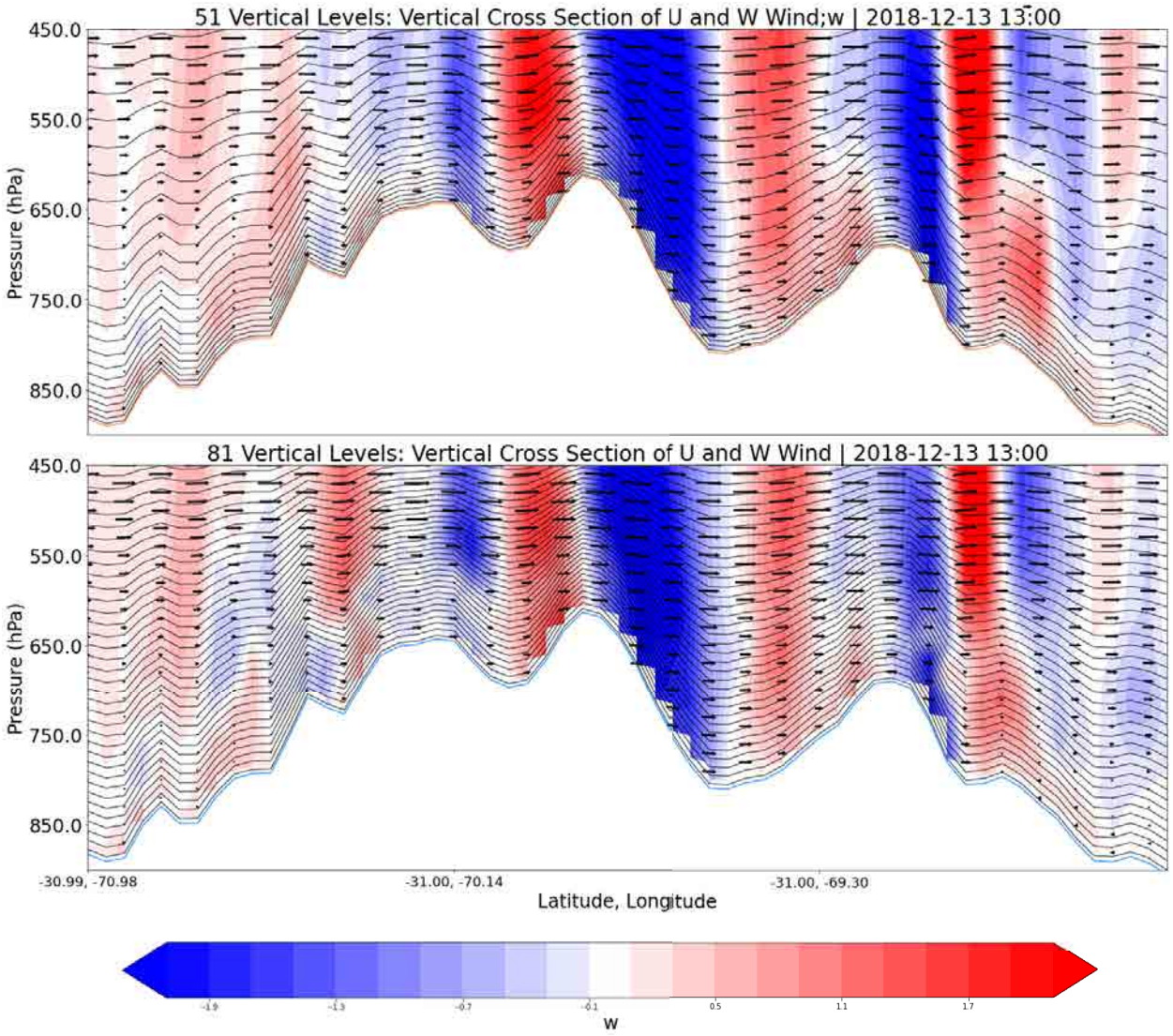

Figure 3.26: Cross section of vertical velocity along the black dotted line in Fig. 3.25 for 51vert (top) and 81vert (bottom) at 1300 UTC 13 December. Model levels (black lines) are also plotted for each simulation.

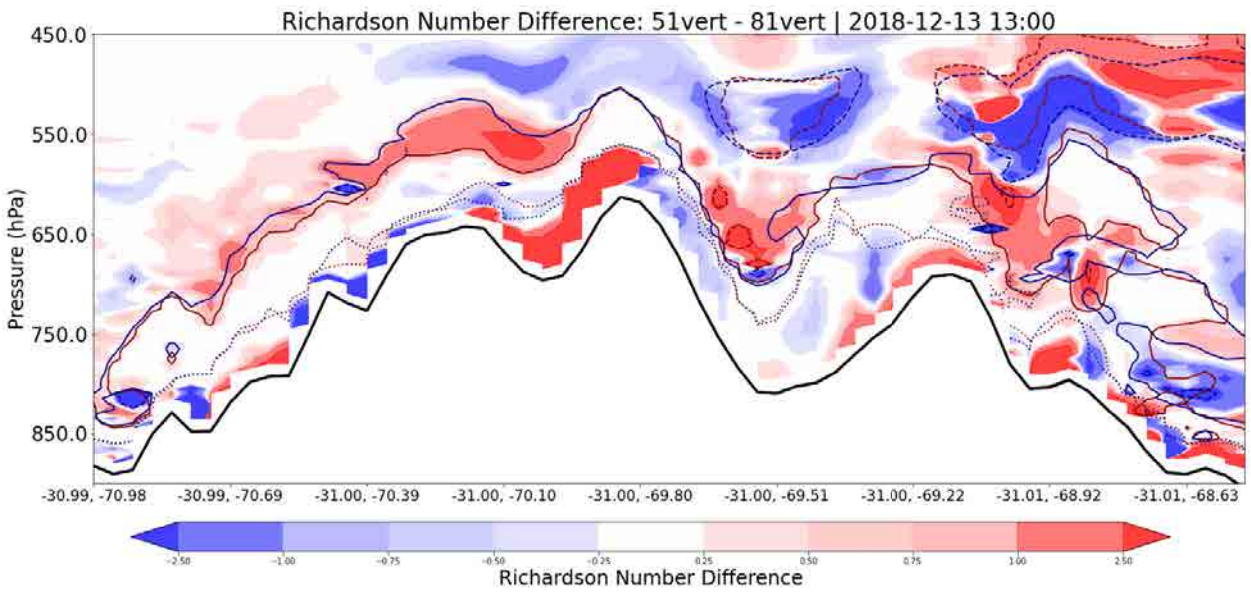

Figure 3.27: Difference between Ri, 51vert minus 81vert such that areas Ri is larger (smaller) in the 51vert simulation are colored red (blue). Also plotted for each simulation are the contours of Ri = 0 (dotted), Ri = 1 (solid) and Ri = 5 (dashed) with blue contours from the 81vert simulation and red contours from the 51vert simulation. Surface pressure is contoured with a thick black line.

in each simulation at 1300 UTC December 13, one hour into the simulation. Key differences in the behavior of the flow over the mountains can be seen. Both simulations show strong mountain waves but at the largest inflection points along the terrain profile, near 70W and just east of 69.3W, reductions in the in-plane wind speed and corresponding disruptions to the vertical velocity pattern can be seen in the 81vert simulation relative to the 51vert simulation. This indicates that at these inflection points the higher fidelity to the shape of the mountain range in the 81vert simulation allows for the generation of turbulence in the flow that is able to impart a drag on the flow.

Fig. 3.27 shows the impact that this slow down in the flow has on the Richardson number (Ri). Ri represents the ratio of buoyancy forces to shear forces, and when the number is below 0.25 turbulence is prevalent. The depth of Ri < 1 is larger in the 81vert simulation than the 51vert simulation at one hour into the simulations, particularly over the westernmost (leftmost on the figure) high peaks of the Andes at this latitude. A cross section of potential temperature at the same time (Fig. 3.28) indicates minimal differences between the two simulations, therefore the difference in Ri between the two simulations is primarily a result of the shear caused by the layer

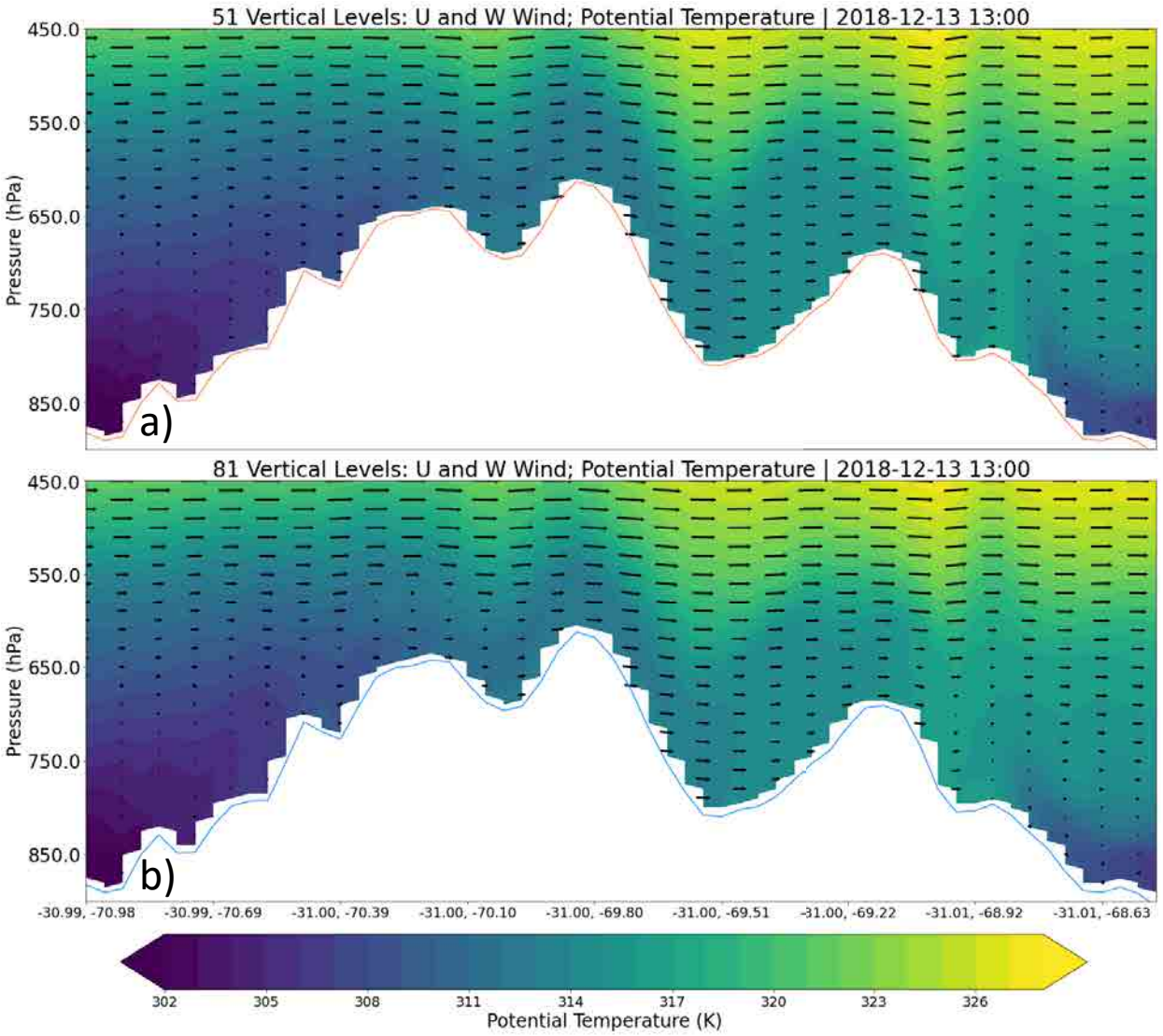

Figure 3.28: Cross section of potential temperature along the dotted black line in Fig. 3.25 at 1300 UTC 13 December.

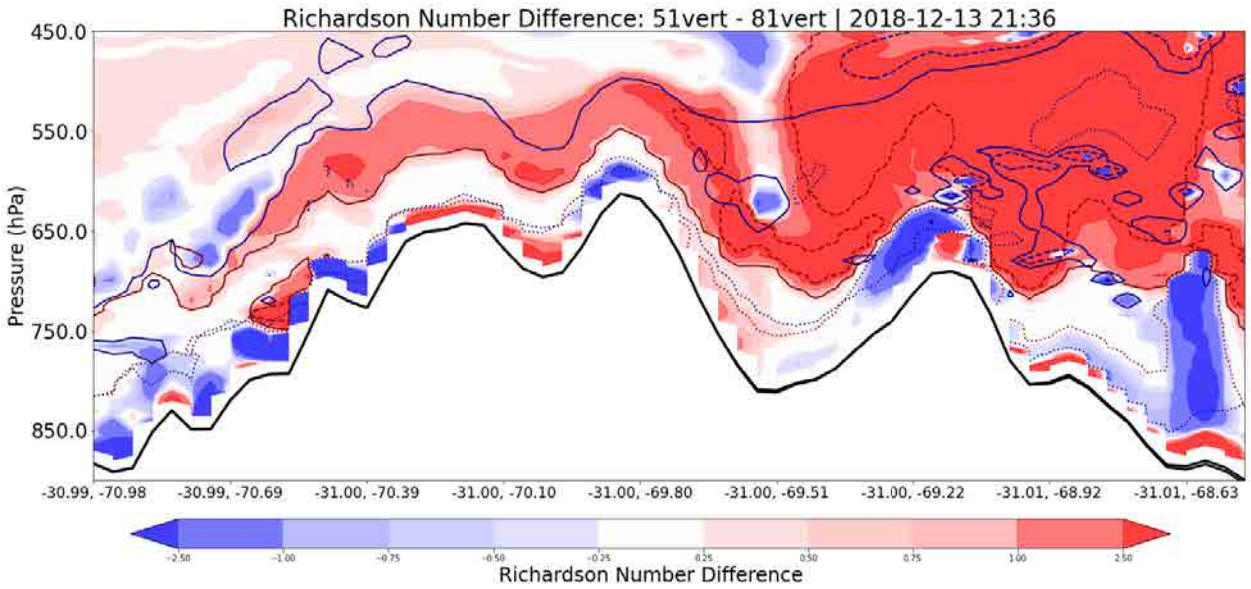

Figure 3.29: As in Fig. 3.27 but for 2136 UTC 13 December.

of reduced wind speed in the 81vert simulations. At this time both simulations show a potential temperature pattern consistent with the strong mountain wave depicted in Fig. 3.26. Later in the simulation time at 2136 UTC 13 December the differences in Ri become much more apparent, as seen in Fig. 3.29. The 81vert simulation has more area at Ri < 1 than 51vert, with the Ri = 1 contour at a lower pressure in the 81vert simulation across the entire cross section. Fig. 3.30 illustrates that at this time, winds east of the easternmost mountain peak below 650hPa in the 81vert simulation are consistently lower than the corresponding winds in the 51vert simulation. Also, downstream of the Andes the column is much more mixed in the 81vert simulation, while the 51vert simulation depicts closely spaced isentropes above 650mb, which contributes to the higher Ri indicated by the 51vert simulation for this layer. The 51vert simulation also still has clear characteristics of a strong mountain wave, while the isentropes in the 81vert simulation show a much weakened wave. Fig. 3.31, also at 2136 UTC, the 81vert simulation shows evidence of a trapped lee wave, with rotors occurring beneath gentle waviness aloft. These rotors are particularly apparent between 69.2W and 67.5W, and compared to the 51vert simulation relatively quiescent conditions prevail at the surface beneath these features. The 51vert plot shows strong vertically propagating gravity waves accompanied by strong differences from the 81vert simulation associated with a feature at

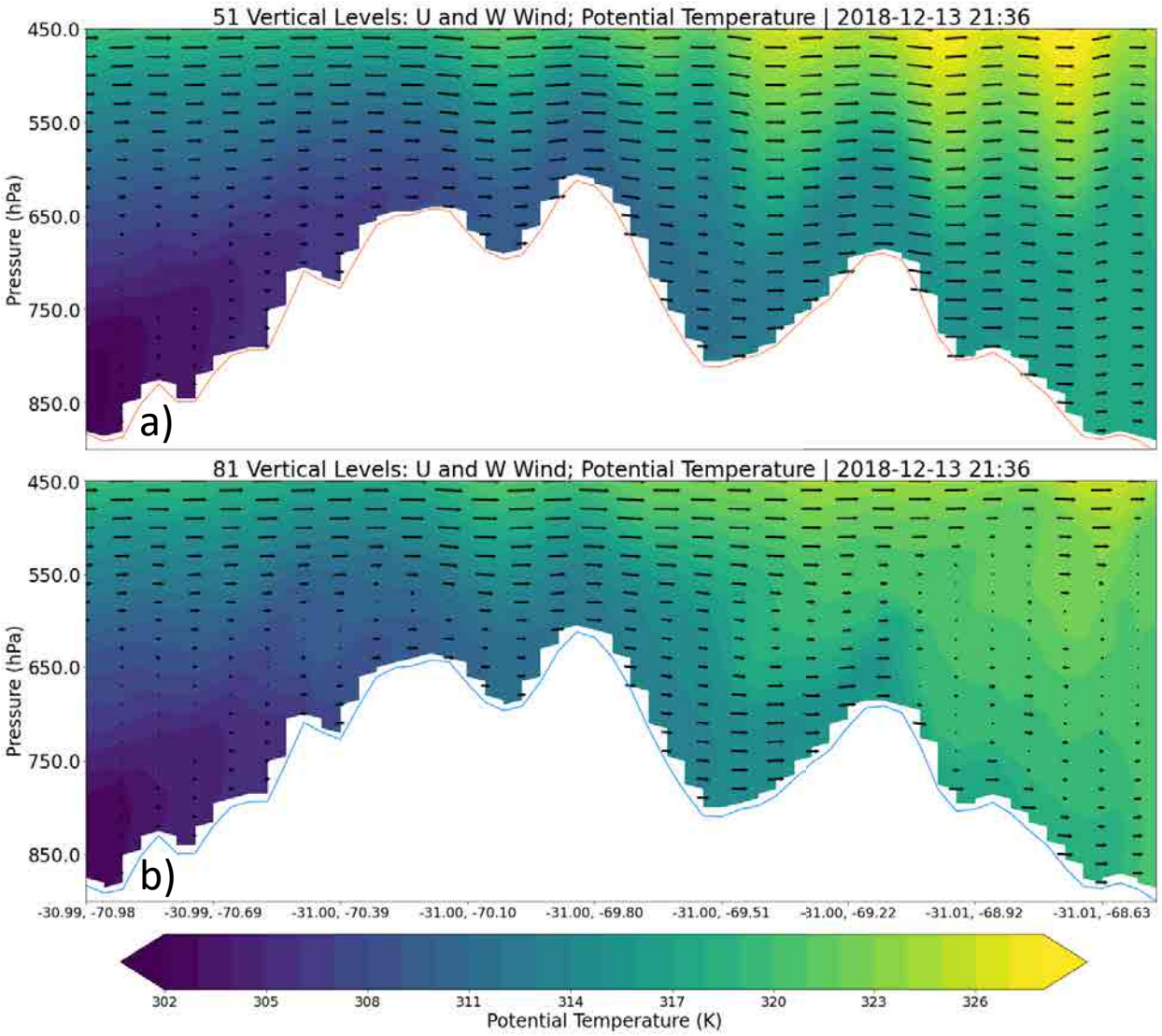

Figure 3.30: Same as Fig. 3.28 but for 2136 UTC 13 December

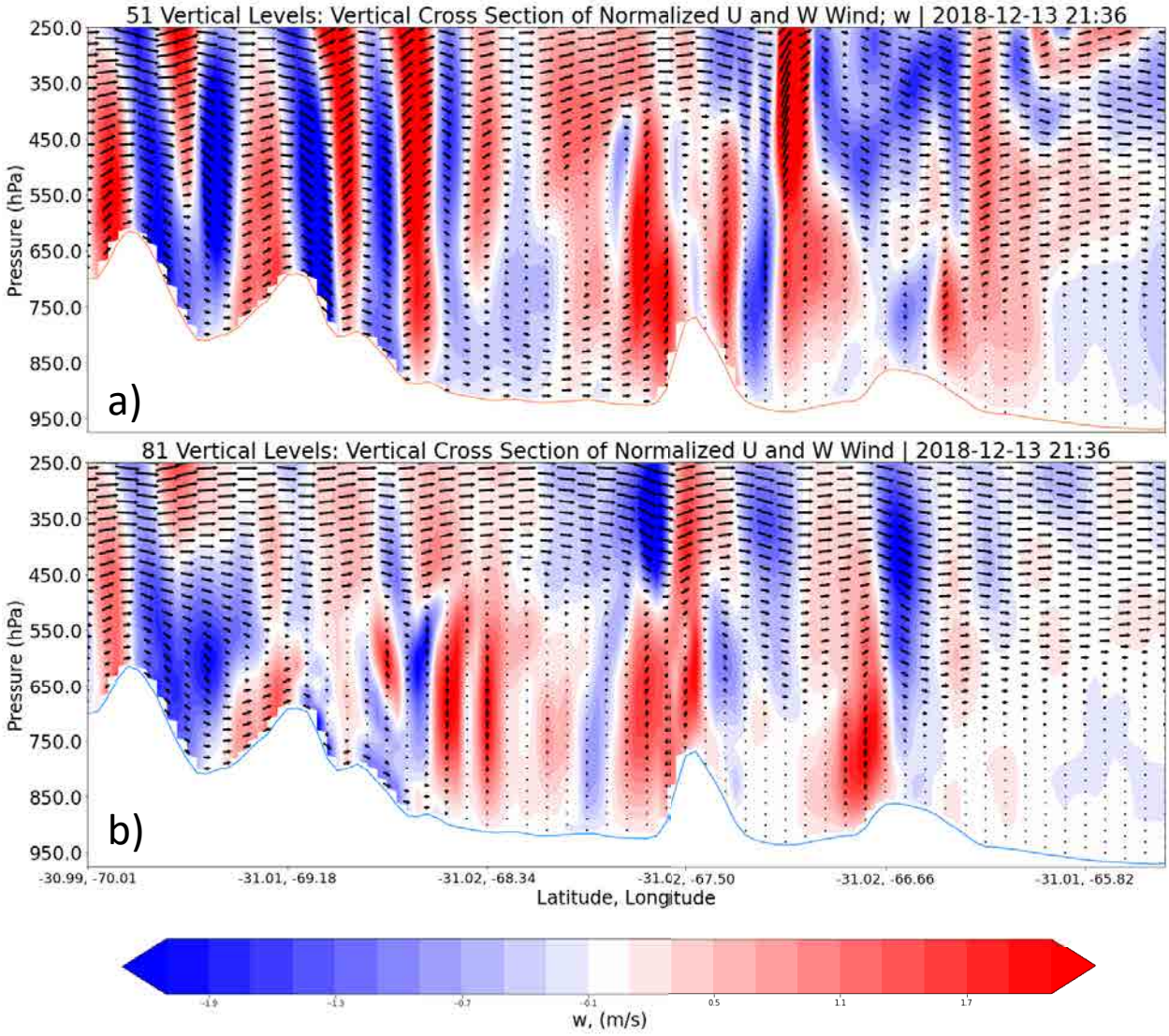

Figure 3.31: Cross section of vertical velocity along the same line of latitude (31S) as Figs. 3.26 - 3.30 but extended to the east (65.5W instead of 68W) and starting further west (70W instead of 71W) at 2136 UTC 13 December. To more easily see vertical motions, each wind vector has been normalized to the maximum component in the 51vert simulation along both the U and W axis; ie W = W/51vert W maximum and U = U/51vert U maximum. 51vert simulation is on top, 81vert on the bottom.

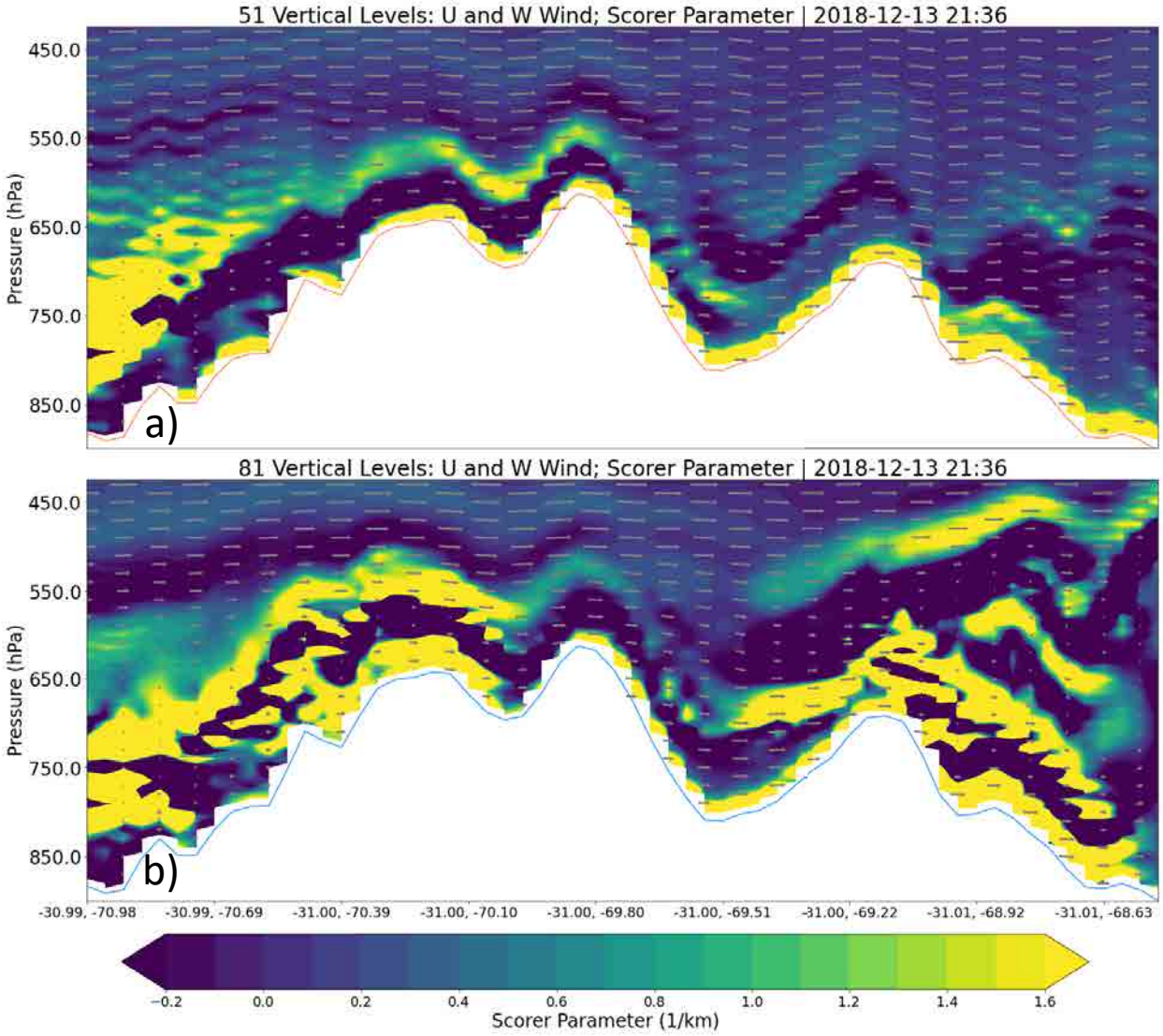

Figure 3.32: Cross section of Scorer parameter along the dotted line in Fig. 3.25 at 2136 UTC 13 December.

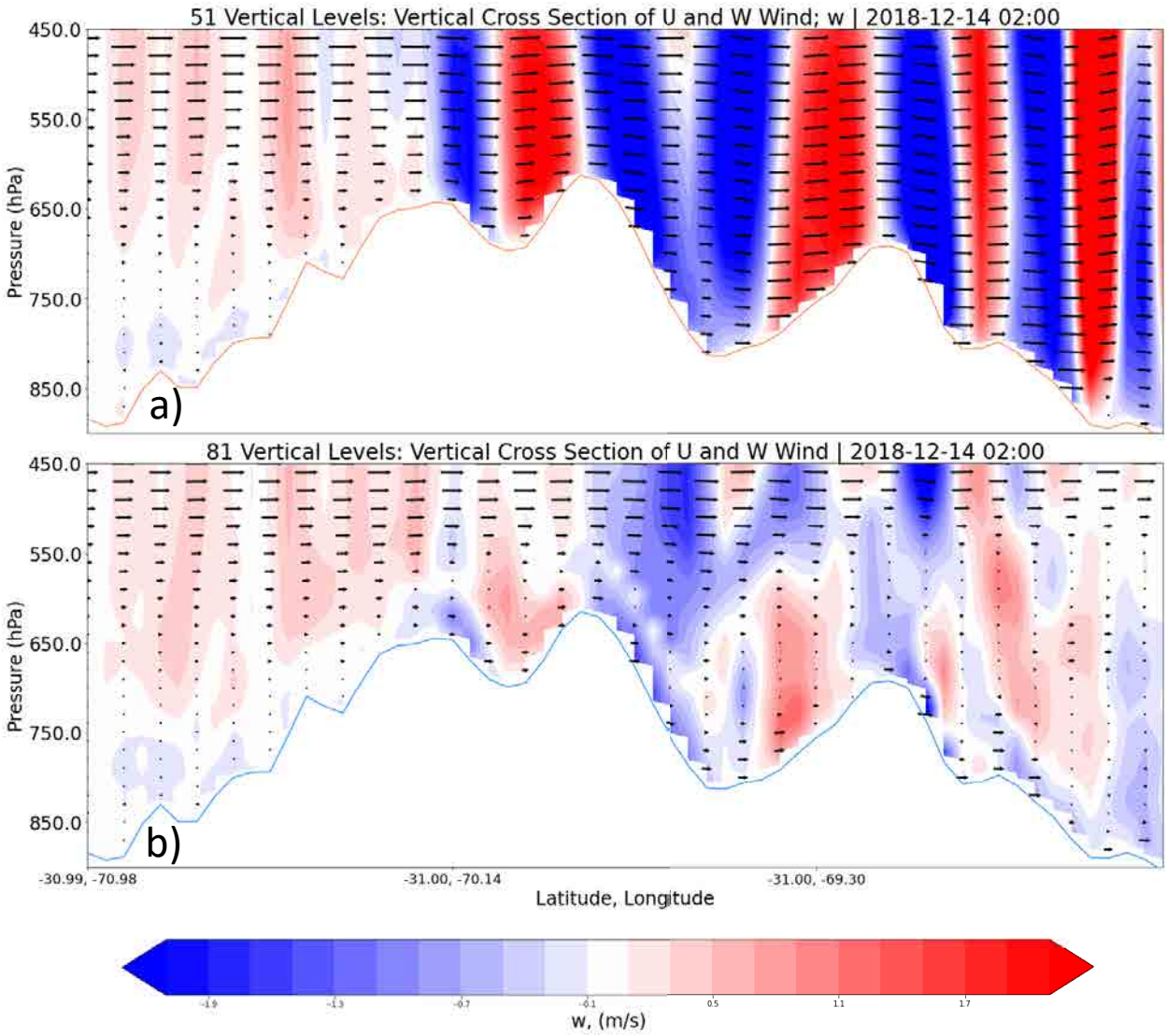

Figure 3.33: Same as Fig. 3.26 but at 0200 UTC 14 December and without plotting model levels.

the surface near 67.5W. Strong westerly winds prevail on the surface behind this feature, along with a strong pattern of ascent and descending columns that extend through the troposphere. Fig. 3.32 shows the Scorer parameter for the cross section along the black dotted line in Fig. 3.25 at 2136 UTC 13 December, the same time as Fig. 3.31. When the Scorer parameter decreases with height, conditions are good for vertically propagating gravity waves, while when it increases with height conditions are good for trapped lee waves (e.g. Mayer et al. (2012)). For flow over the eastern most peak in this cross section (around -69.22 longitude) the 51vert simulation presents good conditions for vertically propagating waves, with the scorer parameter mostly decreasing with height, particularly above 600hPa. The 81vert simulation displays the opposite pattern, with one layer of higher scorer parameter following the terrain over the barrier at between 750hPa and 650hPa and another layer of high scorer parameter between 600hPa and 450hPa. Fig. 3.33 shows vertical velocity along the same cross section at 0200 UTC 14 December. By this time wave activity in the 81vert simulation is substantially reduced and winds are relatively light below 600hPa, while in the 51vert simulation the mountain wave event continues unabated. These major differences in representation of the mountain wave event during this case had large implications for moisture availability upstream of the SDC during the period of backbuilding along that mountain range, with the mountain wave int he 51vert simulation scouring out the deep layer of moisture advected there by the low level jet while the shorter and less intense wave event in the 81vert simulation did not remove this moisture as quickly or as completely. Both simulations had less moisture in the region west of the SDC than observations, since in the observed event downslope winds advecting very dry air from the peaks of the Andes did not extend far from the base of the foothills and dewpoints west of the SDC mountains did not drop significantly until the arrival from the south of drier air advected by winds induced by the lee trough. Furthermore, the overprediction of the mountain wave also changed the location of key boundaries that led to convective initiation by creating a dryline that the modeled convection formed along west of the SDC that was not present in the real case.

3.3.4 The Event in Context: Results from a Tracking Algorithm

The question remains: What can this one case tell us about other significant cases in the region? How often would a model creating a spurious downslope windstorm negatively affect the forecast of potentially hazardous convection? To put this event in context and answer these questions a tracking algorithm was developed. This algorithm utilizes the GPM IMERG Final precipitation data, with half hour temporal resolution and 0.1 degree spatial resolution. The data used to construct the dataset covers the period from 1 July 2000 to 1 July 2021. For each half hourly time step creates contours of precipitation rates exceeding 1mm per hour, keeping any with an area greater than 400km^2. When contours are drawn for the next time step any contours that overlap with contours from the previous timestep are considered to be the same system. The algorithm also keeps track of metrics such as maximum precipitation rate for each system at each time step. Fig. 3.34 shows the location of the centers of contours occurring in conjunction with IMERG 99th percentile 3-hour precipitation events as described in Chapter 2 that occurred at the gridpoint nearest the city of Corodba (marked with black star on the figure). For clarity, only the five centers for each time for each event with the highest rain rates are plotted. The plot shows the system centers starting at 6 hours before the end of the event (top left) to 3 hours after the end of the event. At 6 hours before the end of the 3-hour event time, the highest concentration of system centers can be found to the west and southwest of the gridpoint the event occurred at. 3 hours before the end of the event (the beginning of the 3 hour accumulation period), the concentrations immediately south and west of the gridpoint is increased. The end of the event accumulation period is marked by system centers concentrated directly over the event gridpoint, and 3 hours after the end of the accumulation period the system centers are much more scattered, with a slightly concentration around a northwest to southeast line lying to the northeast of the gridpoint. Many of the centers of systems occurring at the same time as a 99th percentile 3 hour precipitation event was beginning were observed in the region west of the SDC near the triple border of Córdoba, San Luis, and La Rioja provinces. This region was affected by the removal of moisture due to the over prediction of the mountain wave in the the 51vert simulation, indicating that forecasts of other events may be affected by a similar poor

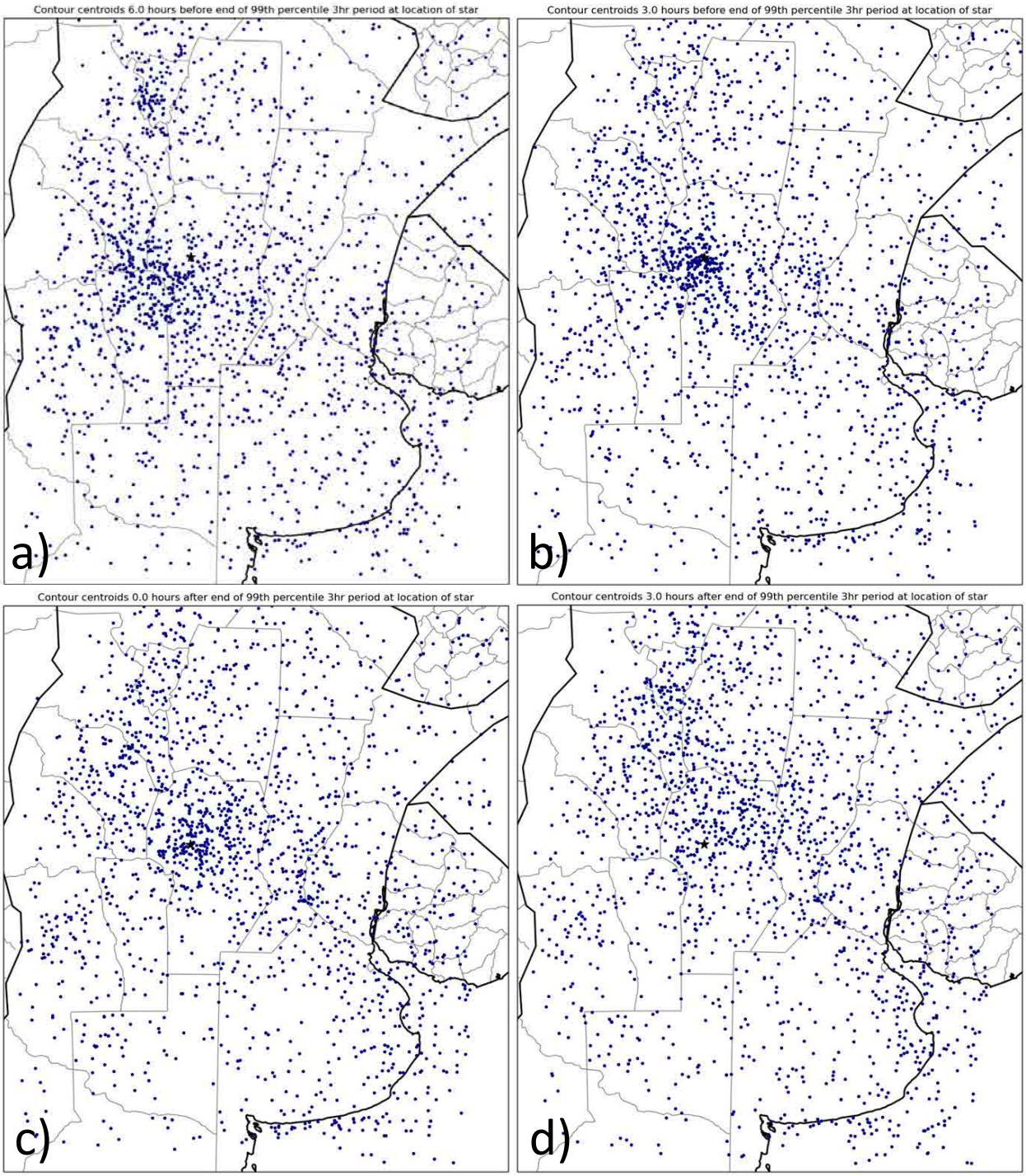

Figure 3.34: System centers as identified by the IMERG tracking algorithm at a) 6 hours before the end of 99th percentile three hour events as defined in Chapter 2 at Córdoba (black star), b) 3 hours before, c) end of event, d) 3 hours after the end of the event.

predictions of mountain waves, especially in strongly forced scenarios involving a strong trough with high winds crossing the Andes.

3.4 Chapter 3 Conclusions

The 13-14 December event provided an excellent case study into the processes of convection in Córdoba province in central Argentina. The large MCS observed during this period exhibited backbuilding behavior leading to substantial rainfall. Small hail was also observed with the storm, which stretched from Córdoba to off the Atlantic coast of Argentina. Operation forecast models of the RELAMPAGO field campaign did not capture the backbuilding aspects of this storm well, and instead moved the storm through the region quickly. This study has shown that an increase in the number of vertical levels in the WRF model substantially improved the forecast of mountain wave conditions that in turn had a strong impact on the evolution of the 13-14 December case. The increase in vertical levels resulted in a reduction of wind speed just above the surface at the strongest inflection points along the west-east terrain profile of the Andes mountains, and this reduction of wind speeds created an environment less conducive to strong downslope winds in the lee of the Andes. In the real-time models, this downslope windstorm removed moisture from the inflow of the storm leading to a lack of backbuilding behavior in the modeled storm with 51 vertical levels. With 81 vertical levels these effects were mitigated but still present, and some backbuilding did occur in the 81vert simulation. These simulations confirm the results of other studies that indicate that in forecast situations where the impact of mountain waves is important, increasing model vertical resolution can help to obtain a better forecast.

Chapter 4

Overall Conclusions

Argentina's complex weather provides a challenge for researchers and forecasters alike, compounded by the difficulties presented by a data sparse region. Due to the lack of a dense network of long term rain gauges, studies of the characteristics of heavy rainfall in the region on small spatial or temporal scales must be undertaken using either satellite or reanalysis QPE products. This study investigated characteristics of 3-hour rainfall above the 99th percentile in four datasets: IMERG, TRMM, ERA5 and MERRA2 after regridding each of these datasets to the MERRA2 0.5 degree latitude by 0.625 degree longitude grid using a method that preserves the rainfall volume. These products each have their own biases regarding what 3-hour periods meet the 99th percentile threshold and what the value of that threshold is. Reanalysis datasets had lower threshold values. Between each pair of datasets, only 40-50% of events overlapped. An event occurring within one three hour timestep at the same or an adjacent gridpoint was considered an overlap. Due to this lack of overlap between events, large differences in thermodynamic environments were observed. MERRA2 events were found to occur in environments with the lowest CAPE and PWAT, while IMERG and TRMM events were associated with higher CIN than either of the reanalysis datasets. To further investigate the storms that produce these rainfall events the RELAMPAGO campaign was undertaken in Argentina. This campaign allowed the close observation of an event that met the threshold for a 99th percentile 3-hour event in the IMERG dataset that was characterized by backbuilding convection along the SDC mountain range. This backbuilding was not well represented by convective allowing WRF models used during the campaign. Adding 30 vertical levels (from 51 to 81) to the set up used during the campaign resulted in the model producing limited backbuilding. This was found to be due to the differences in the representation of mountain wave effects as a strong trough crossed the Andes mountain range. With increased vertical levels, turbulence in lower layers of the model was increased and mountain wave activity was significantly dampened. However, comparing forecasts of surface dewpoint from both the 51 and 81 vertical level models

to surface observations of the event reveals that even the 81 vertical level simulation produced too much drying at the surface due to downslope winds from the Andes. This is likely why the 81 vertical level model did not fully simulate the extent of the backbuilding that was observed during the event. These results will aid both researchers and forecasters interested in precipitation in this region by giving context to the long term QPE datasets critical to studies that require a large sample size, while the modeling results illustrate how events in this region can happen.

Bibliography

Aligo, E. A., W. A. Gallus, and M. Segal, 2009: On the impact of wrf model vertical grid resolution on midwest summer rainfall forecasts. *Weather and forecasting*, **24 (2)**, 575–594.

Anabor, V., D. J. Stensrud, and O. L. de Moraes, 2009: Simulation of a serial upstream-propagating mesoscale convective system event over southeastern south america using composite initial conditions. *Monthly Weather Review*, **137 (7)**, 2144–2163.

Arabzadeh, A., M. R. Ehsani, B. Guan, S. Heflin, and A. Behrangi, 2020: Global Intercomparison of Atmospheric Rivers Precipitation in Remote Sensing and Reanalysis Products. *Journal of Geophysical Research: Atmospheres*, **125 (21)**, e2020JD033 021.

Aravind, A., C. Srinivas, R. Shrivastava, M. Hegde, H. Seshadri, and D. Mohapatra, 2022: Simulation of atmospheric flow field over the complex terrain of kaiga using wrf: sensitivity to model resolution and pbl physics. *Meteorology and Atmospheric Physics*, **134 (1)**, 1–25.

Avolio, E., S. Federico, M. Miglietta, T. L. Feudo, C. Calidonna, and A. M. Sempreviva, 2017: Sensitivity analysis of wrf model pbl schemes in simulating boundary-layer variables in southern italy: An experimental campaign. *Atmospheric Research*, **192**, 58–71.

Bang, S. D., and D. J. Cecil, 2019: Constructing a multifrequency passive microwave hail retrieval and climatology in the gpm domain. *Journal of Applied Meteorology and Climatology*, **58 (9)**, 1889–1904.

Beck, H. E., and Coauthors, 2019: Daily Evaluation of 26 Precipitation Datasets using stage-iv Gauge-Radar Data for the conus. *Hydrology and Earth System Sciences*, **23 (1)**, 207–224.

Blacutt, L. A., D. L. Herdies, L. G. G. de Gonçalves, D. A. Vila, and M. Andrade, 2015: Precipitation Comparison for the CFSR, MERRA, TRMM3B42 and Combined Scheme Datasets in Bolivia. *Atmospheric Research*, **163**, 117–131.

Bosilovich, M. G., and Coauthors, 2015: Merra-2: Initial Evaluation of the Climate. *Technical Report Series on Global Modeling and Data Assimilation*, **43**.

Bruick, Z. S., K. L. Rasmussen, and D. J. Cecil, 2019: Subtropical south american Hailstorm Characteristics and Environments. *Monthly Weather Review*, **147 (12)**, 4289–4304.

Cannon, F., L. M. Carvalho, C. Jones, T. Hall, D. Gomberg, J. Dumas, and M. Jackson, 2017: Wrf simulation of downslope wind events in coastal santa barbara county. *Atmospheric Research*, **191**, 57–73.

Casaretto, G., M. E. Dillon, P. Salio, Y. G. Skabar, S. W. Nesbitt, R. S. Schumacher, C. M. García, and C. Catalini, 2022: High-resolution nwp forecast precipitation comparison over complex terrain of the sierras de córdoba during relampago-cacti. *Weather and Forecasting*, **37 (2)**, 241–266.

Cavalcanti, I. F. A., 2012: Large Scale and Synoptic Features Associated with Extreme Precipitation over South America: A Review and Case Studies for the First Decade of the 21st Century. *Atmospheric Research*, **118**, 27–40.

Chen, S., and Coauthors, 2013: Performance Evaluation of Radar and Satellite Rainfalls for Typhoon Morakot over Taiwan: Are Remote-Sensing Products Ready for Gauge Denial Scenario of Extreme Events? *Journal of Hydrology*, **506**, 4–13.

Chou, S.-H., 2011: An example of vertical resolution impact on wrf-var analysis. *Electron. J. Oper. Meteorol*, **12**, 1–20.

Computational, and I. S. Laboratory, 2019: Cheyenne: Hpe/sgi ice xa system (university community computing). National Center for Atmospheric Research Boulder, CO, doi:10.5065/D6RX99HX.

de la Casa, A., and O. Nasello, 2010: Breakpoints in Annual Rainfall Trends in Córdoba, Argentina. *Atmospheric Research*, **95 (4)**, 419–427.

de la Torre, A., R. Hierro, P. Llamedo, A. Rolla, and P. Alexander, 2011: Severe hailstorms near southern andes in the presence of mountain waves. *Atmospheric Research*, **101 (1-2)**, 112–123.

Donat, M. G., J. Sillmann, S. Wild, L. V. Alexander, T. Lippmann, and F. W. Zwiers, 2014: Consistency of Temperature and Precipitation Extremes Across Various Global Gridded In Situ and Reanalysis Datasets. *Journal of Climate*, **27 (13)**, 5019–5035.

Durkee, J. D., T. L. Mote, and J. M. Shepherd, 2009: The Contribution of Mesoscale Convective Complexes to Rainfall Across Subtropical South America. *Journal of Climate*, **22 (17)**, 4590–4605.

DuVivier, A. K., J. J. Cassano, S. Greco, and G. D. Emmitt, 2017: A case study of observed and modeled barrier flow in the denmark strait in may 2015. *Monthly Weather Review*, **145 (6)**, 2385–2404.

Fang, J., W. Yang, Y. Luan, J. Du, A. Lin, and L. Zhao, 2019: Evaluation of the TRMM 3B42 and GPM IMERG Products for Extreme Precipitation Analysis over China. *Atmospheric Research*, **223**, 24–38.

Foelsche, U., G. Kirchengast, J. Fuchsberger, J. Tan, W. A. Petersen, and Coauthors, 2017: Evaluation of GPM IMERG Early, Late, and Final Rainfall Estimates using WegenerNet gauge Data in Southeastern Austria. *Hydrology and Earth System Sciences*, **21 (12)**, 6559–6572.

Giles, J. A., R. C. Ruscica, and C. G. Menéndez, 2021: Warm-Season Precipitation Drivers in Northeastern Argentina: Diurnal Cycle of the Atmospheric Moisture Balance and Land–Atmosphere Coupling. *International Journal of Climatology*, **41**, E768–E778.

Gupta, V., M. K. Jain, P. K. Singh, and V. Singh, 2020: An Assessment of Global Satellite-Based Precipitation Datasets in Capturing Precipitation Extremes: A Comparison With Observed Precipitation Dataset in India. *International Journal of Climatology*, **40 (8)**, 3667–3688.

Hahmann, A. N., C. L. Vincent, A. Peña, J. Lange, and C. B. Hasager, 2015: Wind climate estimation using wrf model output: method and model sensitivities over the sea. *International Journal of Climatology*, **35 (12)**, 3422–3439.

Hernandez, V., V. Moron, F. F. Riglos, and E. Muzi, 2015: Confronting farmers' perceptions of climatic vulnerability with observed relationships between yields and climate variability in central argentina. *Weather, Climate, and Society*, **7 (1)**, 39–59.

Hersbach, H., and Coauthors, 2020: The ERA5 Global Reanalysis. *Quarterly Journal of the Royal Meteorological Society*, **146 (730)**, 1999–2049.

Huffman, G. J., R. F. Adler, D. T. Bolvin, and E. J. Nelkin, 2010: The TRMM Multi-Satellite Precipitation Analysis (TMPA). *Satellite Rainfall Applications for Surface Hydrology*, Springer, 3–22.

Huffman, G. J., D. T. Bolvin, D. Braithwaite, K. Hsu, R. Joyce, P. Xie, and S.-H. Yoo, 2015: NASA Global Precipitation Measurement (GPM) Integrated Multi-Satellite Retrievals for GPM (IMERG). *Algorithm Theoretical Basis Document (ATBD) Version*, **4**, 26.

Hugo, G., and Coauthors, 2006: Trends in Land Degradation in South America. *Management of Natural and Environmental Resources for Sustainable Agricultural Development*.

Hurtado, S. I., P. G. Zaninelli, E. A. Agosta, and L. Ricetti, 2021: InfillingMmethods for Monthly Precipitation Records with Poor Station Network Density in Subtropical Argentina. *Atmospheric Research*, 105482.

Kim, K., J. Park, J. Baik, and M. Choi, 2017: Evaluation of Topographical and Seasonal Feature using GPM IMERG and TRMM 3B42 over Far-East Asia. *Atmospheric Research*, **187**, 95–105.

Kunkel, K. E., S. E. Stevens, L. E. Stevens, and T. R. Karl, 2020: Observed Climatological Relationships of Extreme Daily Precipitation Events with Precipitable Water and Vertical Velocity in the Contiguous United States. *Geophysical Research Letters*, **47 (12)**, e2019GL086 721.

Latrubesse, E. M., and D. Brea, 2009: Floods in Argentina. *Developments in Earth Surface Processes*, **13**, 333–349.

Lavers, D. A., A. Simmons, F. Vamborg, and M. J. Rodwell, 2022: An evaluation of era5 precipitation for climate monitoring. *Quarterly Journal of the Royal Meteorological Society*.

Le Coz, J., and Coauthors, 2016: Crowdsourced Data for Flood Hydrology: Feedback from Recent Citizen Science Projects in Argentina, France and New Zealand. *Journal of Hydrology*, **541**, 766–777.

Mahto, S. S., and V. Mishra, 2019: Does ERA-5 Outperform Other Reanalysis Products for Hydrologic Applications in India? *Journal of Geophysical Research: Atmospheres*, **124 (16)**, 9423–9441.

Mayer, S., M. O. Jonassen, A. Sandvik, and J. Reuder, 2012: Profiling the arctic stable boundary layer in advent valley, svalbard: Measurements and simulations. *Boundary-Layer Meteorology*, **143 (3)**, 507–526.

Merlos, F. A., and Coauthors, 2015: Potential for Crop Production Increase in Argentina Through Closure of Existing Yield Gaps. *Field Crops Research*, **184**, 145–154.

Montini, T. L., C. Jones, and L. M. Carvalho, 2019: The South American Low-Level Jet: A New Climatology, Variability, and Changes. *Journal of Geophysical Research: Atmospheres*, **124 (3)**, 1200–1218.

Mulholland, J. P., S. W. Nesbitt, R. J. Trapp, K. L. Rasmussen, and P. V. Salio, 2018: Convective Storm Life Cycle and Environments near the Sierras de Córdoba, Argentina. *Monthly Weather Review*, **146 (8)**, 2541–2557, doi:10.1175/MWR-D-18-0081.1.

Nesbitt, S. W., and Coauthors, 2021: A storm safari in subtropical south america: Proyecto relampago. *Bulletin of the American Meteorological Society*, **102 (8)**, E1621–E1644.

Peters, J. M., and R. S. Schumacher, 2015: The simulated structure and evolution of a quasi-idealized warm-season convective system with a training convective line. *Journal of the Atmospheric Sciences*, **72 (5)**, 1987–2010.

Petty, G. W., and K. Li, 2013: Improved Passive Microwave Retrievals of Rain Rate over Land and Ocean. Part I: Algorithm Description. *Journal of Atmospheric and Oceanic Technology*, **30 (11)**, 2493–2508.

Phélinas, P., and J. Choumert, 2017: Is gm soybean cultivation in argentina sustainable? *World Development*, **99**, 452–462.

Piersante, J. O., K. L. Rasmussen, R. S. Schumacher, A. K. Rowe, and L. A. McMurdie, 2021: A synoptic evolution comparison of the smallest and largest mcss in subtropical south america between spring and summer. *Monthly Weather Review*, **149 (6)**, 1943–1966.

Rasmussen, K., M. Chaplin, M. Zuluaga, and R. Houze Jr, 2016: Contribution of Extreme Convective Storms to Rainfall in South America. *Journal of Hydrometeorology*, **17 (1)**, 353–367.

Rasmussen, K. L., M. D. Zuluaga, and R. A. Houze Jr, 2014: Severe Convection and Lightning in Subtropical South America. *Geophysical Research Letters*, **41 (20)**, 7359–7366.

Reichle, R. H., and Q. Liu, 2014: Observation-Corrected Precipitation Estimates in GEOS-5. *Technical Report Series on Global Modeling and Data Assimilation*, **35**.

Rocque, M. N., and K. L. Rasmussen, 2022: The impact of topography on the environment and life cycle of weakly and strongly forced mcss during relampago. *Monthly Weather Review*, **150 (9)**, 2317–2338.

Schumacher, R. S., and Coauthors, 2021: Convective-storm environments in subtropical south america from high-frequency soundings during relampago-cacti. *Monthly Weather Review*, **149 (5)**, 1439–1458.

Sekaranom, A. B., and H. Masunaga, 2017: Comparison of TRMM-Derived Rainfall Products for General and Extreme Rains over the Maritime Continent. *Journal of Applied Meteorology and Climatology*, **56 (7)**, 1867–1881.

Sun, X., and A. P. Barros, 2010: An Evaluation of the Statistics of Rainfall Extremes in Rain Gauge Observations, and Satellite-Based and Reanalysis Products Using Universal Multifractals. *Journal of Hydrometeorology*, **11 (2)**, 388–404.

Taghizadeh, E., F. Ahmadi-Givi, L. Brocca, and E. Sharifi, 2021: Evaluation of Satellite/Reanalysis Precipitation Products over Iran. *International Journal of Remote Sensing*, **42 (9)**, 3474–3497.

Tan, J., G. J. Huffman, D. T. Bolvin, and E. J. Nelkin, 2019: Diurnal Cycle of IMERG V06 Precipitation. *Geophysical Research Letters*, **46 (22)**, 13 584–13 592.

Tang, G., M. P. Clark, S. M. Papalexiou, Z. Ma, and Y. Hong, 2020: Have Satellite Precipitation Products Improved Over Last Two Decades? a Comprehensive Comparison of GPM IMERG with Nine Satellite and Reanalysis Datasets. *Remote Sensing of Environment*, **240**, 111 697.

Taszarek, M., N. Pilguj, J. T. Allen, V. Gensini, H. E. Brooks, and P. Szuster, 2020: Comparison of Convective Parameters Derived from ERA5 and MERRA2 with Rawinsonde Data over Europe and North America. *Journal of Climate*, 1–55.

Vidal, L., S. W. Nesbitt, P. Salio, C. Farias, M. G. Nicora, M. S. Osores, L. Mereu, and F. S. Marzano, 2017: C-Band Dual-Polarization Radar Observations of a Massive Volcanic Eruption in South Aamerica. *IEEE Journal of Selected Topics in Applied Earth Observations and Remote Sensing*, **10 (3)**, 960–974.

Villarini, G., and W. F. Krajewski, 2007: Evaluation of the Research Version TMPA Three-Hourly $0.25\times$ 0.25 Rainfall Estimates over Oklahoma. *Geophysical Research Letters*, **34 (5)**.

Xia, G., C. Draxl, A. Raghavendra, and J. K. Lundquist, 2021: Validating simulated mountain wave impacts on hub-height wind speed using sodar observations. *Renewable Energy*, **163**, 2220–2230.

Xu, H., C.-Y. Xu, H. Chen, Z. Zhang, and L. Li, 2013: Assessing the Influence of Rain Gauge Density and Distribution on Hydrological Model Performance in a Humid Region of China. *Journal of Hydrology*, **505**, 1–12.

Xue, X., Y. Hong, A. S. Limaye, J. J. Gourley, G. J. Huffman, S. I. Khan, C. Dorji, and S. Chen, 2013: Statistical and Hydrological Evaluation of TRMM-Based Multi-Satellite Precipitation Analysis over the Wangchu Basin of Bhutan: Are the Latest Satellite Precipitation Products 3B42V7 Ready for Use in Ungauged Basins? *Journal of Hydrology*, **499**, 91–99.

Yucel, I., and A. Onen, 2014: Evaluating a Mesoscale Atmosphere Model and a Satellite-Based Algorithm in Estimating Extreme Rainfall Events in Northwestern Turkey. *Natural Hazards and Earth System Sciences*, **14 (3)**, 611–624.

Zipser, E. J., D. J. Cecil, C. Liu, S. W. Nesbitt, and D. P. Yorty, 2006: Where Are the Most Intense Thunderstorms on earth? *Bulletin of the American Meteorological Society*, **87 (8)**, 1057–1072.